

University of Windsor

Scholarship at UWindor

Electronic Theses and Dissertations

Theses, Dissertations, and Major Papers

2002

Synthesis and electronic, magnetic properties of low-dimensional organometallic reduced mesoporous niobium oxide composites.

Xun. He

University of Windsor

Follow this and additional works at: <https://scholar.uwindsor.ca/etd>

Recommended Citation

He, Xun., "Synthesis and electronic, magnetic properties of low-dimensional organometallic reduced mesoporous niobium oxide composites." (2002). *Electronic Theses and Dissertations*. 3690.
<https://scholar.uwindsor.ca/etd/3690>

This online database contains the full-text of PhD dissertations and Masters' theses of University of Windsor students from 1954 forward. These documents are made available for personal study and research purposes only, in accordance with the Canadian Copyright Act and the Creative Commons license—CC BY-NC-ND (Attribution, Non-Commercial, No Derivative Works). Under this license, works must always be attributed to the copyright holder (original author), cannot be used for any commercial purposes, and may not be altered. Any other use would require the permission of the copyright holder. Students may inquire about withdrawing their dissertation and/or thesis from this database. For additional inquiries, please contact the repository administrator via email (scholarship@uwindsor.ca) or by telephone at 519-253-3000ext. 3208.

INFORMATION TO USERS

This manuscript has been reproduced from the microfilm master. UMI films the text directly from the original or copy submitted. Thus, some thesis and dissertation copies are in typewriter face, while others may be from any type of computer printer.

The quality of this reproduction is dependent upon the quality of the copy submitted. Broken or indistinct print, colored or poor quality illustrations and photographs, print bleedthrough, substandard margins, and improper alignment can adversely affect reproduction.

In the unlikely event that the author did not send UMI a complete manuscript and there are missing pages, these will be noted. Also, if unauthorized copyright material had to be removed, a note will indicate the deletion.

Oversize materials (e.g., maps, drawings, charts) are reproduced by sectioning the original, beginning at the upper left-hand corner and continuing from left to right in equal sections with small overlaps.

**ProQuest Information and Learning
300 North Zeeb Road, Ann Arbor, MI 48106-1346 USA
800-521-0600**

UMI[®]

Synthesis and Electronic, Magnetic Properties of Low-Dimensional Organometallic Reduced Mesoporous Niobium Oxide Composites

by

Xun He

A Thesis

Submitted to the Faculty of Graduate Studies and Research
through the Department of Chemistry and Biochemistry
In Partial Fulfillment of the Requirements for
the Degree of Master of Science at the
University of Windsor

Windsor, Ontario, Canada
2002



**National Library
of Canada**

**Acquisitions and
Bibliographic Services**

**385 Wellington Street
Ottawa ON K1A 0N4
Canada**

**Bibliothèque nationale
du Canada**

**Acquisitions et
services bibliographiques**

**385, rue Wellington
Ottawa ON K1A 0N4
Canada**

Your file Votre référence

Our file Notre référence

The author has granted a non-exclusive licence allowing the National Library of Canada to reproduce, loan, distribute or sell copies of this thesis in microform, paper or electronic formats.

The author retains ownership of the copyright in this thesis. Neither the thesis nor substantial extracts from it may be printed or otherwise reproduced without the author's permission.

L'auteur a accordé une licence non exclusive permettant à la Bibliothèque nationale du Canada de reproduire, prêter, distribuer ou vendre des copies de cette thèse sous la forme de microfiche/film, de reproduction sur papier ou sur format électronique.

L'auteur conserve la propriété du droit d'auteur qui protège cette thèse. Ni la thèse ni des extraits substantiels de celle-ci ne doivent être imprimés ou autrement reproduits sans son autorisation.

0-612-75832-X

Canada

© 2002 Xun He

189866

Abstracts

Herein I report the synthesis of a new family of organometallic reduced mesoporous niobium oxide composites with mixed oxidation-state organometallic nanowires in the pores and investigate their electronic and magnetic properties. This is a wonderful system which allows us to systematically study one-dimensional molecular metals based on the respective organometallic species and the reducible mesoporous niobium oxide structure. Investigations were conducted on the effects of electron configuration, ionization potential, and electron affinity of organometallic species as well as the composition of mesoporous transition metal oxide walls on the electronic and magnetic properties in the composites and the loading level of organometallics.

Results obtained in this work showed the treatment of mesoporous niobium oxide with bis(benzene)chromium, bis(benzene)vanadium, bis(cyclopentadienyl)vanadium, bis(cyclopentadienyl)chromium or decamethylsamarocene led to semiconducting materials with mixed oxidation-state organometallic phases in the pores. The conductivity was as high as $10^{-4} \text{ ohm}^{-1}\text{cm}^{-1}$. The mixed oxidation-state organometallic phase was found playing a main role on the conductivity which was attributed to the oxidation-induced molecular orbital holes in the organometallic phase. The Hubbard model was successfully applied to this new family of materials in an effort to understand the origin of conductivity.

Materials in this work were characterized by a combination of techniques including XRD, nitrogen adsorption, EPR spectroscopy, XPS, SQUID magnetometry, room temperature DC conductivity measurements, NMR, and elemental analysis.

Acknowledgements

Firstly, I would like to thank my supervisor Dr. David M. Antonelli for his guidance and help on my studies and research during my graduate term at University of Windsor. His kind advice and support have been greatly appreciated and will be remembered forever.

I am deeply grateful to Dr. Michel Trudeau who gave me a lot of help with the analysis of XPS and SQUID samples. I am also grateful to Dr. Bruce McGarvey and Dr. Raymond Sung for their help with ESR spectra. Mr. J. Robinson is acknowledged for his help with collecting powder XRD data. Dr. P. Wei is thanked for help with single crystal structure determination.

I am grateful to our group members, Mrs. S. Murray, Mr. B. Ye, Ms. M. Vettrano and Mr. B. Skadtchenko for their help and advice. Many thanks are given to the faculty and staff of Department of Chemistry and Biochemistry, University of Windsor, for their support and kind help during the period of my graduate study and research.

Finally, the special thanks are due to my wife Weijuan Jia, my daughter Qingyu He, my parents and my sisters for their encouragement and support.

Table of Contents

Abstract	iv
Acknowledgements	v
List of Figures	xiii
List of Tables	xix
List of Abbreviations	xxi
Chapter 1. Introduction	1
1.1. Electroactive Mesoporous Transition Metal Oxides	2
1.1.1. Mesoporous Zirconium Oxide Based Systems for Fuel-Cell Applications	2
1.1.2. Semiconducting Mesoporous Manganese Oxides	7
1.1.3. Hierarchically Templated Mixed-Valent Molybdenum Oxides	8
1.1.4. Photocatalytic Activity of Mesoporous Niobium and Phosphated Titanium Oxides	11
1.1.5. Photocatalytic Activity of Mesoporous Tantalum Oxides	12
1.1.6. Alkali Reduced Mesoporous Niobium, Tantalum, and Titanium Materials	14
1.1.7. Superparamagnetic Mesoporous Niobium Oxide-Cobaltocene and Nickelocene Composites	17
1.1.8. One Dimensional Alkali Fulleride Wires Supported by a Mesoporous	

Niobium oxide Host	21
1.1.9. Electroactive Mesoporous Tungsten Oxides	24
1.2. Mesostructured Sulfides and Selenides	26
1.2.1. Mesostructured Germanium Sulfides	26
1.2.2. More Germanium Sulfides and Selenides and even some Tin	28
1.3. Mesostructured Metals	33
1.3.1. Mesostructured Platinum	33
1.3.2. Metal Carbonyls as Mesostructure Building Blocks	35
1.4. Summary and Outlook	36
Chapter 2. Electronic Properties of Novel Mixed Oxidation State Bis-Arene Chromium Nanowires Supported by a Mesoporous Niobium Oxide Host	38
2.1. Experimental Section	39
2.1.1. Materials and Equipment	39
2.1.2. Synthesis	40
2.2. Results and Discussions	40
2.2.1. X-ray Powder Diffraction Pattern and Nitrogen Adsorption Studies	41
2.2.2. Ultraviolet (UV)-Visible Reflectance Measurements	42
2.2.3. Electron Paramagnetic Resonance (EPR) Spectroscopy	43
2.2.4. Conductivity Measurements	44
2.2.5. X-Ray Photoelectron Spectroscopy	45

2.2.6. Superconducting Quantum Interference Detector (SQUID)	
Measurements	47
2.3. Conclusions	48
Chapter 3. Synthesis and Electronic Properties of Low-Dimensional	
Bis(benzene) Vanadium Reduced Mesoporous Niobium Oxide Composites	49
3.1. Experimental Section	49
3.1.1. Materials and Equipment	49
3.1.2. Syntheses	50
3.2. Results	51
3.2.1. X-ray Powder Diffraction (XRD) Pattern, Nitrogen Adsorption Study and Elemental Analysis	51
3.2.2. Ultraviolet-Visible (UV-vis) Reflectance Measurements	53
3.2.3. Electron Paramagnetic Resonance (EPR) Spectrum	53
3.2.4. Solid State NMR Spectrum and Raman Spectroscopy	54
3.2.5. X-ray Photoelectron Spectroscopy (XPS)	55
3.2.6. Superconducting Quantum Interference Detector (SQUID)	
Measurements	57
3.3. Discussion	58
3.4. Conclusion	63

Chapter 4. Bis(cyclopentadienyl) Chromium and Bis(cyclopentadienyl)

Vanadium Composites of Mesoporous Niobium Oxide With Pseudo One-Dimensional Organometallic Wires in the Pores	64
4.1. Experimental Method	65
4.1.1. Materials and Equipment	65
4.1.2. Synthesis	65
4.2. Results	67
4.2.1. X-ray Powder Diffraction (XRD) Pattern, Nitrogen Adsorption Study and Elemental Analysis	67
4.2.2. UV-Visible Reflectance Measurements of Bis(cyclopentadienyl)vanadium Composites of Mesoporous Niobium Oxide	69
4.2.3. Electron Paramagnetic Resonance (EPR) Spectra of Bis(cyclopentadienyl) Vanadium Composites of Mesoporous Niobium Oxide	70
4.2.4. X-ray Photoelectron Spectroscopy (XPS) Studies of Bis(cyclopentadienyl) Vanadium Composites of Mesoporous Niobium Oxide	71
4.2.5. Superconducting Quantum Interference Detector(SQUID) Measurements of Bis(cyclopentadienyl) Vanadium Composites of Mesoporous Niobium Oxide	73
4.2.6. Electron Paramagnetic Resonance (EPR) Spectra of Bis(cyclopentadienyl) Chromium Composites of Mesoporous Niobium	

Oxide	74
4.2.7. X-ray Photoelectron Spectra of Bis(cyclopentadienyl) Chromium Composites of Mesoporous Niobium Oxide	76
4.2.8. Superconducting Quantum Interference Detector (SQUID) Measurements	78
4.3. Discussion	79
4.4. Conclusion	83
Chapter 5. Electronic and Magnetic Properties of Bis-benzene Chromium Composites of Mesoporous V-Nb Mixed Oxides	84
5.1. Experimental Section	84
5.1.1. Materials and Equipment	84
5.1.2. Synthesis	85
5.2. Results and Discussion	86
5.2.1. Nitrogen Adsorption Study and XRD Patterns of As-synthesized Mesoporous V-Nb Oxides	86
5.2.2. EPR Spectra of As-synthesized Mesoporous V-Nb Oxides	88
5.2.3. XPS Spectra of As-synthesized Mesoporous V-Nb Oxides	89
5.2.4. Nitrogen Adsorption Study, XRD Patterns and Elemental Analysis of Bis(benzene) Chromium Composites of Mesoporous V-Nb Mixed Oxide	91
5.2.5. EPR Spectra of Bis(benzene) Chromium Composites of Mesoporous	

V-Nb Mixed Oxide	95
5.2.6. XPS Spectra of Bis(benzene) Chromium Composites of Mesoporous V-Nb Mixed Oxide	96
5.2.7. Conductivity Measurement of Bis(benzene) Chromium Composites of Mesoporous V-Nb Mixed Oxide	98
5.2.8. SQUID Measurements of Bis(benzene) Chromium Composites of Mesoporous V-Nb Mixed Oxides	100
5.2.9. Solid State ^2H -NMR Studies	101
5.3. Conclusion	102
Chapter 6. Magnetic Properties of Decamethylsamarocene Composites of Mesoporous Niobium Oxide	103
6.1. Experimental Section	104
6.1.1. Materials and Equipment	104
6.1.2. Synthesis	104
6.2. Results and Discussion	105
6.2.1. XRD Patterns and Nitrogen Adsorption Studies	105
6.2.2. EPR Spectrum	108
6.2.3. XPS Spectra	108
6.2.4. Conductivity Measurements	110
6.2.5. SQUID Measurements	111
6.3. Conclusion	114

Chapter 7. Conclusion	115
Appendix	118
References	122
Vita Auctoris	132
Publications and Presentations (1999 – 2002)	132

List of Figures

Chapter 1. Introduction

- Figure 1.** Schematic representation of lamellar-to-hexagonal phase transformation in mesostructured zirconia 4
- Figure 2.** Self-assembly of a mesoporous platinum-yttria-zirconia material denoted *meso*-PtYZ. 4
- Figure 3.** Complex impedance Argand plot for *meso*-NiO-YSZ. 6
- Figure 4.** Transmission electron micrographs (TEM) of molybdenum oxide bronzes 9
- Figure 5.** Time course of photocatalytic decomposition of water over NiO (4 wt%)-loaded mesoporous Ta₂O₅ after R673-0473 treatment 13
- Figure 6.** Reduction of Nb-TMS1 with bis(toluene) niobium, Na, cobaltocene, nickelocene, K₃C₆₀, and bis(benzene)chromium 15
- Figure 7.** Energy-level diagram of alkali-reduced M-TMS1 (M = Ta, Nb, Ti). 16
- Figure 8.** Temperature dependence of magnetic susceptibility for Nb-TMS1 after reduction with Cp₂Co. 18
- Figure 9.** Optical transmittance spectra for mesoporous and sol-gel tungsten oxide. 25
- Figure 10.** Proposed architecture of a mesostructured germanium sulfide material. 26

Figure 11.	TEM images of worm-like particles of (CTA)NiGe ₄ S ₁₀ .	27
Figure 12.	Proposed structure model of the C _n MGeQ phases.	29
Figure 13.	Electronic absorption spectra and photoluminescence spectra of mesostructured sulfide.	31
Figure 14.	SEM image of a washed sample of mesoporous platinum and TEM image of H ₁ -platinum (bottom).	33
Figure 15.	Thermal treatment of layered platinum carbonyl phases results in loss of CO and formation of a new platinum-based layered material.	35
Chapter 2. Electronic Properties of Novel Mixed Oxidation State Bis-Arene Chromium Nanowires Supported by a Mesoporous Niobium Oxide Host		
Figure 16.	XRD pattern (CuK α) of a sample of mesoporous niobium oxide treated with 0.07 equivalents of bis-benzene chromium	41
Figure 17.	Powder EPR spectra of mesoporous niobium oxide after treated with bis-benzene chromium	43
Figure 18.	Schematic representation of bis-benzene chromium molecular nanowires in a mesoporous niobium oxide host.	45
Figure 19.	XPS spectra of mesoporous Nb oxide after treatment with excess bis(benzene)chromium.	46
Figure 20.	Plot of magnetic susceptibility vs. temperature for Nb-TMS1	

sample with 0.07 equivalents of bis(benzene) chromium 47

Chapter 3. Synthesis and Electronic Properties of Low-Dimensional Bis(benzene) Vanadium Reduced Mesoporous Niobium Oxide Composites

Figure 21. XRD pattern of Nb-TMS1 before and after treatment with $(C_6H_6)_2V$. 51

Figure 22. (a) Nitrogen adsorption and desorption isotherms and incremental HK pore volume vs. pore diameter plots of Nb-TMS1 before and after treatment with excess $(C_6H_6)_2V$ 52

Figure 23. Powder EPR spectrum of Nb-TMS1 treated with excess $(C_6H_6)_2V$. 54

Figure 24. XPS spectrum of Nb-TMS1 treated with excess $(C_6H_6)_2V$ 56

Figure 25. (a) M vs. T plot for a sample of Nb-TMS1 treated with excess $(C_6H_6)_2V$. (b) Plot of $1/\chi_m$ vs. T for the sample in (a) 58

Chapter 4. Bis(cyclopentadienyl) Chromium and Bis(cyclopentadienyl) Vanadium Composites of Mesoporous Niobium Oxide With Pseudo One-Dimensional Organometallic Wires in the Pores

Figure 26. XRD patterns of Nb-TMS1 before and after treatment with excess Cp_2V and Cp_2Cr . 67

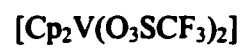
Figure 27. Nitrogen adsorption and desorption isotherms of Nb-TMS1 before and after treatment with with excess Cp_2V and Cp_2Cr , and

	plots of incremental HK pore volume vs. average pore diameter	68
Figure 28.	Powder EPR spectra of Nb-TMS1 treated with excess Cp ₂ V	70
Figure 29.	XPS spectra of Nb-TMS1 treated with excess Cp ₂ V	72
Figure 30.	M vs. T plots for a sample of Nb-TMS1 treated with excess Cp ₂ V	73
Figure 31.	Powder EPR spectra of Nb-TMS1 treated with excess Cp ₂ Cr	76
Figure 32.	XPS spectra of Nb-TMS1 treated with excess Cp ₂ Cr	77
Figure 33.	M vs. T plots for a sample of Nb-TMS1 treated with excess Cp ₂ Cr	79
Chapter 5. Electronic and Magnetic Properties of Bis-benzene		
Chromium Composites of Mesoporous V-Nb Mixed Oxides		
Figure 34.	(a) Nitrogen adsorption and desorption isotherms of Nb-TMS1 and material 1, 2, and 3. (b) Plots of incremental HK pore volume vs. average pore diameter for materials from (a).	87
Figure 35.	XRD patterns of (a) Nb-TMS1, (b) 1, (c) 2, and (d) 3.	88
Figure 36.	Powder EPR spectrum of 1 and the simulation of this spectrum	89
Figure 37.	XPS spectra of all materials from Figure 1 of Chapter 5.	90
Figure 38.	Nitrogen adsorption and desorption isotherms of Nb-TMS1, material 4, 5 and 6 before and after treatment with excess (C ₆ H ₆) ₂ Cr.	91
Figure 39.	XRD patterns of Nb-TMS1, material 4, 5 and 6 before and after treatment with excess (C ₆ H ₆) ₂ Cr.	94

Figure 40.	EPR spectra of all materials from Figure 6 and diluted samples.	95
Figure 41.	XPS spectra of all materials from Figure 6 after treatment with excess $(C_6H_6)_2Cr$.	97
Figure 42.	M vs. T plots and $1/\chi_g$ vs. T plots for all materials from Figure 6	99
Chapter 6. Magnetic Properties of Decamethylsamarocene Composites of Mesoporous Niobium Oxide		
Figure 43.	XRD patterns of trimethylsilated Nb-TMS1 before and after treatment with excess $(C_5Me_5)_2Sm(THF)_2$	106
Figure 44.	(a) Nitrogen adsorption and desorption isotherms of trimethylsilated Nb-TMS1 before and after treatment with excess $(C_5Me_5)_2Sm(THF)_2$. (b) Plots of incremental HK pore volume vs. average pore diameter before and after treatment with excess $(C_5Me_5)_2Sm(THF)_2$.	107
Figure 45.	Powder EPR spectrum of trimethylsilated Nb-TMS1 before and after treatment with excess $(C_5Me_5)_2Sm(THF)_2$	108
Figure 46.	XPS spectra of trimethylsilated Nb-TMS1 before and after treatment with excess $(C_5Me_5)_2Sm(THF)_2$.	109
Figure 47.	M vs. T plot, χ_m vs. $1/T$ plot and B vs. H plots for the sample of trimethylsilated Nb-TMS1 before and after treatment with excess $(C_5Me_5)_2Sm(THF)_2$.	112

Appendix

Figure 48. Single crystal structure (ORTEP) of vanadocenium ditriflate



118

List of Tables

Chapter 1. Introduction

Table 1.	Conductivities and corresponding activation energies of mesoporous Pt (NiO)-YSZ.	6
Table 2.	Characterization and reactivity results for titania and niobia materials	11
Table 3.	Comparison of the photocatalytic activity of NiO loaded tantalum oxides	13

Chapter 5. Electronic and Magnetic Properties of Bis-benzene

Chromium Composites of Mesoporous V-Nb Mixed Oxides

Table 4.	BET surface area, pore size and pore volume of the as-synthesized mesoporous V-Nb oxides	87
Table 5.	BET surface area, pore size and pore volume of trimethylsilylated mesoporous V-Nb oxides and the corresponding bis(benzene) chromium composites.	93
Table 6.	Carbon and hydrogen elemental analysis results of the mesoporous transition metal oxides before and after reduction with bis(benzene) chromium.	94
Table 7.	The effects of vanadium contents on the conductivity of bis(benzene) chromium reduced mesoporous V-Nb oxide	

	composites	99
Table 8.	Curie constants, Weiss constants and effective magnetic moments of the samples made from mesoporous V-Nb oxide and excess bis(benzene) chromium	101
Appendix		
Table 9.	Lattice constants and parameters of the structure determination of vanadocenium ditriflate [$\text{Cp}_2\text{V}(\text{O}_3\text{SCF}_3)_2$]	118
Table 10.	Atomic coordinates ($\times 10^4$) and equivalent isotropic displacement parameters ($\text{\AA}^2 \times 10^3$) for $\text{Cp}_2\text{V}(\text{O}_3\text{SCF}_3)_2$	119
Table 11.	Selected bond distance (\AA) and bond angles ($^\circ$) for $\text{Cp}_2\text{V}(\text{O}_3\text{SCF}_3)_2$	121

List of Abbreviations

The Family of Silica Based Mesoporous Materials	M41S
Mobil Composition of Matter-41, Hexagonal Mesoporous Phase	MCM-41
Mobil Composition of Matter-48, Cubic Mesoporous Phase	MCM-48
Mobil Composition of Matter-50, Hexagonal Mesoporous Phase	MCM-50
Hexagonally Ordered Mesoporous Niobium Oxide	Nb-TMS1
Hexagonally Ordered Mesoporous Tantalum Oxide	Ta-TMS1
Hexagonally Ordered Mesoporous Titanium Oxide	Ti-TMS1
Liquid Crystal Template	LCT
Ligand Assisted Template	LAT
Cetyltrimethylammonium Bromide	CTAB
Cyclopentadienyl	Cp
Trimethylsilyl	TMS
Tetrahydrofuran	THF
X-ray Diffraction	XRD
X-ray Photoelectron Spectroscopy	XPS
Electron Paramagnetic Resonance Spectroscopy	EPR
Electron Spin Resonance Spectroscopy	ESR
Number of Electron Counts per Electron	N(E)/E
Superconducting Quantum Interference Detector	SQUID
Zero-Field Cooling	ZFC

Field Cooling	FC
Nuclear Magnetic Resonance	NMR
Ultra-Violet Spectroscopy	UV
Fourier Transform Infra-Red Spectroscopy	FT-IR
Magic Angle Spin Nuclear Magnetic Resonance	(MAS)NMR
Extended X-ray Adsorption Fine Structure	EXAFS
Energy Dispersive X-ray Spectroscopy	EDS
Solid Oxide Fuel Cell	SOFC
Brunauer, Emmett, Teller	BET
Horvath-Kowazoe	HK
Yttria-Stabilized-Zirconia	YSZ
Transmission Electron Microscopy	TEM
Scanning Electron Microscopy	SEM
Blocking Temperature	T_b
Inductively Coupled Plasma	ICP
Magnetic Susceptibility versus Magnetic Field	B vs. H
Magnetic Susceptibility versus Temperature	M vs. T
Bis(benzene)chromium	(C₆H₆)₂Cr
Bis(benzene)vanadium	(C₆H₆)₂V
Bis(Cyclopentadienyl)chromium	Cp₂Cr
Bis(Cyclopentadienyl)vanadium	Cp₂V
Decamethylsamarocene	(C₅Me₅)₂Sm

Chapter 1. Introduction

In the wake of a great expansion of interest in the design and synthesis of materials with tailored chemical and physical properties, materials scientists have focussed much attention on shape-controlled composite materials with the goal in mind of creating systems in which there is functional cooperation between the overall nanoscale architecture of the material and its physical properties. Multilayered nanotubes,¹ imprinted polymers,² polymer-encapsulated drug delivery systems,³ and "artificial leaf" technologies⁴ are examples of systems that weave two or more disparate materials into a single whole possessing electronic, mechanical, or optical properties not possible in more simple single phase bulk systems. A crucial feature in the design of many functional materials is controlled porosity over a broad length scale. Advances by Mobil researchers in the 1990s led to the discovery of M41S mesoporous silicates, a family of materials with regularly spaced nanometer-sized pores, synthesized using liquid crystals as structural imprints to cast the shape of the silica.⁵⁻¹² Since this work, researchers have expanded this basic motif to the point where it is possible to synthesize fabricated architectures with a myriad of structural features and pore sizes ranging from 1-10,000 nm out of virtually any stable solid substance that can be easily manipulated on the nanoscale.¹³ Single molecules,¹⁴ self-assembled surfactant phases,¹⁵ amphiphilic block co-polymers,^{16,17} vesicles,¹⁸ emulsion-stablized oil droplets,¹⁹ and even micron-level latex spheres^{20,21} have all been used in this regard, the last example being of particular importance to the fabrication of photonic band gap materials.²² Transition metals and transition metal oxides are of particular interest in the synthesis of ordered materials

because of their variable oxidation states, properties not possessed by silicates, a capacity which often leads to unusual magnetic, electronic, and optical properties.

After pioneering efforts leading to the synthesis of mesostructured W and Pb oxides in 1993,²³ a stable mesoporous Nb oxide molecular sieve was reported in 1996.^{24,25} This material had an advantage over the W and Pb materials in that the pore structure remained intact after template removal. Shortly thereafter the synthesis of related mesoporous Zr, Ti, Ta, Hf, and Mn oxides,²⁶⁻³⁸ were reported, the last example being of special note since it was the first such material with semiconducting properties,³⁸ an important feature in many catalytic and electronic applications. More recently, Ozin reported the synthesis of mesoporous Y-doped Zr oxide materials with high ion conductivity for fuel cell applications,³⁹ while Kanatzidis⁴⁰ and Ozin⁴¹ independently synthesized mesoporous Ge sulfide based materials with semiconducting properties. Research in our group has focussed on the reduction and modification of existing mesoporous Nb, Ti, and Ta oxides,^{42,43} to lead to numerous organometallic/inorganic composites with semiconducting, metallic, superparamagnetic, and even spin-glass behavior. This introduction will focus principally on these and other recent advances in electroactive molecular sieves, an exciting and rapidly growing area of research interest.

1.1. Electroactive Mesoporous Transition Metal Oxides

1.1.1. Mesoporous Zirconium Oxide Based Systems for Fuel-Cell Applications

Solid oxide fuel cells (SOFC) have attracted much recent attention in the fields of materials science, catalysis, ceramics, and electrochemistry.⁴⁴ Much of this research is aimed at the design of electrode materials which are not only stable under high operating

temperatures (600-1000°C), but also have optimal electronic and ionic conductivity coupled with catalytic activity and mass-transfer properties. The traditional electrode materials are nickel/yttria-stabilized-zirconia (Ni-YSZ) cermet as the anode and perovskite or platinum/yttria-stabilized-zirconia (Pt-YSZ) as the cathode. The common approach to improve the performance of the materials is to enlarge the triple-phase boundary (TPB), which controls the efficiency of the SOFCs, by decreasing the dimensions of the active metal particles, Ni or Pt, relative to that of the yttria-stabilized-zirconia grains. Several researchers have attempted to improve the porosity and enlarge the TPB of the materials by manipulating the microstructure of electrode materials through traditional nanofabrication techniques,⁴⁵ but most of these materials are just nanoscale or microscale versions of the bulk cermet electrode ceramics with a comparatively low thermal stability and wide pore size distribution. Ozin's group recently reported the first example of binary and ternary mesoporous yttria-stabilized-zirconia (meso-YSZ) and metal (Pt, Ni)-yttria-zirconia solid solutions which could be used as solid oxide fuel cell electrode materials.^{39, 46, 47} While much work has gone into the synthesis of stable mesoporous zirconias, including an elegant recent example from Rao's group⁴⁸ demonstrating an unusual lamellar-to-hexagonal-to-cubic phase change (Figure 1), these materials differ previous efforts in that they use Y as a stabilizing agent. These mesoporous yttria-stabilized-zirconia materials were synthesized via modified sol-gel methods under basic conditions, where zirconium ethoxide and yttrium acetate were used as the precursors for the transition metal oxides, and the cationic surfactant, cetyltrimethylammonium bromide (CTAB) was used as the mesostructure-directing reagent. The higher dielectric constant and coordinating ability of ethylene glycol was to

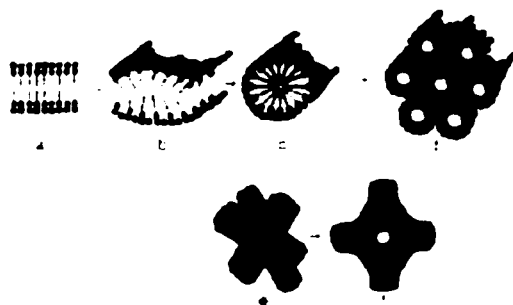


Figure 1. Schematic representation of lamellar-to-hexagonal phase transformation (a - d) and the hexagonal-to-cubic transformation (e and f) in mesostructured zirconia.⁴⁸

control the rate of hydrolysis and avoid the solubility problems which previously resulted in low levels of yttria incorporation in the zirconia phase.⁴⁹ The surfactant template was removed by calcining the as-synthesized materials at various rates and temperatures. The yttrium content in these binary materials can be tuned from 12-56 wt.% and no phase segregation of yttria and zirconia was observed. The nitrogen adsorption isotherms of these materials after calcination gave Brunauer-Emmett-Teller (BET) surface areas ranging from 100-300 m²g⁻¹, and an average pore size of 18-21 Å. The pore wall was determined to be 25-28 Å thick and composed of nanocrystalline yttria-stabilized zirconia. The synthetic strategy is outlined in Figure 2. The variable temperature powder X-ray diffraction patterns illustrated the high structural stability of these materials at temperatures above 600 °C, a property crucial for useful solid oxide fuel cell materials.

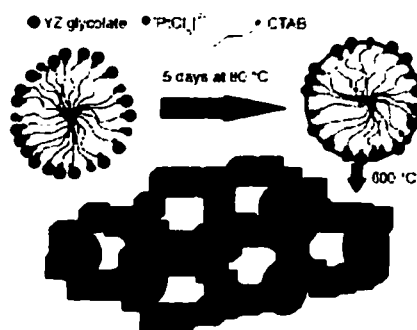


Figure 2. Self-assembly of anionic yttrium-zirconium glycolate and hexachloroplatinate precursors with a supramolecular cationic surfactant template leading to formation of a mesoporous platinum-yttria-zirconia material denoted *meso*-PtYZ.⁴⁶

This material possesses the highest surface area of any recorded sample of template-free yttria-stabilized zirconia.

Electroactive ternary mesoporous metal (Pt, Ni)- yttria-zirconia, were synthesized using metal precursors such as sodium hexachloroplatinate, or Ni(II) reagents, i.e. bis(acetato) nickel, nickel chloride or nickel nitrate as the source of the third metal dopant in the presence of surfactant-containing yttria-zirconia gels.^{46,47} This method produced ternary transition metal oxides with pore structures similar to those of the meso-YSZ materials. The inclusion of Ni or Pt in the materials is necessary for applications in fuel cells, as it effects the charge transfer and oxygen transport properties. In these materials platinum and nickel exist as metal (Pt) and metal oxide (NiO_{1+x}) nanoclusters respectively, 30-40 Å in size, homogeneously dispersed throughout the yttria-zirconia mesostructures. The amount of Pt and Ni can be tuned from 1-10 wt.% and 10-30 wt.% respectively. A chemisorption titration experiment on meso-Pt-YSZ by use of $\text{H}_2\text{-O}_2$ adsorbents showed that the surface area of the incorporated platinum nanoclusters was partly accessible to gaseous reagents and gave a representative dispersion of 18% for sample loading with 2.4 wt% Pt. The ionic conductivity of meso-Pt (NiO)-YSZ materials was evaluated by alternating current (AC) complex impedance spectroscopy in the temperature range of 300°C to 800°C and recorded in an air atmosphere. The meso-YSZ and meso-Pt-YSZ samples gave a single symmetric, slightly depressed semicircle from 500 °C to 700°C resulting from both bulk and grain boundary polarization and all meso-NiO-YSZ samples yielded similar impedance spectra. The bulk and grain boundary conductivity of all meso-Pt (NiO)-YSZ samples was extracted from the low frequency minima of the respective semicircles in the Argand plots of the

complex impedance spectra (Figure 3). The corresponding activation energies E_a for thermally activated charge-transported process were obtained from the Arrhenius equation $\sigma=(A/T)\exp(E_a/RT)$. These data are summarized in the Table 1.

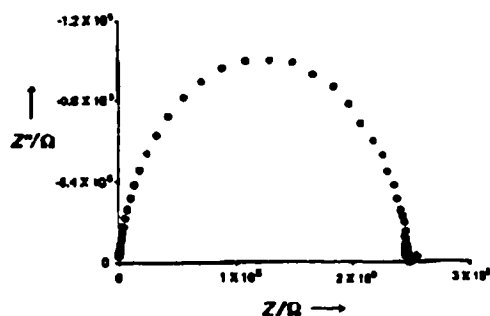


Figure 3. Complex impedance Argand plot for meso-NiO-YSZ with 22 wt % NiO recorded at 296°C in air.⁴⁷

Table 1. Conductivities σ [ohm⁻¹cm⁻¹] and corresponding activation energies E_a [kJ mol⁻¹] of mesoporous Pt (NiO)-loaded yttria-stabilized-zirconia.

	Pt-YSZ	Pt-YSZ	Pt-YSZ	Ni-YSZ	Ni-YSZ	Ni-YSZ
wt.%(Pt/NiO)	2	17	23	7	22	27
E_a	207	130	93	67	53	36
$\sigma(450^\circ\text{C})$	-	3.4×10^{-8}	5.5×10^{-5}	1.2×10^{-7}	6.2×10^{-6}	2.9×10^{-5}

The mixed oxygen ion-electron charge-transport was dominated by the non-stoichiometric nickel oxide nanocrystalline phase at low temperature around 400°C in the meso-NiO-YSZ and the enhanced NiO connectivity within meso-NiO-YSZ forms an electronic conduction pathway at far lower NiO content than in conventional materials (E_a , 80-100kJ/mol and little change in NiO content from 0-40 mol.%). However, the slightly higher activation energies for oxygen ion charge-transport in the meso-Pt-YSZ materials as compared to conventional Pt-YSZ were also observed maybe due to the nanocrystalline YSZ channel walls. These two materials represent a new class of solid

fuel cell electrode materials and show some of the first potential applications of mesoporous transition metal oxides.

1.1.2. Semiconducting Mesoporous Manganese Oxides

Since transition metal oxides have advantages over aluminosilicate materials due to their variable oxidation states and the presence of d-electrons in the walls of the structure, the direct chemical syntheses of mesoporous transition metal oxides with partially-filled d shells should lead to materials with unusual electronic, magnetic, and catalytic properties. However, most of the mesoporous transition metal oxides synthesized to date, including Ti,³² Nb,^{24,25} Ta,²⁸ W,²³ Zn,⁵⁰ V,⁵¹ Zr,²⁹⁻³¹ and Hf³³ are insulators containing high-valent transition metals in a single oxidation state. Recently Suib's group reported hexagonal and cubic phases of mesoporous manganese oxides with mixed oxidation states, synthesized using surfactants as mesostructure directing agents. These materials represented the first semiconducting mesostructures and possess catalytic activity in the oxidation of alkanes.³⁸ The mixed oxidation states (III/IV) of manganese in these materials result from the oxidation of the metal precursor Mn(OH)₂ (or Mn(OH)₆⁴⁺) by air during the synthetic process. The calcined samples prepared with higher surfactant concentration (28wt%) had hexagonally ordered manganese oxide channels (MOMS-1), while lower concentration (10wt%) of surfactant resulted in cubic mesostructures (MOMS-2). The argon adsorption isotherms of MOMS-1 and MOMS-2 gave BET surface areas of 170m²g⁻¹ and 46 m²g⁻¹, respectively, while the pore sizes and wall thicknesses were 30Å and 17Å respectively. The walls of the mesopores are composed of microcrystallites of dense phase of Mn₂O₃ and Mn₃O₄ (average oxidation states of Mn

in MOMS-1 is 3.55) with MnO_6 octahedra as the primary building blocks which are linked together by sharing edges. This is an important advance because most mesoporous materials possess amorphous walls, an undesirable feature in many catalyst supports. No other phases or amorphous manganese oxides were observed by TEM or XRD methods. The conductivities of MOMS-1 before and after calcination are $5.0 \times 10^{-8} \text{ ohm}^{-1} \text{ cm}^{-1}$ and $8.1 \times 10^{-6} \text{ ohm}^{-1} \text{ cm}^{-1}$ (band gap is 2.46 eV from UV spectra for the calcined material), respectively, while the conductivity of MOMS-2 is $2.28 \times 10^{-6} \text{ ohm}^{-1} \text{ cm}^{-1}$. These materials were the first semiconducting mesostructures and for this reason may have applications in photocatalysis or the fabrication of novel optic and electronic devices. Thermogravimetric analysis (TGA) and differential scanning calorimetry (DSC) demonstrated that both MOMS materials are stable at up to 1000°C. The Fourier transform infrared (FT-IR) data for pyridine adsorbed on calcined MOMS-1 indicate that there are two types of Lewis acid sites. This is further supported by the observation that MOMS-1 can act as active oxidation catalyst in the oxidation of cyclohexane and n-hexane to the corresponding alcohols in aqueous solutions.

1.1.3. Hierarchically Templated Mixed-Valent Molybdenum Oxides

In 1999 our group reported a semiconducting mesostructured mixed oxidation state molybdenum oxide, a material which selectively forms toroidal shapes with diameter of several hundred nanometers.⁵² This material was prepared by use of an as-synthesized dimeric molybdenum ethoxide complex with a bridging dodecylimido group as structure-constructing blocks and then hydrolyzing to generate bronze mesostructure Mo oxide.

The XRD pattern showed a high intensity peak (100) at $d = 32\text{\AA}$. The X-ray photoelectron spectrum (XPS) displayed Mo 3d_{5/2} emissions which could be simulated

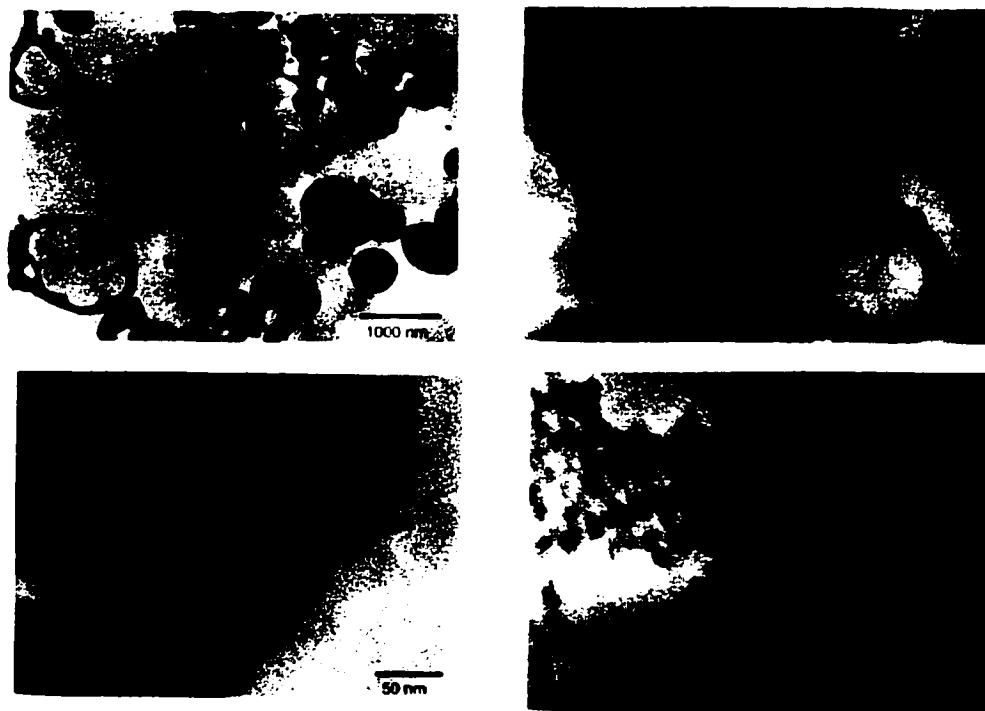


Figure 4. Transmission electron micrographs (TEM) of molybdenum oxide bronzes a) shown at low magnification revealing the toroidal structures of approximately 300 nm in diameter including regions in which several smaller toroids have clustered together inside a larger toroid. These living cell-like regions reorder into larger toroids upon exposure to the TEM electron beam, b) shown at higher magnification. The further-magnified inset reveals the mesostructured nature of the walls of the toroid. Scanning electron microscopy (SEM) revealed no salient structural features or tubular forms, indicating that these toroids are relatively flat (ca. 50 nm). Other areas of sample exist in which there is no higher order to the mesostructured system, although the toroidal regions dominate the material, c) lamellar region of the mesostructured molybdenum oxide blue showing that certain regions of the bronze have reordered into a layered phase in the blue, d) close up of a region of the molybdenum blue showing where crystallization of the walls of the mesostructure into oxide grains ca. 1.5 nm in size has led to partial degradation of the occluded mesopores.⁵²

as three peaks at 231.9 eV, 232.8 eV and 230.9 eV. The peak at 232.8 eV can be assigned to Mo(V), and the gap from valance band to Fermi level is 1.3 eV (band gap calculated from UV is 3.75 eV), providing evidence for weakly semiconducting properties in this material. The toroidal structures of this material, which are constructed of oriented mesotubules of roughly 50 nm in length and 3 nm in diameter, were revealed by transmission electron microscopy (TEM) images (Figure 4a). The toroidal shapes were thought to arise from a double templating interaction where the amine template forms both micelles and vesicles or microbubbles under the same conditions.^{53,54} Attempts to remove the template either by acid treatment or ozone treatment led to the formation of layered and amorphous materials respectively. Figure 4b provides evidence for an unusual dynamic process as observed by TEM in which adjacent toroids open up and coalesce into much larger toroids. This was the first example of dynamic behavior in such hierarchically-ordered materials and is a similar process to that observed in bundles of carbon nanotubes at high temperature.⁵⁵

When these bronze toroidal mesoporous materials were hydro-thermally treated in a sealed tube at 150°C for ten days, a phase changed to a new blue material consisting of 2-3 nm Mo (IV) oxide crystallites (Figure 4c), thought to arise from crystallization of the walls, and a mesolamellar Mo(VI) region (Figure 4d) as confirmed by XRD and TEM. The conductivity of this blue material is $6.3 \times 10^{-7} \text{ ohm}^{-1} \text{ cm}^{-1}$, higher than that of the bronze, possibly because of the presence of metallic Mo(IV) oxide. The XPS supports the presence of a metallic phase with a weak emission near the Fermi level. While MOMS mesoporous manganese oxide materials possess crystalline walls, in the case of these molybdenum oxide toroids, crystallization of the walls leads to collapse of both the

mesostructure and the macrostructure, suggesting that long range order in the walls in many cases may come at the expense of the porous structure.

1.1.4. Photocatalytic Activity of Mesoporous Niobium and Phosphated Titanium Oxides

An important area of application of mesoporous transition metal oxides is in photocatalysis. In the past decade, a variety of photocatalytic systems centered around oxidative degeneration of organic chemicals,^{56,57} fixation of carbon dioxide,⁵⁸⁻⁶⁰ evolution of H₂ from water,^{61,62} and reduction of metal ions⁶³ were developed using semiconducting transition metal oxides. Coupling the controlled pore size and high surface areas of mesoporous materials with photocatalytic properties would thus represent an important advance. Titanium dioxide, because of its efficient electron-hole pair separation and low cost, is one of the most desirable materials for photocatalytic applications. In 1998 Stone and Davis studied the photocatalytic activity of phosphated titania and niobia based mesoporous molecular sieves.⁶⁴ The well-known oxidative dehydrogenation of 2-propanol to acetone was used as a probe to measure the photocatalytic activity of the materials. The quantum yields were defined as the molecules of acetone formed per incident photon (about 360nm wavelength of light as incident light resource). The surface areas, band gaps, and quantum yields of the phosphated titania and niobia catalysts are summarized in Table 2.

Table 2. Characterization and reactivity results for titania and niobia materials.

Samples	Surface area (m ² g ⁻¹)	Band gap (eV)	Quantum yield
Meso-TiO ₂ (473K) ^a	712	3.19	0.0026
Meso-TiO ₂ (973K) ^a	90	3.25	0.0089

Meso-TiO ₂ , extracted	603	3.15	0.010
ns-TiO ₂ , as-synthesized	-	3.24	0.0094
ns-TiO ₂ (873K) ^a , 1h	39	-	0.022
ns-TiO ₂ (873K) ^a , 3h	36	3.22	0.038
ns-TiO ₂ (873K) ^a , 12h	28	3.26	0.27
Anatase (Aldrich)	9	3.28	0.41
Degussa P25	50	3.22	0.45
Meso-Nb ₂ O ₅	415	3.29	0.0041
Nb ₂ O ₅	13	3.08	0.217

^a Number in bracket is calcining temperature.

The lower photocatalytic activity of mesoporous titania and niobia compared to the anatase phase was attributed to the amorphous nature of the walls of these materials and the presence of phosphorous in the case of the titania materials: the low degree of crystalline wall and the high surface concentration of defects lead to surface electron-hole recombination, and/or the poisoning of catalytic surface sites by the phosphorus remaining from the templates. Since high surface area mesoporous titania is now readily available, the presence of phosphorous in these materials should no longer hinder applications,³⁶ although from these studies it appears that the low crystallinity of the walls of the structure may be a larger hurdle to overcome before the development of functional mesoporous titanium oxide photocatalysts can be realized.

1.1.5. Photocatalytic Activity of Mesoporous Tantalum Oxides

Takahara and Domen recently reported the photocatalytic activity of mesoporous tantalum oxide.⁶⁵ These studies were undertaken because Ta-based mixed oxides are

highly active in the overall decomposition of water under UV irradiation.⁶⁶⁻⁶⁸ When as-synthesized tantalum oxide, prepared by the method of Antonelli and Ying, was used as a photocatalyst, H₂ evolved in a speed of 50 μmol/h. In contrast, the sample calcined at 600K after template removal by acid treatment and solvent extraction showed higher photocatalytic activity and released both H₂ and O₂ in a stoichiometric ratio, even though a brief induction period was observed. The initial H₂ evolution was attributed to the decomposition reaction of the remaining surfactants and the stoichiometric evolution of H₂ and O₂ started after complete consumption of the surfactant template. A NiO loaded sample showed higher photocatalytic activity and shorter induction time than those

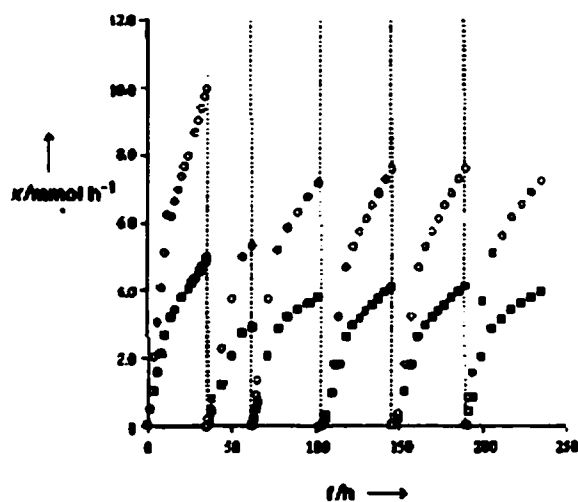


Figure 5. Time course of photocatalytic decomposition of water over NiO (4 wt%)-loaded mesoporous Ta₂O₅ after R673-0473 treatment: reduction at 673K by H₂ followed by reoxidation in O₂ at 473K.⁶⁵

samples without NiO since NiO can act as co-catalyst in the water decomposition reaction (Figure 5). The optimal NiO loading level for the overall water decomposition was found to be 4.0wt%. The NiO loaded samples showed an important trend in increasing photocatalytic activity. These results are summarized in Table 3.

Table 3. Comparison of the photocatalytic activity of NiO loaded tantalum oxides.

Tantalum oxides	Loading amount of NiO (wt %)	Pretreatment	BET surface area (m ² g ⁻¹)	H ₂ (μmol h ⁻¹)	O ₂ (μmol h ⁻¹)
Amorphous Ta ₂ O ₅	1.0	before	145	46	24
		after	NA	125	43
Orthorhombic Ta ₂ O ₅	1.0	before	NA	10	0
		after	NA	389	194
Mesoporous Ta ₂ O ₅	4.0	before	370	150	73
		after	141	515	272

Mesoporous Ta₂O₅ sample showed better photocatalytic activity than the non-porous amorphous and crystallized samples due to its higher surface area which results in higher NiO loading level. These high activities as compared to those reported above for titania and niobia⁶⁴ were explained by the different band gaps of the respective materials. The stable photocatalytic activity of pretreated mesoporous Ta₂O₅ with 4wt% NiO continued for more than 200 hours although the first run exhibited somewhat higher activity. From these results it is evident that mesoporous Ta oxides are effective photocatalysts and for this reason may spur a great deal of research interest over the coming years.

1.1.6. Alkali Reduced Mesoporous Niobium, Tantalum, and Titanium Materials

Recent work in our group showed that mesoporous Nb, Ta and Ti oxides can act as stoichiometric electron acceptors and hosts for a variety of electron-donating guest species, thus opening the doorway to a wide variety of reactions involving electron transfer to a mesoporous host lattice. This synthetic approach to achieving populated d-states in the walls of the mesostructure differs appreciably from previous approaches in

that the introduction of electrons into the d-band occurs *after* the mesostructure has been formed. The use of air sensitive low valent transition metal alkoxide precursors, which may well become oxidized during the course of mesostructure formation, can thus be avoided. In this work reduced transition metal molecular sieves⁴² were obtained by treatment of mesoporous Nb oxide with Na-naphthalene in THF (Figure 6).

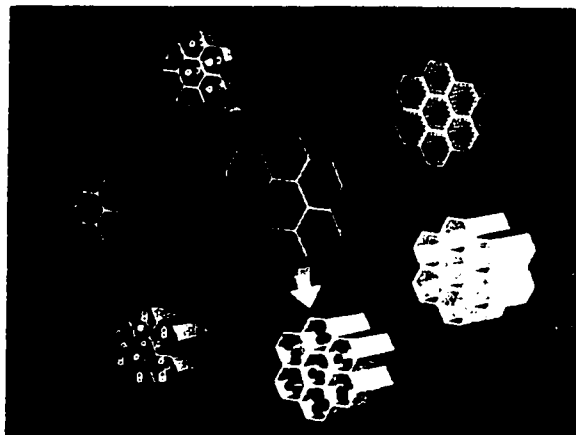


Figure 6. Reduction of mesoporous niobium oxide with: (a) bis(toluene) niobium to give a material with low valent Nb on the surface; (b) Na-naphthalene to give a reduced sodium niobate with potential applications as a cathodic material; (c) cobaltocene to give a material in which the mesostructure is filled with superparamagnetic molecular ensembles; (d) nickelocene to give a mesoporous spin glass; (e) K₃C₆₀ to give one-dimensional potassium fulleride wires supported by the mesoporous oxide lattice; (f) bis(benzene)chromium to give low dimensional organometallic hole metals in the pores.

The reduced materials were gray to black and showed full retention of mesostructure after reduction as determined by XRD and nitrogen adsorption. The XPS spectra showed that the Nb 3d 5/2, 3/2 emissions shift monotonically to lower binding energy with increasing reduction from 207.8 eV, 210.6 eV for the unreduced materials to 206.0 eV, 208.8 eV for the sample reduced with 1.0 equivalent of sodium naphthalene. This is consistent with a gradual change of the Nb oxidation state from Nb(V) to Nb(IV) as the

Na loading level increases. Two distinct peaks for Nb (IV) and Nb(V) were not resolved, possibly because of local electron hopping between sites faster than the XPS time scale. This initial work was then expanded to include all alkali metal reduced mesoporous Nb, Ta and Ti oxides.⁴³ The order of stability to reduction by alkali metal was found to be Ta > Nb >> Ti as judged by retention of the XRD pattern after reaction. The band gaps for all materials studied ranged from 3.3-4.0 eV and the distance from impurity band, thought to be composed of the transition metal nd [$n = 3(\text{Ti}), 4(\text{Nb}), 5(\text{Ta})$] and the alkali metal n's [$n' = 2(\text{Li}), 3(\text{Na}), 4(\text{K}), 5(\text{Rb}), 6(\text{Cs})$], to conduction band was roughly 2.1 eV as calculated from their UV spectra (Figure 7).

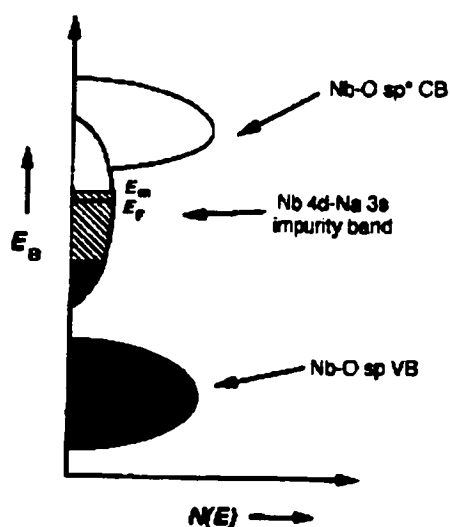


Figure 7. Energy-level diagram of alkali-reduced M-TMS1 ($M = \text{Ta}, \text{Nb}, \text{Ti}$). The electron from the alkali metal resides in an nd (transition metal)-n's (alkali metal) impurity band between the valence and conduction bands of the mesostructure. E_f denotes the Fermi level while E_m represents the mobility edge. Black areas are filled with electrons while the area marked by grid lines represents a region of localized states extending down into the (black) filled levels of the impurity band; CB = conduction band, VB = valence band.⁴³

Interestingly, all of the alkali metal reduced Nb and Ta oxide materials studied were insulating (less than $10^{-8} \text{ ohm}^{-1} \text{ cm}^{-1}$), while the Li-Ti material gave conductivity values of up to $10^{-6} \text{ ohm}^{-1} \text{ cm}^{-1}$. The insulating nature of the Ta and Nb materials was attributed to Anderson localization effects, a phenomenon studied in Na-reduced amorphous tungsten

oxides Na_xWO_3 .⁶⁹ Since the Li-Ti materials are semiconducting, an Anderson transition to a more continuous electronic state may have occurred. The superconducting quantum interference device (SQUID) magnetometry measurement of all of these materials showed evidence for paramagnetic behavior. The presence of free electrons in the structure was further supported by their electron paramagnetic resonance (EPR) spectra showing one peak close to free electron position ($g = 2.003$). The electrochemical studies on the unreduced Ti materials give a cyclic voltammogram with two clear peaks at 0.8 V and 1.4 V indicating reversible reduction-oxidation of the oxide framework, and possible applications in Li batteries. The stoichiometric retention of reductant with almost no loss of porosity gives these oxides a distinct advantage over other porous cathodic materials, which typically undergo a phase change to a non-porous state on addition of more than just a few tenths of an equivalent of alkali.⁷⁰ This is most likely due to the greater structural flexibility of the amorphous walls of mesoporous oxides as compared to the more rigid crystalline framework of other cathodic materials. In contrast, the unreduced Nb and Ta materials displayed very weak or no reversible electrochemical reduction-oxidation properties. The strong capacitance in these materials was attributed to charge mobility problems due to greater electron localization in the Nb and Ta materials than in the Ti materials.

1.1.7. Superparamagnetic Mesoporous Niobium Oxide-Cobaltocene and Nickelocene Composites

Of special interest is the intercalation of cobaltocene into mesoporous niobium oxide.^{71,72} Cobaltocene is a strong reductant and has a rich host guest inclusion chemistry

with many layered materials, such as sulfides and selenides, that can act as electron acceptors.⁷³ Recent work in our group shows that mesoporous Nb oxide readily reacts with cobaltocene to give a dark gray material (Figure 6C) which undergoes a dramatic change in magnetic properties on increased cobaltocene loading from paramagnetic to superparamagnetic behavior, a property which is normally only observed in the nanometer colloid grains of transition metals and their compounds. Interestingly, bulk Nb₂O₅ does not react with cobaltocene, demonstrating that the broader distribution of energy of the d-band in the amorphous mesostructure leads to a fraction of states which are low enough in energy to accept an electron from cobaltocene. The materials were characterized by XPS, and displayed Nb 3d 5/2, 3/2 emissions at 206.8 eV and 209.6 eV, indicative of slight reduction from Nb(V) to Nb(IV) state as compared to the starting materials at 207.6 eV and 210.4 eV, and the Co 2p 3/2 region in the sample prepared with more than 0.5 equivalent of cobaltocene showed two distinct cobalt peaks for cobaltocene and cobaltocinium at 779.7 eV and 781.1 eV respectively. The superparamagnetic materials have a Co/Nb molar ratio above a critical value of 0.5:1.0 and a blocking temperature (T_b) of 18K from SQUID plot of χ vs. T (Figure 8 curve a),

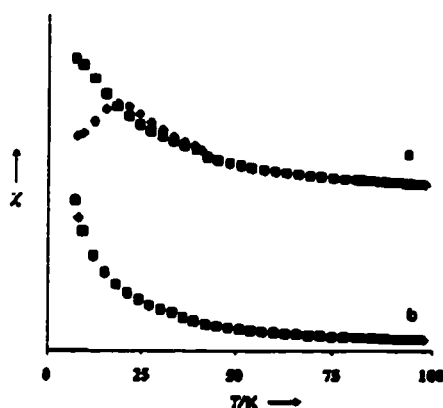


Figure 8. Temperature dependence of Magnetic susceptibility for Nb-TMS sample ($\mu =$ Zero Field Cooling, $n =$ Field Cooling) with (a) 0.5 equivalents of cobaltocene showing superparamagnetic blocking transition (T_b) at 18K; (b) 0.4 equivalents of cobaltocene showing no evidence of a superparamagnetic transition.⁷¹

below which the individual spins in the nanoscale magnetic domains are said to be blocked to certain low-energy transitions due to thermal fluctuations.⁷⁴ Materials with less cobaltocene were paramagnetic (Figure 8, curve b). The retention of neutral cobaltocene in the structure after the maximum level of cobaltocinium was reached was attributed to a strong host-guest interaction. This was the first reported example of superparamagnetism in a molecular ensemble. Recently superparamagnetism was also observed in Fe oxide based mesostructured surfactant composites,^{75,76} and it was attributed to small domains in the walls of the structure, not altogether surprising given that colloidal grains of many Fe-containing materials often display superparamagnetic properties. Since other reduced mesoporous oxides are not superparamagnetic, the origin of cooperative magnetism in this system must be related to the cobaltocene in the pores and short range coupling between the unpaired electrons associated with the Co centers. Whether or not the unpaired electrons in the walls of the structure interact with the spins of the Co species is not known at this stage. What makes this system particularly unusual is that bulk cobaltocene is paramagnetic and superparamagnetism is normally observed in small grains of materials which are ferromagnetic in their bulk form.

In order to investigate the factors contributing to superparamagnetism in this system, a study of variation of pore size, pore wall thickness and wall composition was conducted.⁷² The wall thickness and pore sizes were systematically varied from 15-30 Å and the 23-33 Å respectively, while the composition of the walls was varied from Nb, to Ta and Ti. M vs. T and B vs. H SQUID measurements were done for all materials. In all materials the mean particle size was estimated from the magnetic data to be about 14 nm.⁷⁷ The pore size and wall thickness of the mesostructure seemed to have little effect

on the magnetic behavior of these materials. The presence of cigar-shaped cobaltocene-based clusters within a single pore rather than spherical regions spanning several pore diameters was invoked to explain the 14 nm domain sizes, since some effect on the magnetic properties of increasing pore wall thickness would be expected if the pore walls were part of the magnetic domains. The samples synthesized from cobaltocene and Ta-TMS1 or Ti-TMS1 absorbed much lower levels of organometallic, mostly in the non-magnetic cobaltocinium form, and only displayed paramagnetic behavior. The lower levels of cobaltocene were attributed to the lower oxidizing ability of the walls of these materials as compared to the Nb-based structures. Thus, from this study it is evident that the host material must be reactive enough towards reduction by a guest species to first absorb a critical amount of cobaltocene in the pores in the cobaltocinium form. Once this critical level has been reached the materials absorb more cobaltocene, but this time in the neutral form. Once enough cobaltocene has aggregated in the pores, the materials undergo a transition to superparamagnetic behavior because of an increased density of unpaired electrons in the pore channels.

In order to investigate the effect of the overall spin of the guest species on the magnetic behavior of the system, we chose to synthesize mesoporous niobium oxide composites of metallocene species with more than one unpaired electron per nucleus.⁷⁸ Thus, new composite materials were prepared from nickelocene, which has two unpaired electrons per Ni center, and mesoporous niobium oxide (Figure 6). These materials showed an interesting loading-dependent transition from superparamagnetic (blocking temperature T_b at 8K) to spin glass behavior, a phenomenon normally associated with amorphous metal alloys in which the spins essentially become "frozen" in a random

orientation below a certain temperature. These nickel-based composites in general possessed a much lower loading level of organometallic species as determined by XPS (molar ratio of Ni:Nb was 0.07:1) than the cobalt-based composites. This result was rationalized by the greater number of unpaired electrons in Ni-based materials. That is, the ground state of nickelocene is a triplet and its cation is a doublet while cobaltocene is a doublet and its cation is a singlet. In a study of magnetic behavior of Fe-doped Pd alloys, a transition from the superparamagnetic state to the spin glass state was found to occur on increasing the concentration of the magnetically active species in the alloy.⁷⁹ The transition to the spin glass state in the nickelocene composites took place at the molar ratio of Ni:Nb in the amount of 0.1:1. Currently we are embarking on a series of more detailed magnetic studies in an effort to elucidate the origin of superparamagnetism and spin glass behavior in this new family of reduced mesoporous composites.

1.1.8. One Dimensional Alkali Fulleride Wires Supported by a Mesoporous Niobium oxide Host

Another family of electroactive mesoporous transition metal oxide materials recently reported by our group are the mesoporous niobium oxide intercalates of the superconductor K_3C_{60} (Figure 6).^{80,81} Since the electronic properties of alkali fullerides show a strong dependence on level of reduction,⁸² an important aspect of these materials is that the oxidation state of the fulleride phase in the pores can be easily tuned by addition of potassium naphthalene. The pore size of the mesoporous niobium oxide host material used in this study was 22 Å, just large enough to fit in one unit cell length (ca. 14 Å) of K_3C_{60} across the diameter of the pore. This feature allows us to investigate the

properties of one-dimensional alkali fullerides and the effects of quantum confinement on superconductivity and metallic properties of alkali fullerides in general. The reaction of K_3C_{60} and trimethylsilylated mesoporous niobium oxide in THF solution gave a material with alkali fulleride in the pores with an oxidation state of $n = 0.5$ as measured by its Raman spectra (for fulleride salts of the type M_nC_{60} ($M=K, Rb, Cs$), the A_g mode shifts roughly 6 cm^{-1} for every integer increment in the value of n).⁸² The reduction of the niobium mesostructure by the fulleride was illustrated by XPS spectrum, which indicated a level of reduction equivalent to that obtained by treatment of mesoporous niobium oxide with 0.4 equivalents of potassium naphthalene. The conductivity of this material was $1.25 \times 10^{-3}\text{ ohm}^{-1}\text{cm}^{-1}$, several orders of magnitude greater than that observed for a sample of fulleride-free mesoporous niobium oxide reduced with 0.4 equivalents of potassium naphthalene. This suggests that the conductivity pathway in this material is through the fulleride-units on the surface of the material or through the channels, and not through the niobium oxide walls of the structure. When this composite was further reduced by potassium naphthalene back to $n = 3$ state, the conductivity of this new material was lower than $10^{-7}\text{ ohm}^{-1}\text{cm}^{-1}$. No further reduction of niobium oxide walls of the mesostructure was observed in this process. Neither material showed signs of a T_c that might indicate a transition to superconducting behavior. This is not altogether unexpected given the strong dependence of superconductivity on structure in solids. EPR studies suggest that the fulleride phase and the free electron in the walls of the mesostructure are behaving as isolated systems. The room temperature conductivity patterns of these materials confirm some calculations that K_3C_{60} should be a Mott-Hubbard insulator because of its half-filled t_{1u} band⁸² and that the accidental vacancies in

the $n = 3$ state are responsible for the metallic behavior of bulk K_3C_{60} . However more structural information is necessary before any direct comparisons can be made to the bulk state.

In order to more fully probe into the dependence of room temperature conductivity on oxidation state of the fulleride in the pores, the parent composite with $n = 0.5$ was reduced in small increments up to $n = 4.5$, the process monitored by Raman and XPS. Interestingly, a double maximum at $n = 2.6$ and 4.1 state in the dependence of conductivity on oxidation state was revealed in this system.⁸³ The conductivity of the materials at these two states was $10^{-4} \text{ ohm}^{-1}\text{cm}^{-1}$ and $10^{-1} \text{ ohm}^{-1}\text{cm}^{-1}$ respectively. The maximum at $n = 2.6$ provides indirect evidence that the potassium fulleride phases other than $n=3$ state might be involved in the conductivity in bulk K_3C_{60} . The maximum at $n = 4.1$ is perhaps even more surprising since the room temperature conductivity of this composite is almost as high as pure K_3C_{60} and the $n = 4$ state is thought to be insulating.

The effects of pore size and wall composition of mesoporous transition metal oxides on the conductivity of the composites were also studied by expanding mesostructure hosts from Nb to Ti and Ta and the pore size to 32 \AA , large enough to accommodate two unit cells across a pore rather than only one. The results revealed that the double maximum behavior was general to other porous hosts, however the differences in the positions of the maxima were too subtle to draw any conclusions. The change in pore size seemed to have little effect, suggesting that a much more dramatic change in pore size might be necessary to affect the electronic properties. An interesting trend that emerged, however, was an increase in density of states near the Fermi level as measured by XPS in all the samples at the transition point to the conductivity maximum at ca. $n =$

4.0. This is consistent with a transition to metallic behavior, possibly involving a favorable overlap between the band structure of the walls and the fulleride phase, although we are currently doing variable temperature resistivity studies to confirm this hypothesis.

1.1.9. Electroactive Mesoporous Tungsten Oxides

Wei Cheng and coworkers recently reported the syntheses and electrochromic properties of mesoporous tungsten oxide films.⁸⁴ These materials were prepared via dip-coating using block copolymers as templates, a procedure that was developed by Stucky's group.^{85,86} The coating solutions consisted of a mixture of WCl_6 , anhydrous ethanol and tri-block polymer $EO_{20}PO_{70}EO_{20}$ (BASF Pluronic P₁₂₃), and either solvent extraction or calcination was used to remove the copolymer template. These materials were characterized by thermogravimetric analysis (TGA), XRD, TEM and nitrogen adsorption-desorption, giving compositions of $WO_{2.94} \cdot 2.8H_2O \cdot 0.011P_{123}$, $WO_{2.94} \cdot 1.3H_2O \cdot 0.001P_{123}$, $WO_{2.94} \cdot 0.8H_2O \cdot 0.0005P_{123}$ and $WO_{2.97} \cdot 0.17H_2O$ for the as-synthesized, solvent extracted, 300°C calcined and 400°C calcined samples, respectively. The mesostructures possessed fairly regular pore diameters but were not well ordered and generally collapsed at 400°C during calcination. The BET surface area for the solvent extracted and calcined (300 °C) samples were 155 and 135 m²g⁻¹ respectively and the corresponding average pore sizes were 50 and 45 Å.

Voltammetric measurements of the mesoporous tungsten oxide films showed a well-defined anodic peak for the samples calcined at 300°C and 400°C and well-behaved electrochemical reversibility after several cycles. The cyclic voltammograms of samples

calcined at 300°C showed the evolution of multiple anodic peaks during the repetitive insertion-desertion scans which could be due to the different types of hydrogen injection sites and/or the high surface area of the films. The electrochromic properties of mesoporous tungsten oxide were also studied. The optical change for the sample calcined at 300°C or sample extracted by ethanol during the voltammetric sweep was completely reversible (Figure 9), while tungsten oxide samples with low surface areas such as a sol-gel derived non mesoporous film heated at 300°C and the same sample heated at 400°C showed an irreversible coloration/bleaching process. This result was

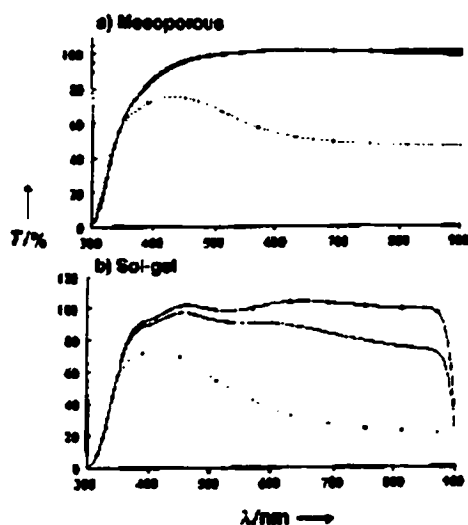


Figure 9. Optical transmittance spectra for a) mesoporous and b) sol-gel tungsten oxide films heated at 300 K. Solid line with triangles = initial; solid line = +0.8 V (1st charge); dotted line = -0.8 V (1st discharge).⁸⁴

further confirmed by the plots of transmittance variation at 650nm as a function of time in the experiment of the transient absorption response to voltage step. The coloration efficiency (CE) for mesoporous tungsten oxide film calcined at 300°C was 21.2 cm²C⁻¹ for the first cycle. The chronoamperometric measurements for voltage steps between -0.8V and +0.8V (vs. SCE) showed the mesoporous films possess better electrochemical stability than the sol-gel nonporous film. Therefore, the high surface area resulting from

the mesoporosity of the tungsten oxide films provides enhanced electrochemical and electrochromic properties.

1.2. Mesostructured Sulfides and Selenides

1.2.1. Mesostructured Germanium Sulfides

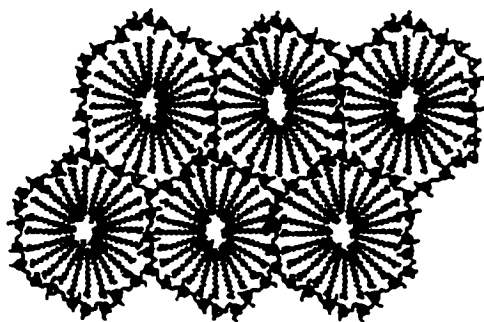


Figure 10. Proposed architecture of a mesostructured germanium sulfide material. $\text{TMA}_4\text{Ge}_4\text{S}_{10}$ and CTABr are dissolved in formamide to give a viscous mesophase of the adamantoid clusters charge balanced by surfactant. On addition of a metal salt, the adamantoid clusters link to form a supramolecular, hexagonal, mesostructured material in which the adamantoid clusters are linked by metal ions in the structure.

Because of their anticipated electronic and optical properties and affinities to heavy metals, researchers have recently been investigating the synthesis and potential applications of mesostructured sulfides and selenides. Ozin's group recently reported a new family of surfactant templated metal germanium sulfide materials with structures similar to that of as-synthesized MCM-41.^{41,87} Previously reported mesostructured chalcogenide composites such as CdS,⁸⁸⁻⁹⁰ ZnS,⁹¹ SnS₂,⁹² GeS₂⁹³ and CdSe⁹⁴ were prepared by Stupp and other researchers. The representative synthetic strategy was developed by Stupp via flowing H₂S or H₂Se over a hexagonal mesophase containing oligoethylene oxide oleyl ether [C₁₈H₃₅(OCH₂CH₂)₁₀OH], water and Cd(II) or Zn(II)

salts. In contrast, the mesostructured metal germanium sulfides synthesized in Ozin's group were synthesized by a non-aqueous surfactant-templating assembly of adamantanoid $[\text{Ge}_4\text{S}_{10}]^{4-}$ cluster precursors in formamide, where $(\text{TMA})_4\text{Ge}_4\text{S}_{10}$ (TMA = tetramethylammonium) was used as the inorganic precursor and $\text{C}_n\text{H}_{2n+1}\text{NMe}_3^+\text{X}^-$ ($n = 12, 14, 16, 18$ and $\text{X} = \text{Cl}^-, \text{Br}^-$) were used as structure-directing agents (Figure 10). Transition metal cations such as Co^{2+} , Ni^{2+} , Zn^{2+} or Cu^+ were employed as charge-balancing and inorganic framework-chain-linking ions to create well ordered hexagonal mesostructures.

The powder XRD patterns and TEM images of these materials illustrated a moderate degree of mesostructural order with wormlike morphologies and hexagonal unit cells (Figure 11). The Raman spectra of the mesostructured materials showed overlapping

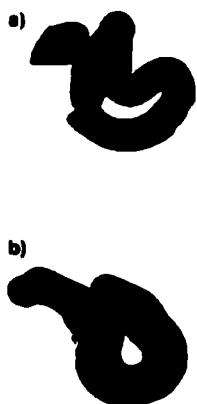


Figure 11. TEM images of worm-like particles of $(\text{CTA})\text{NiGe}_4\text{S}_{10}$. A magnified view of the particle in image b) confirmed that the channels of the material run parallel to the longitudinal axis of the faceted shape.⁸⁷

peaks between 240 and 320 cm^{-1} for the Zn-S stretching modes, confirming the presence of metal-linked adamantanoid clusters in the material. The solid state ^1H (MAS)NMR spectra and cross-polarization (CP) ^{13}C (MAS) NMR spectra confirmed the presence of the surfactant in the materials, as did thermogravimetric analyses (TGA) and pyrolysis mass spectroscopy. No sulfur-containing small molecules, such as H_2S , HSMe and

Me_2S , were observed in the mass spectra. The elemental analyses gave $(\text{CTA})_2\text{M}_2\text{Ge}_4\text{S}_{10}$ with 3-10 wt.% unaccounted mass for most of the samples. Only 40% of the surfactant in the materials could be removed by acetone extraction, indicating that the cationic surfactants CTA were functioning as charge-balancing reagents for the anionic framework as well as space-fillers to reinforce the mesostructure. A liquid-crystal templating mechanism was proposed to rationalize the formation of these materials. In this mechanism the terminal negative sulfide groups of the adamantanoid clusters in the initially formed micellar and cylindrical liquid-crystalline phase by $[\text{Ge}_4\text{S}_{10}]^{4-}$, TMA^+ , and surfactant cations could rapidly coordinate to the transition metal species to form a hexagonal mesostructured network. Because of the well-defined nature of the crystalline units in the walls of these materials, it is anticipated that numerous electronic and optical applications, in which a well-defined wall-structure is an advantage, may be possible.

1.2.2. More Germanium Sulfides and Selenides and even some Tin

At about the same time the non-aqueous synthesis of mesostructured metal germanium sulfides from $[\text{Ge}_4\text{S}_{10}]^{4-}$ clusters was being developed by Ozin's group, Kanatzidis and coworkers were working on the synthesis of related mesostructured metal germanium sulfides and selenides, $(\text{C}_n\text{H}_{2n+1}\text{NMe}_3)_2[\text{MGe}_4\text{Q}_{10}]$, where $\text{Q} = \text{S}$ and Se , $\text{M} = \text{Zn}$, Cd , Hg , Ni and Co , $n = 12, 14, 16, 18$,^{40,95} using a mainly aqueous route (with a small amount of ethanol and methanol). Certain aspects of the synthetic method, chemical formula, overall three-dimensional framework organization, and thermal stability of the materials are different from those reported by Ozin. The method developed by Kanatzidis involves the stoichiometric metathesis reactions between $[\text{Ge}_4\text{Q}_{10}]^{4-}$ ($\text{Q} = \text{S}$,

Se) anions and metal dichlorides in the presence of long chain cationic surfactants at 20-80°C. The charge on the $[\text{Ge}_4\text{Q}_{10}]^{4-}$ cluster was balanced by one M^{2+} and two surfactant RNMe_3^+ cations. Energy dispersive microprobe analysis (EDS) on the resulting material gave the chemical formula $(\text{RNMe}_3)_2[\text{MGe}_4\text{Q}_{10}]$, slightly different from the formula of the materials synthesized by Ozin.⁴¹ The powder XRD patterns, HRTEM images and atom pair distribution function (PDF) plots of these materials revealed a mesostructured

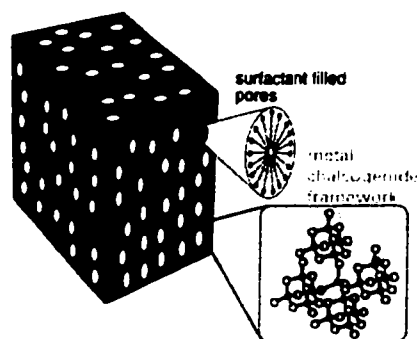


Figure 12. Proposed structure model of the C_nMGeQ phases. The amorphous framework is perforated by the worm hole-like micelles of surfactant molecules.

nature with short-range local order and non-periodic disordered wall structure much like that of mesoporous silica MSU-1/-2/-3.⁹⁶ The surfactant-filled inorganic framework pores were composed of adamantanoid $[\text{Ge}_4\text{Q}_{10}]^{4-}$ clusters with linking tetrahedral divalent transition metal ions, and organized in a worm hole pattern with a constant average tunnel to tunnel distance (Figure 12). The pore size could be tuned from 30-45 Å by varying the surfactant chain length and the overall structure of the $[\text{MGe}_4\text{Q}_{10}]^{2-}$ framework. The Raman and IR spectra of these materials showed that the adamantanoid clusters remained intact and gave evidence for additional M-Q bonds present. All materials were wide band gap semiconductors in the energy range of 1.0-3.6 eV and the band gaps were independent of the surfactant chain length. Based on the TGA, about 70-

80% of surfactant inside the inorganic framework could be removed without collapse of the mesostructure by heating at about 180-220°C under vacuum for 3-4 days.

Materials containing the divalent Mn^{2+} ion behaved differently and did not lead to an immediate precipitation in either the non-aqueous or aqueous mediums described above. This problem was resolved by conducting the reaction of $\text{Na}_4\text{Ge}_4\text{S}_{10}$, MnCl_2 , and mesityltrimethyl ammonium bromide in a stoichiometric ratio under hydrothermal conditions.⁹⁷ This method resulted in new hexagonally ordered mesostructures of metal germanium sulfides with only short-range local order similar to those reported by Ozin's group. The semiconducting properties of this material were confirmed by solid-state absorption spectra, giving a bandgap of 2.84 eV.

Trivalent cations such as Ga^{3+} and In^{3+} can also act as the cluster linking agents in these materials, leading to light emitting mesostructured sulfides with hexagonal order.⁹⁸ The mesostructure of these two materials were similar to the divalent counterparts and the optical absorption confirmed their semiconducting behavior. The chemical formula of both materials was close to $(\text{CP})_2\text{M}_{1.3}\text{Ge}_4\text{S}_{11}$ (CP = cetylpyridinium, $\text{M} = \text{Ga}^{3+}, \text{In}^{3+}$), indicative of a very high content of metal which could not be accounted for by charge balance among surfactant, metal cations and cluster anions, possibly due to the presence of S^{2-} species. A unique feature of these two materials was the intense photoluminescence observed when excited with light energy above their bandgaps. For example, under an excitation light of 3.35 eV (370 nm) at 77 K, an intense green emission with a maximum 2.35 eV (528 nm) and 2.32 eV (535 nm) was observed for CPGaGeS and CPInGeS respectively (Figure 13). The opto-electronic property possibly

originates from the pyridinium chromophore of the surfactant. This was the first observation of light emission from mesostructured metal thiogermanates.

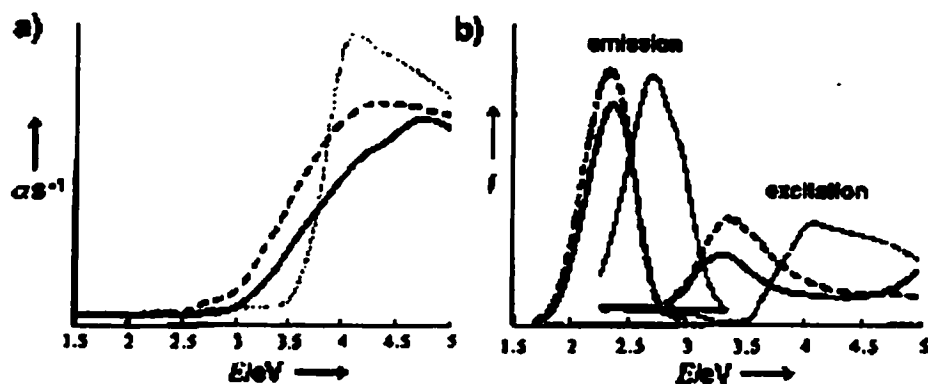


Figure 13. a) Electronic absorption spectra of mesostructured sulfides (dashed line = CPInGeS; solid line = CPGaGeS; dotted line = CPBr). αs^{-1} : in arbitrary units. b) Photoluminescence and excitation spectra of materials from a) (solid line = CPGaGeS; dashed line = CPInGeS; dotted line = CPBr). Intensity I: in arbitrary units.⁹⁸

This methodology of supramolecular assembly of chalcogenide nanocomposites could be expanded to synthesize stable binary system including $[Fe_4S_4]$ and $[Ge_4Q_{10}]^+$ (Q = S, Se) clusters as building blocks for the inorganic frameworks.⁹⁹ The cluster $[Fe_4S_4]$ was selected as a research target because it is exceptional and ubiquitous in biological systems, providing a major part of the foundation for electron transfer, catalytic, and enzymatic processes in living organisms.¹⁰⁰ This material possessed hexagonal mesoscopic order and was prepared in the non-aqueous solvent mixture of formamide and dimethyl formamide (DMF). This general method has opened a doorway for preparing a stable hybrid system with multiple functionality.

Another new class of mesostructured selenide semiconductors with an open framework based on tetrahedral $[SnSe_4]^{4-}$ anion was reported recently by the same

group.¹⁰¹ These materials are important not only because of their interesting electronic properties but also because of their varied pore organization, including disordered worm-hole, hexagonal and even cubic phases. It was known that $[\text{SnSe}_4]^{4-}$ possessed the same tetrahedral structure as $[\text{SiO}_4]^{4-}$ and that it was smaller and heavier than the $[\text{Ge}_4\text{Q}_{10}]^{4-}$ (Q=S, Se) clusters. Therefore, it was expected that a similar topological structure to silicas and semiconductors with narrower bandgaps than metal germanium chalcogenides would be obtained. These materials were made by spatially controlled assembly of $[\text{SnSe}_4]^{4-}$ anions in formamide with various divalent metals such as Mn^{2+} , Fe^{2+} , Co^{2+} , Zn^{2+} , Cd^{2+} and Hg^{2+} in the presence of cetylpyridinium surfactant as the template. Their general chemical formula were described as $(\text{CP})_{4-2x}\text{M}_x\text{SnSe}_4$ (where $1.0 < x < 1.3$). XRD patterns and TEM images revealed that, under the same experimental conditions, all the materials had hexagonal mesostructures like silica MCM-41 except the Zn analogue, which had a cubic mesostructure like MCM-48. The structure of the Zn materials was dependent on the surfactant concentration. When the concentration was reduced by 50%, the product had an hexagonally ordered mesophase with uniform pore size. The presence of the tetrahedral $[\text{SnSe}_4]^{4-}$ anion clusters was demonstrated by ^{119}Sn Mössbauer spectroscopy. The UV-visible/ near-infrared spectroscopy showed the band gap transition in the energy range of 1.4-2.4 eV, values similar to those of CdTe (1.45 eV) and GaAs (1.54 eV) semiconductors. In summary, while these materials are not yet completely stable to template removal, their fascinating array of ordered structures and unusual optico-electronic properties may lead to applications in which accessible internal void space porosity is not a requirement.

1.3. Mesostructured Metals

1.3.1. Mesostructured Platinum



Figure 14. SEM image of a washed sample of mesoporous platinum (top) and TEM image of H₁-platinum (bottom). The material was suspended in acetone, sonicated for 5 min and applied to a carbon-coated copper grid.¹⁰²

Due to the importance of zero valent transition metals in many catalytic processes the synthesis of nanostructured metals with high surface areas and controlled porosity represents a significant challenge for materials scientists. In 1997 Attard and coworkers reported the aqueous syntheses of mesostructured metallic platinum via surfactant liquid crystal templating.¹⁰² In this work, hexachloroplatinic acid (H₂PtCl₆) and ammonium tetrachloroplatinate [(NH₄)₂PtCl₄] were employed as the metal source and octaethyleneglycol monohexadecyl ether [C₁₆(EO)₈] as the hexagonal structure-directing agent. In order to obtain mesostructured platinum metal, pure Fe, Zn, Hg, or hydrazine hydrate, were applied *in situ* as reducing agents after the self-assembly processes for the system H₂PtCl₆ and (NH₄)₂PtCl₄, respectively. The surfactant template, metal residues and small molecules were removed by repetitive washes with acetone, water and hydrochloric acid until TGA showed almost no further weight loss at up to 600°C in air.

SEM images revealed that the materials were composed of particles 90-500 nm in diameter, and TEM showed evidence of small grains possessing a hexagonal mesostructure with a pore size of 30Å and a pore wall thickness of 30Å (Figure 14). These results were consistent with the broad and poorly defined XRD pattern, indicative of either small domains of hexagonal order or large amorphous regions in the sample. No nitrogen adsorption data was presented in this work. The extended X-ray absorption fine structure (EXAFS) data obtained for the platinum L_{III} edge of the materials were in good agreement with the presence of pure platinum metal and no oxygen backscattering shells were found. The lower amplitude and corresponding decrease in coordination number of mesoporous platinum than those of bulk metallic platinum also revealed by EXAFS could be attributed to high surface area for the mesoporous materials, although no nitrogen adsorption data was reported. In a subsequent paper, this technique was extended to the synthesis of thin films,¹⁰³ and nitrogen adsorption studies revealed surface areas of 23 m²g⁻¹, comparable to that of colloidal Pt. The proposed mechanism of mesostructure formation in this new class of materials involved stabilized metal precursors at the interface between the hydrophobic and hydrophilic domains of the microphase-separated environment. Then the fast reduction of the platinum salts yielded small colloidal primary metallic particles on the interface followed by agglomeration and coalescence until the walls become homogeneous. This interesting new method has recently been extended to liquid crystal template syntheses of Ru/Pt alloys¹⁰⁴ and shows promise as a general method towards mesostructured metallic materials which may find applications in catalytic hydrogenation and fuel cell design.

1.3.2. Metal Carbonyls as Mesostructure Building Blocks

In 1998, Antonelli and co-workers attempted the synthesis of mesoporous Pt using metal carbonyl anions and cationic surfactants as building blocks with thermal or photolytic decomposition of the resulting self-assembled platinum carbonyl-surfactant phases required to eliminate the carbon monoxide and leave behind the pure metal mesostructure.¹⁰⁵ While this work resulted only in the formation of layered phases, it is included in this review because of the novelty and potential promise of this new synthetic method. Ionic metal carbonyl clusters ($\text{Na}_2[\text{Pt}_3(\text{CO})_6]_n$, $n = 3-5$) were selected as building blocks due to the great flexibility of composition, size, average charge per Pt atom, and the relative ease of thermal decomposition to pure metallic state. Trimethyl ammonium surfactants were employed as structure directing agents (Figure 15).

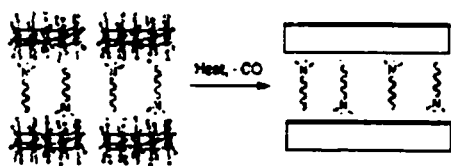


Figure 15. Thermal treatment of layered platinum carbonyl phases results in loss of CO and formation of a new platinum-based layered material.¹⁰⁵

The interdigitated layered structure of these materials was revealed by XRD. The layered structure was further confirmed by TEM images, which showed small regions of local order. Changes in the metal-to-surfactant ratio, brought about by simply changing the size of the metal carbonyl cluster, or precipitation directly from cold methanol without the addition of degassed water, had no effect on changing the nature of the layered mesophase. Thus no hexagonal or cubic phases were observed. Elimination of CO from the as-synthesized materials by heating at 70°C under dynamic vacuum resulted

in the retention of the structure with only a slight shrinkage of the interlayer spacing with a $d(100)$ going from 19.6 Å to 19.1 Å. The lack of regularly spaced gaps between the platinum units within each layer suggested that the individual platinum clusters had condensed together or that the gaps were too small to be observed. The elemental analyses and ^{13}C MAS NMR spectra confirmed the presence of surfactant in this material. No platinum oxide was observed by energy dispersive X-ray spectra (EDS). Further heating of this material at 120°C for two days led to loss of the layered structure and formation of an amorphous phase. While only layered materials were formed, this study demonstrated that metal carbonyl anions could be used as precursors to pseudo metallic phases, the loss of CO and condensation of the walls on thermal or photolytic treatment being related to the loss of water and formation of metal oxygen bridges in the sol-gel synthesis of metal oxides.

1.4. Summary and Outlook

From the contents of the above review it is clear that the area of mesoporous non-silica materials has expanded significantly in the last several years and that real-world applications of these exciting materials may not be too far off in the future. By offering controlled porosity, large accessible internal surface areas and void space, in combination with the variable oxidation states of transition metals or semiconducting behavior of sulfides and selenides, this class of materials possess many crucial properties that hitherto have not been possible in zeolites or mesoporous silicates. Already functional materials in this class have been developed for use in photocatalysis, fuel cells, catalytic oxidation, and reduction, while many other applications are no doubt forthcoming. Moreover, the

propensity for mesoporous transition metal oxides to act as stoichiometric electron acceptors, making them obvious candidates for cathodic materials, has allowed for the exploration of new one-dimensional hole-doped molecular metals with unusual electronic and magnetic properties not observed in the bulk state of these materials. Therefore, this thesis will mainly present the synthesis, electronic and magnetic properties of low-dimensional organometallics reduced mesoporous niobium oxide composites.¹⁰⁶⁻¹⁰⁸

Chapter 2. Electronic Properties of Novel Mixed Oxidation-State Bis-Arene Chromium Nanowires Supported by a Mesoporous Niobium Oxide Host

Research in our group has shown that mesoporous niobium oxide (Nb-TMS1) can act as an electron acceptor while fully retaining its mesostructure.⁴² Not only is this property important in the fabrication of fast ion conduction materials¹⁰⁹ for solid electrolyte and battery applications, yet it also allows the host oxide framework to act as an electron receptacle in a wide variety of electrochemically-active guest species. While mesoporous M41S silicates^{5-8, 10} do not exhibit flexible oxidation state behavior, M-TMS1 (M = Nb, Ta, Ti)^{24,25,27,28,32,35} materials have the potential to be readily reduced by a wide variety of metallic and organometallic species to lead to a new family of mixed-oxidation state intercalates with interesting electronic and magnetic properties. The beauty of this transition-metal-oxide-based system is that not only may the pore size be varied to allow for intercalation of nanophases of different diameters, but also that the propensity for the walls to act as an electron acceptor can be tuned by doping the walls with metal ions more strongly oxidizing than Nb(V). This allows control over both the size and electronic structure of the guest phase. While mesoporous materials synthesized from semiconducting Mo⁵² and Mn³⁸ oxides have previously been reported, there are as yet no studies published on the behavior of these materials on electrochemical reduction.

In this study it will be shown how mesoporous niobium oxide can absorb bis-arene chromium species to obtain mixed oxidation state Cr(0)/Cr(I) molecular nanowires with conductivities much greater than those observed for the analogous materials reduced with

alkali or cobaltocene⁷¹. This suggests that mixed-oxidation state bis-arene transition metal complexes can act as molecular metals when confined by a mesostructured host.

2.1. Experimental Section

2.1.1. Materials and Equipment

All chemicals unless otherwise stated were obtained from Aldrich. Samples of mesoporous niobium oxide (Nb-TMS1) were synthesized by the method of Antonelli and Ying²⁴ and used without further purification. Chlorotrimethylsilane was obtained from Aldrich and distilled over calcium hydride. Nb-TMS1 samples were dried at 100 °C overnight under vacuum and then stirred with excess Chlorotrimethylsilane in dry ether for 12 h under nitrogen. Nitrogen adsorption and desorption data were collected on a Micromeritics ASAP 2010. X-ray diffraction (XRD) patterns (CuK α) were recorded in a sealed glass capillary on a Siemens D-500 θ -2 θ diffractometer. All X-ray photoelectron spectroscopy (XPS) peaks were reference to the Carbon C-(C, H) peak at 284.8eV and the data were obtained using a Physical Electronics PHI-5500 spectrometer using charge neutralization. Conductivity measurements were recorded on a Jandel 4-point universal probe head combined with a Jandel resistivity unit. The equations used for calculating the

resistivity were as follows: for pellets of <0.5mm thickness: $\rho = \left(\frac{\pi}{\log n^2} \times \frac{V}{I} \right) t$

For pellets of >0.5mm thickness the following equation is used: $\rho = 2\pi(S) \frac{V}{I}$

Where ρ = resistivity; $\frac{\pi}{\log n^2}$ = sheet resistivity; V = volts; I = current; t = thickness of

the pellet; S = the spacing of the probes (0.1cm).

The powder UV-visible spectra were collected on an Ocean Optics S2000 fiber optics spectrometer equipped with an Analytical Instrument Systems Light Source emitter with a tungsten halogen lamp and an Ocean Optics UV 0.4mm, 2M reflection probe. The powder electron paramagnetic resonance (EPR) samples were prepared under vacuum and the data collected on a Bruker X-band ESP 300E EPR spectrometer. Magnetic measurements were conducted on a Quantum Design SQUID magnetometer MPMS system with a 5 Tesla magnet. All elemental analysis data (conducted under an inert atmosphere) were obtained from Galbraith Laboratories, 2323 Sycamore Drive, Knoxville, TN 37921-1700.

2.1.2. Synthesis

To a suspension of the Nb-TMS1 in dry benzene was added excess bis(benzene) chromium calculated on the basis of metal percent as determined from elemental analysis. The mesoporous solid immediately went from a light faun color to a grey-black. After several days and additional stirring to ensure complete absorption of the organometallic, the reduced material was collected by suction filtration and washed several times with benzene. Once synthesized, the material was dried *in vacuo* at 10^{-3} torr until all condensable volatiles had been removed. All other reduced oxides in this study were prepared in an analogous fashion. The elemental analysis gave values of 53.12% Nb and 2.57% C for the trimethylsilated mesoporous niobium oxide, and 51.36% Nb, 8.30% C and 2.02% Cr for the material after treatment with excess bis(benzene) chromium.

2.2. Results and Discussions

2.2.1. X-ray Powder Diffraction Pattern and Nitrogen Adsorption Studies

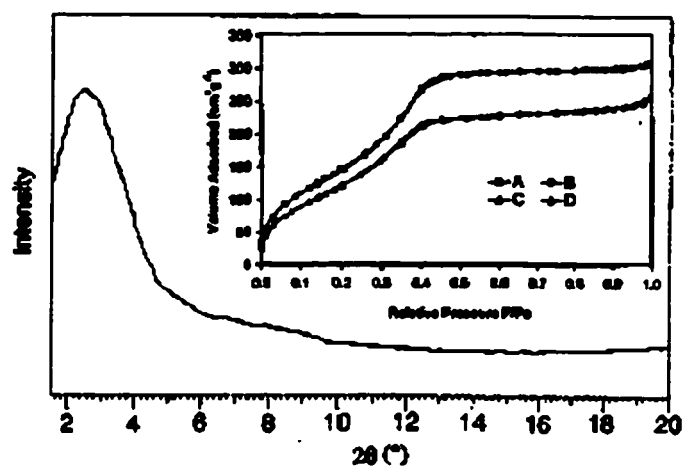


Figure 16. X-ray powder diffraction pattern (Cu K α) of a sample of mesoporous Nb oxide after treated with excess bis(benzene) chromium. The inset shows the nitrogen adsorption (A, C) desorption (B, D) isotherms of the material before (A, B) and after (C, D) reaction with excess bis(benzene) chromium.

When a sample of trimethylsilated mesoporous Nb oxide of Horvath-Kowazoe (HK) pore size 28 Å and a surface area of 580 m²g⁻¹ and a pore volume of 0.499 cm³g⁻¹ is treated with excess (C₆H₆)₂Cr in benzene an immediate reaction occurs which leads to darkening of the oxide to a deep grey-black color. This new material is collected by suction filtration under nitrogen and washed with dry benzene until the filtrate is colorless. The X-ray powder diffraction pattern of this material (Fig. 16) shows a strong peak at $d = 38\text{Å}$, virtually identical to that of the starting material, indicating that the mesostructure has been fully retained. The nitrogen adsorption isotherm of this material is shown in the inset of Fig. 16 and further supports the retention of mesoporosity with a sharp decrease in surface area from 580 m²g⁻¹ to 482 m²g⁻¹ as expected from intercalation of the organometallic into the pore structure of the material. The HK pore size of the new material was 25Å, consistent with a slight occlusion of the pores by the intercalated

species and the pore volume dropped from $0.499 \text{ cm}^3\text{g}^{-1}$ to $0.433 \text{ cm}^3\text{g}^{-1}$. These results are in accord with previous work in our group, which showed that the mesostructure of mesoporous niobium oxide is fully retained on reduction by electron-donating host species.⁴² Elemental analysis of this material revealed that the maximum Cr/Nb ratio calculated on the basis of 2.02% Cr was 0.07:1, significantly lower than that observed for the analogous cobaltocene intercalates. There was also an increase in the value of carbon by 5.73%, consistent with retention of the structural integrity of the organometallic without decomposition to chromium metal or chromium oxide. The lower loading levels of the bis-benzene chromium with respect to cobaltocene suggests that not only does the hydrophobicity of the internal cavity effect the maximum loading level and host-guest encapsulation affinity of the organometallic as previously discussed,⁷¹ but also that the more weakly-reducing Cr complex has a lesser tendency to be absorbed into the mesostructured host. Interestingly, bulk crystalline Nb_2O_5 does not react with cobaltocene or bis-benzene chromium. The higher reactivity of the mesoporous oxide can be explained by the amorphous nature of the walls of the material and the fact that amorphous materials have a much broader distribution of electronic states than their crystalline counterparts and these states are often highly localized with potentials both higher and lower than that in the crystalline state.⁶⁹

2.2.2. Ultraviolet (UV)-Visible Reflectance Measurements

The UV-visible reflectance measurements of the material synthesized with a Cr:Nb ratio of 0.07:1 shows a complex series of absorbancies from 200 nm to 800 nm which can be explained as a sum of the previously reported Nb-O sp absorbance at 260 nm,^{42,38} the $(\text{C}_6\text{H}_6)_2\text{Cr}$ metal-ligand charge transfer absorbance at 340 nm, the $[(\text{C}_6\text{H}_6)_2\text{Cr}]^+$ metal

ligand charge transfer absorbancies at 280 nm and 370 nm, and the impurity band absorbance at 580 nm, corresponding to a band gap of 3.3 eV and broadly similar to that reported for the related sodium and cobaltocene intercalates. These data suggest a mixed-oxidation state configuration for the encapsulated phase with both $(C_6H_6)_2Cr$ and $[(C_6H_6)_2Cr]^+$ present in the pores and further confirms the retention of structural integrity of the organometallic upon intercalation into the mesostructure.

2.2.3. Electron Paramagnetic Resonance (EPR) Spectroscopy

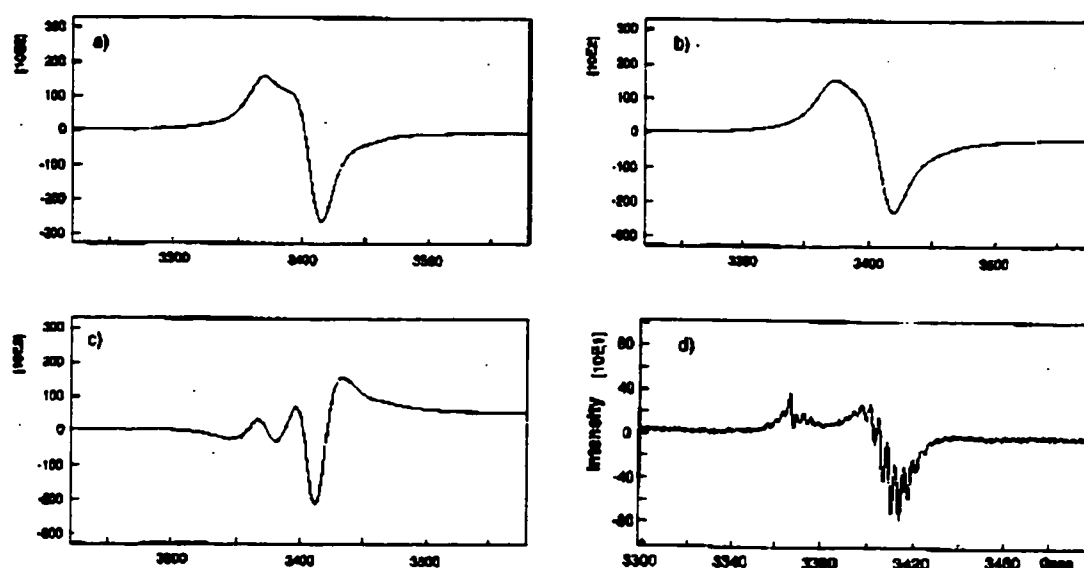


Figure 17. Powder EPR spectrum of (a) a sample of mesoporous niobium oxide treated with 0.07 equivalents of bis-benzene chromium, (b) material in a) after air oxidation, (c) difference spectrum between (a) and (b), and (d) a sample of trimethylsilated mesoporous niobium oxide treated with 0.001 equivalents of bis-benzene chromium. Scale is Gauss versus arbitrary intensity.

Figure 17a shows the powder electron paramagnetic resonance spectra of the material with a Cr:Nb ratio of 1:0.07. The stronger peak at 3404G ($g = 1.985$) is due to the $[(C_6H_6)_2Cr]^+$ a_{1g} electron, in complete accord with previous EPR studies on this

compound, while the second resonance at 3369G ($g = 2.00$) is due to unpaired electrons in the wall of the mesostructure. This peak falls at the same position as that previously reported for the sodium-reduced materials.⁴² Figure 17b shows the spectrum of the sample in (a) after oxidation in air for 30 min. In this spectrum, only the resonance due to $[(C_6H_6)_2Cr]^+$ can be clearly observed. Figure 17c shows the reduced difference spectrum of those shown in (a) and (b). The peak at 3369 G is due to the diminished EPR signal of the free electrons in the wall while that at 3404 G is due to the decreased amount of $[(C_6H_6)_2Cr]^+$ in the sample. Figure 17d shows the spectrum of a dilute sample of $(C_6H_6)_2Cr$ in mesoporous niobium oxide showing an x, y peak for the $[(C_6H_6)_2Cr]^+$ cation centered at 3404 G with clear proton hyperfine splittings ($\alpha_H = 3.43G$, $g = 1.98$) in addition to a z-peak as previously noted.¹¹⁰ and overlaps with the peak expected for the free electron in the Nb mesostructure. The absence of hyperfine splittings in the spectrum shown in Figure 17a is a well-documented concentration effect brought about by the higher dilution of $[(C_6H_6)_2Cr]^+$ in the sample from Figure 17d with respect to the former. These data are all consistent with a mixed-oxidation-state bis-arene chromium phase encapsulated by reduced niobium oxide walls.

2.2.4. Conductivity Measurements

Conductivity measurements on samples of the bis-arene chromium intercalates measured by the four point method under nitrogen showed that these materials are semi-conducting with conductivity values as high as $10^{-5} \text{ ohm}^{-1}\text{cm}^{-1}$. These values are comparable in magnitude to mesoporous niobium oxide potassium fulleride intercalates⁸⁰ and 100 times greater than the corresponding cobaltocene or sodium intercalates and compare favorably to values obtained for polyaniline wires in a mesoporous silica host.¹¹¹

Samples of this material left in air until there is no spectroscopic evidence for $(C_6H_6)_2Cr$ show very low conductivity, suggesting that this species is necessary for conductivity to occur. Since pure $(C_6H_6)_2Cr$ is insulating it is likely that the conductor is the hole introduced in the singly degenerate $Cr a_{1g}$ band of the neutral phase by partial oxidation of Cr (0) to Cr(I) by the Nb oxide framework (Figure 18) leading to a mixed oxidation state Cr(0)/Cr(I) phase. This partially filled band model is commonly used to explain conductivity in molecular metals and doped polymeric semiconductors.⁶⁹

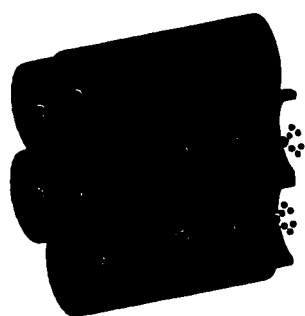
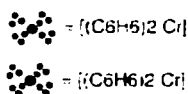


Figure 18. Schematic representation of bis-benzene chromium molecular nanowires in a mesoporous niobium oxide host illustrating the mixed oxidation state formulation of the material.



Decreasing the pore size from 28 Å to 23 Å had no effect on the conductivity levels while materials with lower loading levels of 0.03 equivalents showed conductivity of a similar magnitude. At a loading level of less than 0.007 equivalents of Cr the conductivity dropped to less than $10^{-7} \text{ ohm}^{-1}\text{cm}^{-1}$, indicating that a critical loading level somewhere between 0.03 and 0.007 equivalents is necessary for conductivity to occur.

2.2.5. X-Ray Photoelectron Spectroscopy

To more fully probe the mixed oxidation state nature of these materials, X-ray photoelectron spectroscopy (XPS) was conducted since it is a sensitive technique to

elucidate the different species present in the sample and the degree of reduction of the niobium oxide framework. Figure 19a shows the Nb 3d 3/2,5/2 region of the XPS

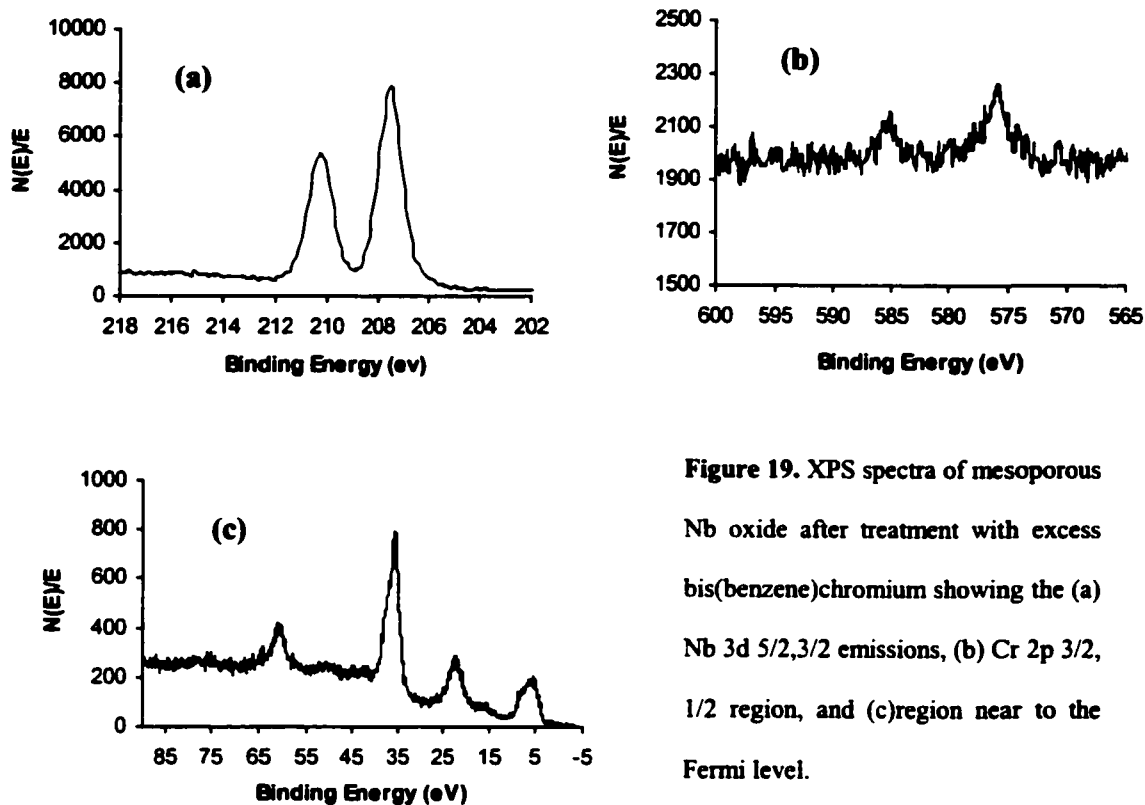


Figure 19. XPS spectra of mesoporous Nb oxide after treatment with excess bis(benzene)chromium showing the (a) Nb 3d 5/2,3/2 emissions, (b) Cr 2p 3/2, 1/2 region, and (c) region near to the Fermi level.

spectrum of the sample prepared with a Cr:Nb ratio of 0.07:1. The position of the peak at 207.6 eV is consistent with an average level of reduction of the niobium framework of less than 0.1 equivalents as compared to samples reduced with increasing amounts of sodium. The Cr 2p region of the spectrum is shown in Figure 19b and shows a major peak at 575.7 eV, consistent with the presence of neutral $(C_6H_6)_2Cr$ in the pores and in complete accord with previous XPS studies on this species.¹¹² The expected peak at 577.7 eV for the species $[(C_6H_6)_2Cr]^+$ confirmed by EPR is not resolved, indicating the Cr(0)/Cr(I) ratio is largely in favor of the neutral species. This exact ratio is difficult to

determine due to the low loading level of Cr and the sensitivity of the XPS technique. The valence region near the Fermi level (Figure 19c) shows the region of low binding energy with a distance to the Fermi level of 2.5 eV, similar to that observed in related reduced mesoporous materials. The Nb 4s (59 eV), Nb 4p (35 eV), and O 2S (22 eV) are also visible.

2.2.6. Superconducting Quantum Interference Detector (SQUID) Measurements

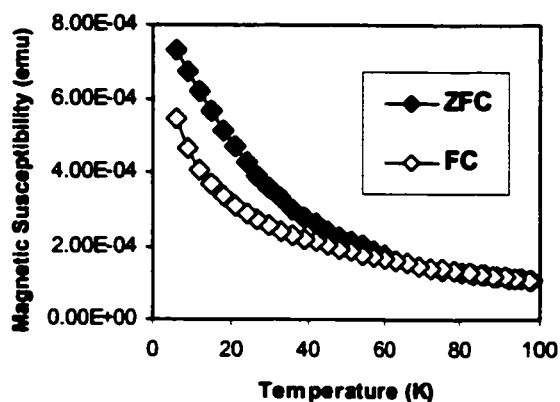


Figure 20. Plot of magnetic susceptibility (emu) vs. temperature run on a Quantum Design SQUID magnetometer at 500 Gauss for Nb-TMS1 sample with 0.07 equivalents of bis(benzene) chromium.

SQUID magnetic measurements of the material prepared with 0.07 equivalents of Cr are consistent with paramagnetic behavior expected from the unpaired electrons in the mesostructure walls. Figure 20 shows a plot of magnetic susceptibility versus temperature recorded at 500 Gauss. There is a small hysteresis between the zero-field-cooling (ZFC) and field-cooling (FC) branches of the plot. The degree of this hysteresis decreases with the loading level of $(C_6H_6)_2Cr$, although there is little change in the shape of the curve with decreasing field. The hysteresis can be attributed to the broad distribution of particle sizes in the mesoporous oxide, which gives a wide range of roughly spherical particles from 50-1000nm, and glass spin behavior at low temperature.¹⁰⁶ The paramagnetic property of this material was further confirmed by the

measurements of magnetic susceptibility versus magnetic field, which gave a straight line passing the original dot. However, in contrast to the cobaltocene materials, there was no evidence of superparamagnetic^{71,113} behavior in this system. In the cobaltocene analogues a paramagnetic-to-superparamagnetic transition was observed at a loading level of 0.8:1 Co:Nb. As previously mentioned, the Co level is more than ten times greater than the maximum loading level in the Cr system. The dependence of superparamagnetism on loading in the Co system was explained on the basis of the need for a critical particle size of the paramagnetic species within the pore before superparamagnetism ensues. Thus either the loading level is too low in the Cr system, or the electronic configuration of the Cr nuclei is not favorable for the onset of superparamagnetic behavior.

2.3. Conclusions

In summary, we have synthesized a new class of one-dimensional conducting molecular nanowires by intercalation of $(C_6H_6)_2Cr$ into a reducible niobium oxide mesostructure. The oxidizing nature of the walls allows for the presence of mixed oxidation state organometallic phases within the pores. This feature leads to unusual magnetic and electronic effects and shows promise for model systems for the study of quantum confinement effects on molecular metals. Because mesoporous Nb oxide can readily be doped with more strongly oxidizing species than Nb(V), this system also shows the potential for tuning the degree of electrons in the conduction levels of molecular metals intercalated in the pores, an attribute which is crucial to metallic behavior in these materials.

Chapter 3. Synthesis and Electronic Properties of Low-Dimensional Bis(benzene) Vanadium Reduced Mesoporous Niobium Oxide Composites

In the Chapter 2, it has been shown that the mixed-valence bis(benzene) chromium phases in the pores of Nb-TMS1 are highly conductive, suggesting that oxidation state defects in metallocenes may lead to metallic behavior.¹⁰⁶ In order to further probe into the nature of low dimensional bis-arene phases supported by mesoporous transition metal oxide hosts, in this report I synthesized related bis(benzene) vanadium composites and investigated their electronic properties.¹⁰⁷ Since conductivity in solids is partially dependant on the Hubbard Potential U ($I - A$) and its relation to the bandwidth W , it seemed plausible that by going from the bis(benzene) chromium material with 2- n electrons in the a_{1g} conduction band to the vanadium analogue with one less electron in this level, we might observe a change in conductivity through the channels due to a perturbation of the balance between U and W .⁶⁹ Further, since bis(benzene) vanadium is more easily oxidized than the Cr analogue, we expected a greater maximum dopant-to-niobium ratio in this vanadium-based composite, possibly leading to further increases in conductivity.

3.1. Experimental Section

3.1.1. Materials and Equipment

All chemicals unless otherwise stated were obtained from Aldrich. All other materials and equipment unless otherwise stated were the same as those shown in Chapter 2. Bis(benzene) vanadium and the tetrachloroaluminate salt of the bis(benzene) vanadium cation were both prepared according to the literature.¹¹⁴ The solid state NMR spectra were recorded on 270 MHz MAS-NMR spectrometer at a spinning speed of 4.8 kHz without cross polarization. The Raman spectra were recorded on a Renishaw Ramascope using a Renishaw 780 nm Diode Laser System. All elemental analysis data (conducted under an inert atmosphere) were obtained from Galbraith Laboratories, 2323 Sycamore Drive, Knoxville, TN 37921-1700.

3.1.2. Synthesis

Synthesis of bis(benzene) vanadium reduced mesoporous niobium oxide composites: To a suspension of the Nb-TMS1 in dry benzene was added excess bis(benzene) vanadium calculated on the basis of metal percent as determined from elemental analysis. The mesoporous solid immediately went from a light faun color to a deep black. After several days and additional stirring to ensure complete absorption of the organometallic, the reduced material was collected by suction filtration and washed several times with benzene until the filtrate was clear. Once synthesized, the material was dried *in vacuo* at 10^{-3} torr until all condensable volatile had been removed. All other reduced oxides in this study were prepared in an analogous fashion. The elemental analysis gave values of 56.60% Nb and 5.39% C for the trimethylsilated mesoporous niobium oxide, and 43.97% Nb, 9.13% C and 7.64% V for the material after treatment with excess bis(benzene) vanadium.

3.2. Results

3.2.1. XRD Pattern, Nitrogen Adsorption Study and Elemental Analysis

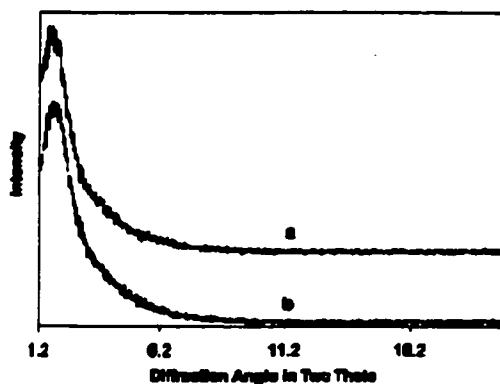


Figure 21. X-ray powder diffraction (XRD) pattern of mesoporous niobium oxide (a) before and (b) after treatment with excess bis(benzene) vanadium.

When a sample of trimethylsilated Nb-TMS1 with an X-ray powder diffraction (XRD) peak centered at $d = 45 \text{ \AA}$, an HK pore size of 28 \AA , a BET surface area of $580 \text{ m}^2\text{g}^{-1}$, and a pore volume of $0.500 \text{ cm}^3\text{g}^{-1}$ was treated with excess bis(benzene) vanadium⁴ in benzene over several days a new black material was formed and collected by suction filtration and dried *in vacuo* for 6 h to ensure complete removal of free solvent from the structure. Figure 21 shows the XRD peaks of the materials before and after treatment with bis(benzene) vanadium. The symmetric peak centered at 45 \AA in the product demonstrates that this material fully retained its mesostructure on intercalation of the organometallic. Figure 22a shows the nitrogen adsorption and desorption isotherms of the materials from Figure 21b. The BET surface area of the treated sample dropped to $467 \text{ m}^2\text{g}^{-1}$ while the pore size and pore volume decreased to 25 \AA and $0.363 \text{ cm}^3\text{g}^{-1}$ respectively. Figure 22b shows the plots of incremental pore volume versus average pore diameter as calculated from the adsorption string of the isotherm. The retention of the XRD pattern and the same type of nitrogen adsorption/desorption isotherms with a

decrease in pore size, pore volume and surface area as compared to the starting materials are all consistent with occlusion of the pores of the mesostructure by the encapsulated organometallic. The decrease in pore size by even 3 Å and the same XRD d-spacing after reduction suggests that the pore wall in the product is 3 Å thicker than that of the starting material.

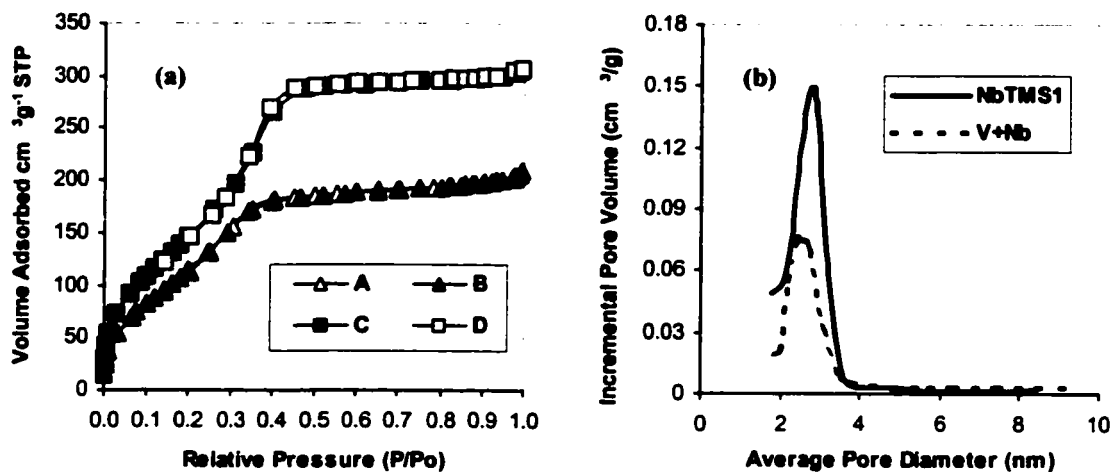


Figure 22. (a) Nitrogen adsorption (B, C) and desorption (A, D) isotherms of mesoporous niobium oxide before (C, D) and after (A, B) treatment with excess bis(benzene) vanadium. (b) Incremental HK pore volume vs. pore diameter before (solid line) and after (dotted line) treatment with excess bis(benzene) vanadium.

The elemental analysis of this new material showed an increase in carbon from 5.39 % in the starting material to 9.13 % with 7.64 % V as determined by inductively coupled plasma. The formula of this material can be calculated from this data as $\text{Nb}_{1.0}\text{O}_{4.8}\text{V}_{0.3}\text{C}_{1.6}\text{H}_{3.3}\text{Si}_{0.1}$ and was reproducible under the same preparation conditions within an acceptable range of error. The increase in carbon is consistent with partial retention of the structure of the bis(benzene) complex with some degradation to a surface vanadium species and free benzene. The V:Nb ratio in this material is 0.3:1, greater than

the Cr:Nb ratio for the related bis(benzene) chromium intercalates (0.07:1) synthesized under identical conditions, presumably due to the greater capacity of the vanadium arene complex to act as an electron donor to the niobium oxide mesostructure.

3.2.2. Ultraviolet-Visible (UV-vis) Reflectance Measurements

The UV-visible spectrum of this material shows a complex series of absorbancies. The peak at 240 nm has been observed previously and can readily be assigned to the Nb-O sp VB-CB transition.⁴² The strong absorbances at 444 nm and 324 nm are due to free bis(benzene) vanadium,¹¹⁵ while those at 479 nm and 340 nm are due to the corresponding cation on the basis of comparison to the UV spectrum of the tetrachloroaluminate salt. The absorbance at ca. 580 nm, corresponding to a band gap of 2.1 eV, appears in all reduced Nb-TMS1 species we have encountered to date and can be attributed to the transition from the dopant impurity band to the conduction band in the reduced mesoporous niobium oxide framework.⁴² In this case the impurity band can best be described as V3d-Nb4d in character. These data confirm that bis(benzene) vanadium has been absorbed into the pore structure of the material and indicate that a portion of this species was oxidized by the niobium oxide framework as seen previously for the cobaltocene and bis(benzene) chromium intercalates.

3.2.3. Electron Paramagnetic Resonance (EPR) Spectrum

The electron paramagnetic resonance spectrum of this material is shown in Figure 23. This spectrum shows two organometallic species of vanadium have been obtained. The eight lines that have axial symmetry of both g and ^{51}V hyperfine tensor with the following spin Hamiltonian parameters confirms the presence of bis(benzene) vanadium ($g_{xx} = g_{yy} = g_{\perp} = 1.982$, $g_{zz} = g_{\parallel} = 2.002$, $A_{xx} = A_{yy} = 92.30\text{G}$, $A_{zz} = 15.00\text{G}$). The

extra peak ($g = 1.992$) between $m_l = \pm 1/2$ is due to unstructured resonance associated with spin exchange in bis(benzene) vanadium,¹¹⁵ providing further evidence that this species has aggregated in the pores. In addition to this resonance, there is a broad peak from 1000-2900 G providing evidence for the bis(benzene) vanadium cation, which displays a similar resonance in this region. This peak indicates very strong electron spin-spin interactions in the system. The resonance at 3369 G normally associated with the free electron in the walls of the reduced mesostructure is not discernable, possibly because it is obscured by the resonance due to the neutral bis(benzene) vanadium. The EPR data is thus consistent with the mixed oxidation state formation of this material where low-dimensional molecular phase of bis(benzene) vanadium and its corresponding cation reside in the pores of a partially reduced niobium oxide framework.

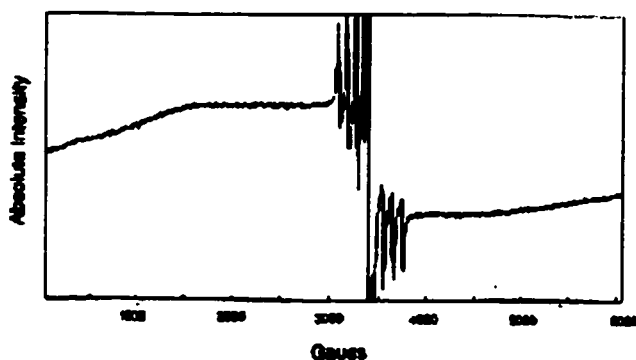


Figure 23. Powder EPR spectrum of mesoporous niobium oxide treated with excess bis(benzene) vanadium.

3.2.4. Solid State NMR Spectrum and Raman Spectroscopy

The ¹H-MAS NMR spectrum of this material exhibits a broad peak at 7.0ppm which can be assigned to the protons associated with neutral bis(benzene) vanadium in the sample. This resonance is comparable to that at 6.8ppm obtained from the ¹H-MAS NMR spectrum of pure bis(benzene) vanadium. The small chemical shift to the lower

magnetic field is possibly due to the magnetic shielding of the reduced paramagnetic mesoporous framework. There is a second resonance at 13.4ppm in the sample which can be assigned to the arene protons bis(benzene) vanadium cation according to the ^1H -MAS NMR spectrum of the tetrachloroaluminate salt. A peak due to the trimethylsilyl protons at 0.1ppm was also observed in the material and compares closely in shift to the same resonance in unreduced mesoporous niobium oxide. ^{51}V -MAS NMR measurements were also attempted, however no peaks were observed. This is not surprising, as ^{51}V -NMR signals are usually too broad to observe in paramagnetic samples. Raman spectroscopic measurements were also conducted on these materials to further probe into the nature of the occluded species in the pores. The strong resonance band at 265.9 cm^{-1} due to the symmetric bz-V-bz stretching mode in the pure bis(benzene) vanadium was too weak to be resolved in the reduced samples. This can be explained by either low loading levels or quantum confinement effects within the reduced niobium oxide framework leading to inactivity of this mode. The lack of this bz-V-bz stretching mode of bis(benzene) chromium was also noted in the Raman spectra of bis(benzene) chromium mesoporous niobium oxide composites.

3.2.5. X-ray Photoelectron Spectroscopy (XPS)

To further probe into the electronic structure of this material, X-ray photoelectron spectroscopy (XPS) studies were conducted. This surface technique provides a useful picture of the material composition since the extremely high surface areas, large pores, and thin walls (ca. 3-5 monolayers) possessed by the material ensure that the vast majority of sites are located on or just below the inner surface of the pore channels in the

material. Also, due to the facile diffusion properties afforded by the mesopores it is unlikely that reduction only occurs on the outside of the mesoporous particles. Figure 24a

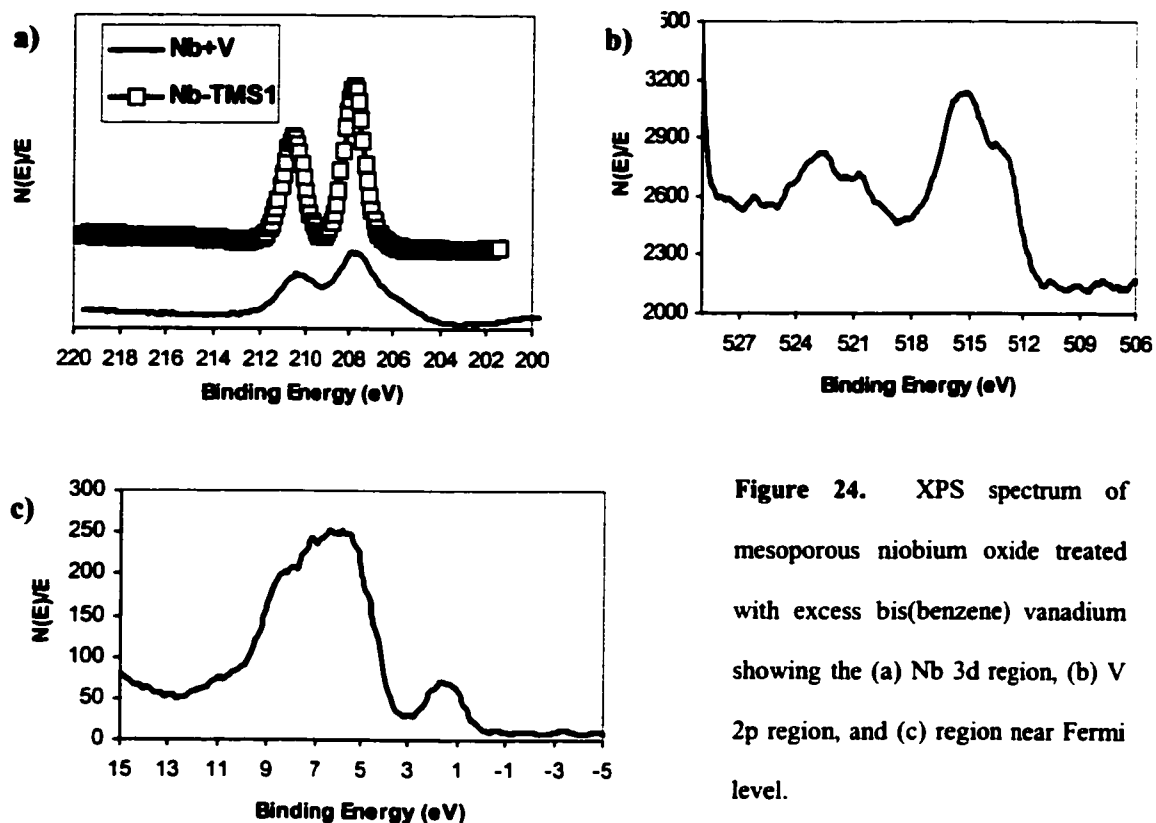


Figure 24. XPS spectrum of mesoporous niobium oxide treated with excess bis(benzene) vanadium showing the (a) Nb 3d region, (b) V 2p region, and (c) region near Fermi level.

shows the Nb 3d region of the starting material and the reduced material with the 5/2 and 3/2 peaks in clear evidence. The position of the 5/2 peak in the reduced species at 206.0 eV is consistent with partial reduction of the Nb oxide framework. In previous work it has been shown that reduction of the niobium oxide framework led to a decrease in peak position with dopant loading level.⁴² These peaks are also much broader than those in the starting material, as is the O 1s peak, providing further evidence for reduction of the Nb framework by bis(benzene) vanadium. Simulation of the 5/2 and 3/2 peaks in the spectrum of the reduced material reveals new peaks for reduced niobium species at 206.0

and 208.9 eV respectively. Figure 24b shows the V 2p 3/2,1/2 region of showing a series of emissions which can be simulated from the XPS spectra of the pure compounds to fit a mixture of neutral bis(benzene) vanadium (520.5 eV, 513.3 eV), the corresponding cation (522.1 eV, 514.5 eV), as well as a V(II) species (523.2 eV, 515.6 eV). The presence of V(II) in this system¹¹⁶ is not unexpected in light of the lower-than-expected carbon values in the elemental analysis well-documented tendency of the bis(benzene) vanadium cation to disproportionate into the neutral species and a V(II) species, in this case an oxide.¹¹⁷ Figure 24c shows the region near the Fermi level with a rough distance to the Fermi level of 3.3 eV for the metal-oxygen sp valence emission, comparable to that observed in related materials, and a small peak near the Fermi level that can be assigned to the V3d emission.¹¹⁷

3.2.6. SQUID Measurements

Figure 25 (a) shows the superconducting quantum interference device (SQUID) magnetometer plot of magnetic susceptibility versus temperature for the composite. The hysteresis in this curve can be attributed to the broad distribution of particle sizes in the mesoporous oxide, which gives a wide range of roughly spherical particles from 50-1000 nm.¹⁰⁶ The slight transition in the ZFC branch of the plot indicates some degree of superparamagnetic or spin glass behavior, although this contribution is clearly much weaker than that observed for related superparamagnetic cobaltocene intercalates.⁷¹ In another report from our group, an interesting dopant-dependent paramagnetic-to-superparamagnetic-to-spin glass transition was observed for nickelocene composites of mesoporous Nb oxide.⁷⁸ Figure 25(b) shows the variation of inverse molar magnetic susceptibility with temperature over the temperature range from 6-100K, demonstrating

that this material obeys the Curie-Weiss law where $\chi_m = C/(T-\theta)$. From this plot, the Curie constant C can be calculated as $3.41 \text{ emu mol}^{-1} \text{ K}$ and the Weiss constant θ is -22.39 K , indicating that there are subtle antiferromagnetic interactions in the material which tends to support spin glass rather than superparamagnetic behavior in this system.

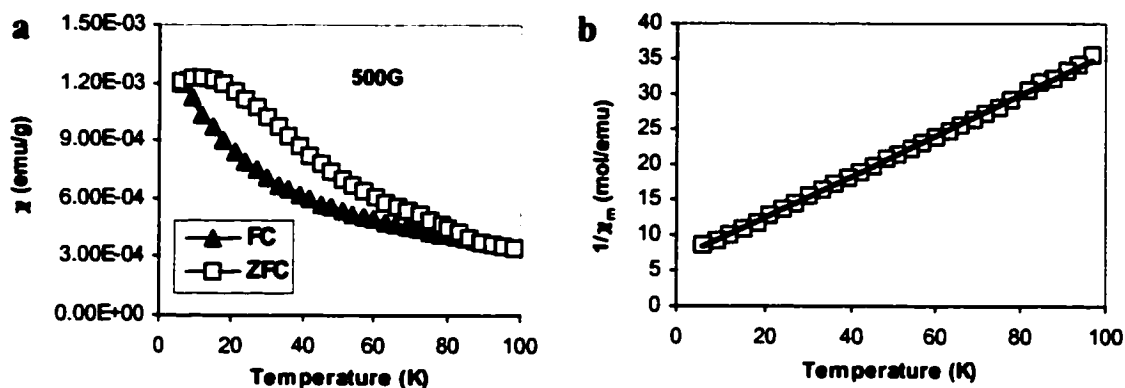


Figure 25. (a) SQUID magnetometer plot of magnetic susceptibility versus temperature for a sample of mesoporous niobium oxide treated with excess bis(benzene) vanadium showing the field cooled (FC) and zero-field cooled (ZFC) branches of the plot. (b) Plot of the variation of inverse molar magnetic susceptibility with temperature at a magnetic field of 500G for sample in (a).

The effective magnetic moment μ_{eff} can be calculated as 1.65 from the equation $C = N\mu_B^2\mu_{\text{eff}}^2/3k$. The B vs. H plots at 5K and 100K of this V composite show a linear progression, typical only of paramagnetic species, indicating that paramagnetism dominates the behavior of this system.

3.3. Discussion

Electron transport properties in these bis(benzene) vanadium intercalates was measured by the four point method and revealed reproducible values in the range from

$1.0\text{-}5.0 \times 10^{-4} \text{ ohm}^{-1}\text{cm}^{-1}$, almost fifty times greater than that observed in the related Cr species. Since the reduced framework of Nb-TMS1 has been previously shown to be insulating,⁴² these materials are convenient hosts for the study of conductivity in one-dimensional molecular phases within the pores, as all conductivity must therefore arise from interactions between the encapsulated species and not the walls of the structure. Unpublished results from our group showed that unreduced and Li-reduced mesoporous niobium oxides are ion insulators, thus ruling out any contribution to conductivity from proton or ion transport. It is also unlikely that surface protons would be present, since acid is readily reduced to H₂ by bis(benzene) vanadium. In order to gauge the contribution made by the low-dimensional molecular phase in the pores of the material as opposed to that deposited on the external surface of the material, amorphous niobium oxide treated with trimethylsilyl chloride with a BET surface area of $91 \text{ m}^2\text{g}^{-1}$ was treated with bis(benzene) vanadium under the same conditions to yield dark gray composites with conductivities of less than $10^{-7} \text{ ohm}^{-1} \text{ cm}^{-1}$. XPS studies of this material showed the expected slight reduction of the Nb oxide. These data suggest that the dopant phase deposited on the outer surface does not contribute to the overall conductivity of the mesoporous composites to any significant extent. This is not entirely surprising since the ratio of outer surface area to inner surface area due to the pores is less than 1:250 on the basis of the nitrogen adsorption data. The role of V(II) in this system, present as an oxide dopant in or on the surface of the walls of the mesostructure, in the conductivity is not completely understood. However, vanadium oxide doped (1-15 mol.% V) Nb-TMS1 have been studied in our group and have only shown insulating properties (less than $10^{-8} \text{ ohm}^{-1} \text{ cm}^{-1}$).¹¹⁸ These materials were reduced with alkali metals to form low-valent V

species in the walls, however this led only to insulating behavior. The as-synthesized bis(benzene) vanadium composites were also oxidized in air at 100 °C for 24 h to ensure complete degradation of the organometallic, and then reduced with K-naphthalene. These materials were also insulating. All of these experiments suggest that conductivity in this V system arise only from the presence of a mixed oxidation state organometallic phase in the pores of the material. Since the kinetic diameter of bis(arene) complexes is ca. 10 Å and the pore diameter of the mesoporous niobium oxide is 28 Å, it is reasonable to conclude that the pores can accommodate one or two organometallic units across the pore diameter.

Understanding the mechanism of conductivity in these materials is complicated by the fact that the ground state configuration of bis(benzene) vanadium cation is $e_{2g}^3 a_{1g}^1$, suggesting that the conduction band in the vanadium composite has mixed a_{1g}/e_{2g} character.¹¹⁹ In molecular metals such as TCNQ salts, a change in metallic to insulating behavior is observed in going from TCNQ/TTF with 0.59 electrons in the π^* conduction band to TCNQ/K with 1 electron in the conduction band.¹²⁰ In related mesoporous niobium oxide-alkali fulleride materials it was shown that the decreased T_{1u} band filling in one-dimensional alkali fulleride phases within the mesopores of Nb-TMS1 altered the physical behavior of the composite from insulating at $n = 3$ to metallic at $n = 0.6$.⁸¹ The reasons for the increase in conductivity in these bis(benzene) vanadium materials with respect to the Cr analogues are not clear, but according to our model may be related to the decreased number of electrons in the a_g conduction band of this species due to a change from Cr $d^6 (a_g^{2-n})$ to V d^5 where $n =$ the number of electrons transferred from the organometallic phase to the walls of the structure. Other factors that may also be at play

are the difference in potential of the V(0)/V(I) and Cr(0)/Cr(I) redox couples as well as the more facile oxidation of the vanadium species leading to a higher loading level within the mesopores which would in turn lead to a more continuous spacing of the individual molecules within the structure. This greater homogeneity in the structure could also lead to improved conductivity within the channels.

Metallic conductivity in solids depends on Hubbard potential ($U = I - A$), where I is the ionization potential and A is the electron affinity of the charge carrying species, and the bandwidth (W). If W is greater than U , the material will be conducting. If it is not then the material will be insulating. Since W is difficult to calculate in an amorphous system it is also meaningful to use pure metal bandwidth (W) in this system. The Hubbard potential can be estimated by considering the I values of 5.72eV ¹²¹ and 5.40eV ¹²² for bis(benzene) vanadium and bis(benzene) chromium respectively along with A values for the corresponding cationic species. Although the A values for their cations are not available in the literature, they can be estimated from the A values of bis(benzene) vanadium(0) and bis(benzene) chromium(0), and bis(cyclopentadienyl) vanadium(II) and bis(cyclopentadienyl) chromium(II). The A values for bis(benzene) vanadium and bis(cyclopentadienyl) vanadium are -0.29eV ¹²³ and 0.68eV ¹²⁴ respectively. We can use half the difference $[(0.68\text{eV} + 0.29\text{eV})/2 - 0.29\text{eV} = 0.195\text{eV}]$ between them as the A value for bis(benzene) vanadium(I) cation. The A values for bis(benzene) chromium and bis(cyclopentadienyl) chromium are -0.76eV ¹²⁵ and 0.88eV ¹²⁴ respectively, and the same calculation as described above for half the difference gives 0.06eV as the A value for the bis(benzene) chromium(I) cation. Therefore, the Hubbard potential U for vanadium system will be 5.525eV ($=5.72\text{eV}-0.195\text{eV}$) and for chromium system will be

5.34eV (=5.40eV–0.06eV). From this analysis and comparison to the estimated maximum value for the bandwidth W of 6.77eV for vanadium and 6.56eV for chromium, it would appear that conductivity in both systems should be favorable according to this model.

In order to more fully explore the effect of electronic configuration on conductivity in these materials we treated Nb-TMS1 with bis-1,3,5-tri-*tert*-butylbenzene yttrium¹²⁶ under the assumption that the d^3 species may give different behavior due to the smaller number of valence electrons per mole of dopant. Comparison of this new material to the V analogue is not simple, however, since this bis-arene species does not have electrons in the a_g level, but only in the lower doubly degenerate e_g level. The material was prepared by stirring trimethylsilated Nb-TMS1 in benzene with the Y precursor. The black color of the reduced material indicated that reduction of the niobium framework occurred as expected by the strongly reducing character of this species. The XRD showed a peak at $d = 45 \text{ \AA}$ and the nitrogen adsorption data showed a drop in surface area to $423 \text{ m}^2\text{g}^{-1}$, consistent with retention of the mesostructure and partial filling of the pores of the niobium oxide framework. Elemental analysis showed that the carbon value did not increase significantly with respect to the starting material while 2.65 % Y had been absorbed. This is consistent with the organometallic acting as a source of Y in much the same way that Na-naphthalene acted as a source of Na in previously studied reduced mesoporous niobium oxide materials. Like this Na-reduced material, the Y-doped composite was insulating, suggesting that this material be also subject to Anderson localization effects. Thus, the Y composite is best described as a direct analogue of the Na-reduced materials with an Y center replacing three Na centers in or on the wall of the

reduced mesostructure, and thus cannot be directly compared to the V and Cr materials, which have low-dimensional organometallic phases occluding the pores.

3.4. Conclusion

In conclusion we have synthesized and characterized a new bis(benzene) vanadium intercalate of Nb-TMS1 in which the mixed oxidation state of the vanadium phase is most likely responsible for the electronic conduction within the mesopores of the material. This conductivity appears to arise from the formation of a molecular phase in the pores of the material and the introduction of charge-carrying holes in the e_{2g} band of this phase, however a small contribution from the surface conductivity of V(II) species may also be important. The higher conductivity of these materials as compared to related bis(benzene) chromium intercalates could be attributed to a decrease in the number of electrons in the conduction band and formation of the mixed oxidation state molecular phase as well as the higher percentage of the vanadium species in the pores as compared to the Cr material.

Chapter 4. Cp₂Cr and Cp₂V Composites of Mesoporous Niobium Oxide with Pseudo One-Dimensional Organometallic Wires in the Pores

In the preceding two chapters, it was shown that mesoporous niobium oxide composites synthesized with bis(benzene) chromium¹⁰⁶ and bis(benzene) vanadium¹⁰⁷ are paramagnetic and semi-conducting with conductivity values as high as 10⁻⁴ ohm⁻¹cm⁻¹. This chapter will compare the electronic behavior of new bis(cyclopentadienyl) vanadium and chromium composites to previously studied bis(benzene) vanadium and bis(benzene) chromium composites to gauge the effect of changing from a zero-valent bis(arene) metal dopant to the corresponding divalent metallocene analogue. Since conductivity in solids depends on a balance between U, the Hubbard potential, (the difference between the ionization potential and the electron affinity of the charge carrying species in question) and the band width W, where electron mobility is favored when W > U,⁶⁹ the electronic properties of these mesoporous composites should depend strongly on the electronic configuration and oxidation state of the organometallic dopants, as well as loading level and the interatomic spacing between the charge carrier units, potentially influenced by the steric bulk of the supporting ligand system. While other factors such as surface conductivity and grain boundary effects may be at play, the dependence on electronic factors is readily illustrated by the dramatic difference in conductivity between insulating mixed oxidation state cobaltocene composites⁷¹ with a π^{*1}/π^{*0} configuration for Co(II) and Co(III), respectively, and the semiconducting bis(benzene) chromium composites with a configuration of $e_{2g}^4 a_{1g}^2/e_{2g}^4 a_{1g}^1$ for Cr(0) and Cr(I), respectively.¹²⁷ In this case

the much lower loading level of Cr (0.05-0.07 Cr:Nb ratio) in the niobium oxide mesostructure as compared to that of Co (0.3-0.5 Co:Nb ratio) in the analogous material would be expected to lead to lower conductivity in the Cr material, yet is obviously offset by the differences in relative electronic properties in the occluded species. It is thus anticipated that the changes in electron configuration, ionization potential, and electron affinity in this series of isostructural chromocene and vanadocene dopants will lead to composites with different electronic properties and that this change in electronic behavior may provide further insight into the nature of electron mobility in this new family of materials.

4.1. Experimental Method

4.1.1. Materials and Equipment

All chemicals unless otherwise stated were obtained from Aldrich. All other materials and equipment unless otherwise stated were the same as those shown in Chapter 2 and Chapter 3. X-ray single crystal data were collected on a Siemens SMART System CCD diffractometer, and the data sets were solved employing the SHELX-TL software package. All X-ray photoelectron spectroscopy (XPS) peaks were reference to the Carbon C-(C, H) peak at 284.8 eV and the data were obtained using a Physical Electronics PHI-5500 XPS using charge neutralization of 2-4 eV where appropriate. All elemental analysis data including inductively coupled plasma (ICP) were obtained from Galbraith Laboratories, 2323 Sycamore Drive, Knoxville, TN 37921-1700.

4.1.2. Synthesis

Synthesis of metallocene composites of mesoporous niobium oxide: To a suspension of trimethylsilated Nb-TMS1 in dry benzene was added 1.0mol equivalent of metallocene calculated on the basis of molar percent Nb as determined by ICP. The mesoporous solid immediately went from a light faun color to a dark color. After several days stirring to ensure complete absorption of the organometallic, the reduced material was collected by suction filtration and washed several times with benzene. Once synthesized, the material was dried *in vacuo* at 10^{-3} torr on a Schlenk line until all condensable volatiles had been removed.

Synthesis of bis(cyclopentadienyl) vanadium ditriflate: 0.15g (0.0008mol) bis(cyclopentadienyl) vanadium in CH_2Cl_2 was added to a solution of 0.42g (0.0016mol) AgSO_3CF_3 in CH_2Cl_2 with stirring under nitrogen. The color of the mixture immediately changed from purple to green. Stirring was continued for 1 hour, and the solution was then filtered to remove the silver precipitate. The filtrate was evaporated to dryness and the resulting solid was fully washed with benzene to give a dark solid. The crude product was recrystallized by vapor diffusion of ether into CH_2Cl_2 to afford the pure dication in 92% yield. The single crystal structure of this vanadocene ditriflate compound is available as supplemental data. Elemental analysis calculated for $\text{C}_{12}\text{H}_{10}\text{O}_6\text{F}_6\text{S}_2\text{V}$: C, 30.07%; H, 2.10%; V, 10.63%; S, 13.38%; F, 23.78%. Found: C, 29.98%; H, 2.03%; V, 10.68%; S, 13.47%; F, 23.88%.

Synthesis of bis(cyclopentadienyl) chromium triflate: The method to synthesize chromocenium triflate was similar to that above for vanadocenium ditriflate except a 1:1 molar ratio of chromocene and AgSO_3CF_3 was used. The total yield of this brown compound was 78%. Recrystallization of this compound in CH_2Cl_2 and ether gave

brown needle-like crystals which were characterized by XPS, EPR, and UV. Elemental analysis calculated for $C_{11}H_{10}O_3F_3SCr$: C, 39.89%; H, 3.04%; Cr, 15.70%; S, 9.68%; F, 17.21%. Found: C, 39.70%; H, 2.83%; Cr, 15.79%; S, 9.81%; F, 17.42%.

4.2. Results

4.2.1. X-ray Powder Diffraction (XRD) Pattern, Nitrogen Adsorption Study and Elemental Analysis

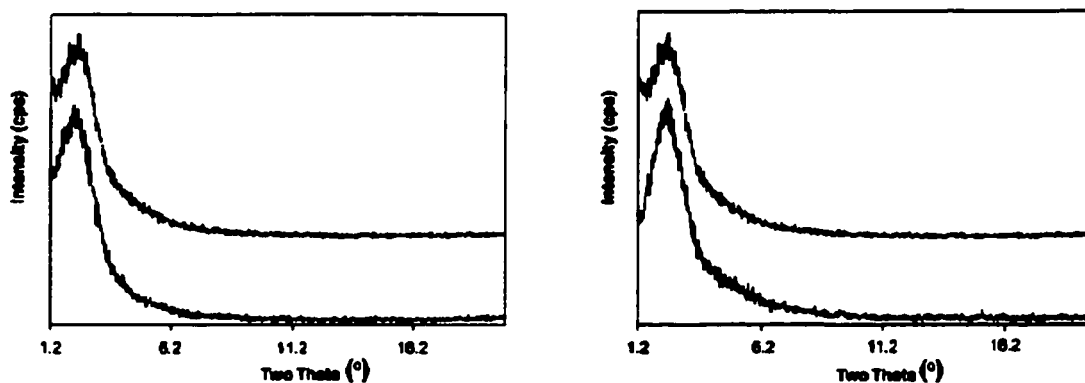


Figure 26. (a, left) XRD of mesoporous niobium oxide before (upper) and after (lower) treatment with excess bis(cyclopentadienyl) vanadium. (b, right) XRD of mesoporous niobium oxide before (upper) and after (lower) treatment with excess bis(cyclopentadienyl) chromium.

Since conductivity in molecular-based metals is strongly dependant on ionization potential and electron affinity of the species in question, and hence electron configuration and oxidation state,¹²⁸ we chose to investigate the changes in physical behavior of organometallic mesoporous niobium oxide composites on going from bis(benzene) vanadium (0), with a ground state of $e_{2g}^4 a_{1g}^1$, as a dopant to bis(cyclopentadienyl) vanadium (II), with a ground state of $e_{2g}^2 a_{1g}^1$. When a sample of trimethylsilated Nb-TMS1 with an X-ray powder diffraction (XRD) peak centered at $d = 38 \text{ \AA}$, an HK pore size of 24 \AA , a BET surface area of $712 \text{ m}^2\text{g}^{-1}$, and a pore volume of $0.470 \text{ cm}^3\text{g}^{-1}$ is

treated with excess bis(cyclopentadienyl) vanadium in benzene over two days a dark-colored material is formed which is collected by suction filtration and dried *in vacuo* for 6 h to ensure complete removal of free solvent from the structure. Figure 26a shows the XRD peak of the material after treatment with bis(cyclopentadienyl) vanadium. The peak centered at 38 Å demonstrates that the material has fully retained its mesostructure on intercalation of the organometallic.

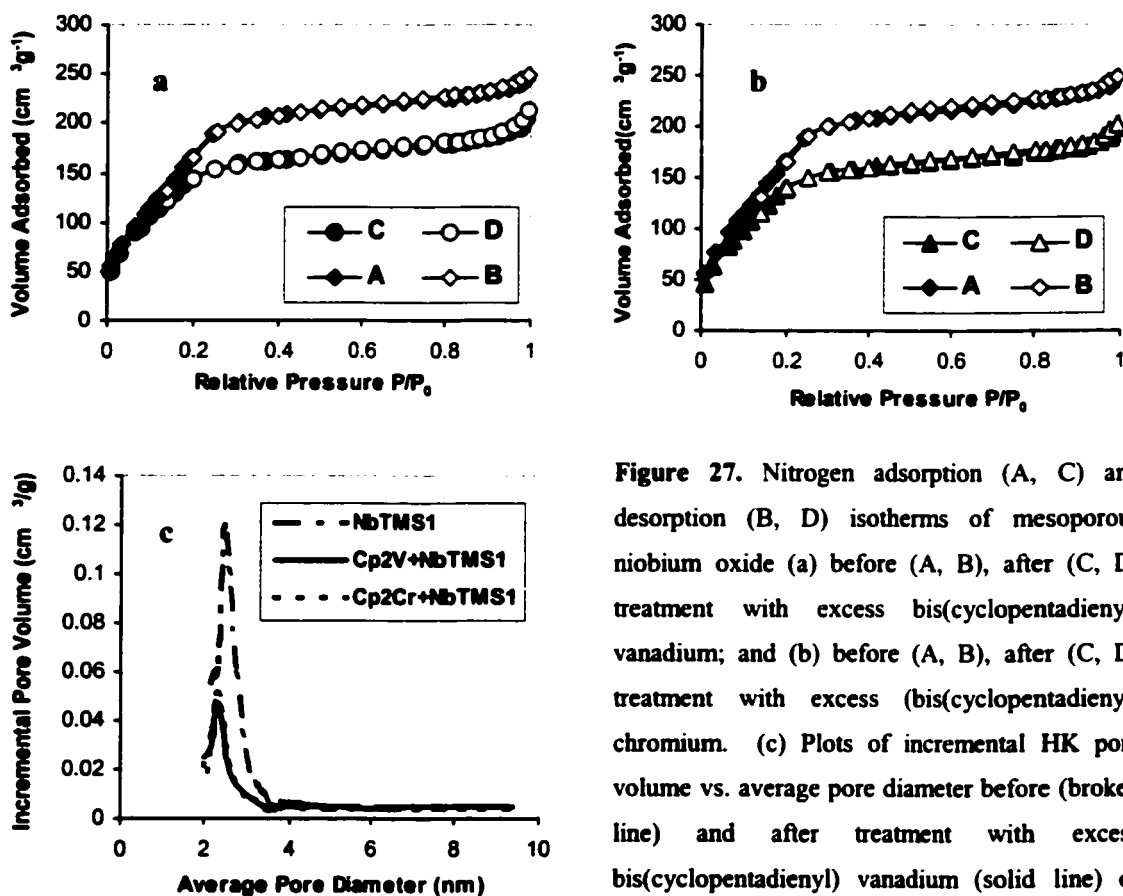


Figure 27. Nitrogen adsorption (A, C) and desorption (B, D) isotherms of mesoporous niobium oxide (a) before (A, B), after (C, D) treatment with excess bis(cyclopentadienyl) vanadium; and (b) before (A, B), after (C, D) treatment with excess bis(cyclopentadienyl) chromium. (c) Plots of incremental HK pore volume vs. average pore diameter before (broken line) and after treatment with excess bis(cyclopentadienyl) vanadium (solid line) or bis(cyclopentadienyl) chromium (dotted line).

Figure 27a shows the nitrogen adsorption and desorption isotherms of the materials from Figure 26a. The BET surface area of the treated sample dropped to 595 m²g⁻¹ while the pore size and the pore volume decreased to 23 Å and 0.282 cm³g⁻¹, respectively.

Figure 27c shows a plot of HK pore size versus incremental pore diameter before and after treatment. These data are consistent with partial occlusion of the pores of the mesostructure by the encapsulated organometallic. The elemental analysis of this new composite showed an increase in carbon from 4.65 % in the starting material to values ranging from 9.07-9.87% depending on the sample. The increase in carbon is fully consistent with retention of the structure of the bis(cyclopentadienyl) complex without loss of the cyclopentadienyl rings. The V:Nb ratio in this material ranges from 0.10-0.15:1 as determined by ICP. This compares to other ratios in bis(benzene) vanadium-reduced composites of 0.3:1, and is consistent with the lower degree of reducing ability in the more highly oxidized organometallic.

4.2.2. UV-Visible Reflectance Measurements of Bis(cyclopentadienyl) Vanadium

Composites of Mesoporous Niobium Oxide

The UV visible spectrum of this material shows a complex series of absorbancies. The peak at 240 nm has been observed previously and can readily be assigned to the Nb-Osp VB-CB transition.⁴³ The strong absorbances at 214 nm and 298 nm are due to neutral bis(cyclopentadienyl) vanadium,¹²⁹ while that at 350 nm are due to a typical charge transfer transition (LMCT) from the Cp ring to the V(IV) center in the bis(cyclopentadienyl) vanadium dication.¹²⁹ The absorbance at ca. 580 nm appears in all reduced Nb-TMS1 species we have encountered to date and can be attributed to the Nb4d-Osp conduction band transition. These data confirm that bis(cyclopentadienyl) vanadium has been absorbed into the pore structure of the material and indicate that a portion of this species was oxidized by the niobium oxide framework as reported previously for the cobaltocene and bis(benzene) chromium intercalates.¹⁰⁶ While

oxidation of bis(benzene) vanadium leads to formation of a monocation, the bis(cyclopentadienyl) vanadium cation is even more unstable to loss of an electron than neutral vanadocene species and thus loses a second electron to the mesostructure.¹³⁰

4.2.3. Electron Paramagnetic Resonance (EPR) Spectra of Bis(cyclopentadienyl) Vanadium Composites of Mesoporous Niobium Oxide

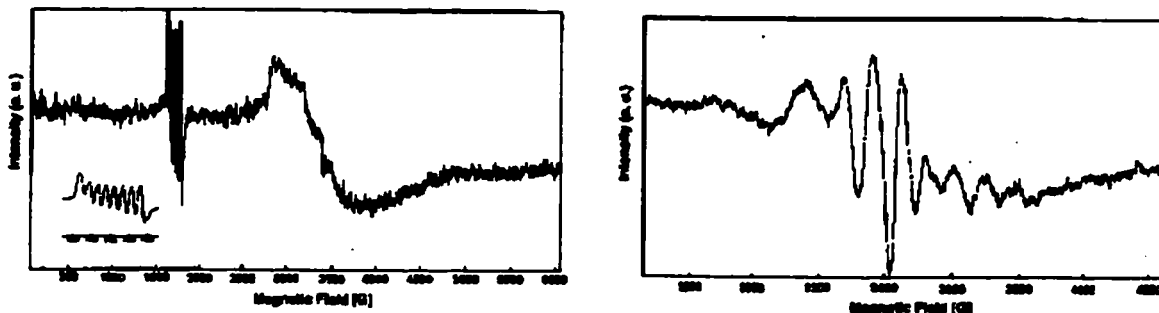


Figure 28. Powder EPR spectra of mesoporous niobium oxide treated with excess bis(cyclopentadienyl) vanadium (a, left) in THF at 77K; and (b, right) at room temperature with a V:Nb ratio of 0.005. The expansion is shown below to magnify the hyperfine splittings.

The electron paramagnetic resonance (EPR) spectra of this material are shown in Figure 28a and b. The powder sample was measured in THF at 77K (Figure 28a). This spectrum shows two very well resolved sets of eight lines due to the ^{51}V nucleus ($I = 7/2$). The first set of eight lines at 3000 G affords $g_{\parallel} = 2.26$ and an average hyperfine splitting of $A = 47.3$ G, originating from the resonance of the main rotation axis (z -axis) of the neutral bis(cyclopentadienyl) vanadium molecule oriented along the magnetic field. The second set of stronger eight lines at almost half field (1700 G) gives $g_{\perp} = 4.00$ and an average hyperfine splitting of $A = 23.4$ G due to the bis(cyclopentadienyl) vanadium rotation axis being perpendicular to magnetic field.¹³¹ The broad peak at 3386.9 G ($g = 2.00$) can be assigned to the free electron in the reduced mesostructure and

appears in the EPR spectra of all reduced mesoporous niobium oxide materials we have studied to date.⁸¹ Figure 28b shows the room temperature powder spectrum of this material at the ratio of 0.005 equivalents of V:Nb. The lower level of V was required to prevent spin-spin interactions between the organometallics at the higher ratio in order to observe hyperfine splittings. The very well resolved eight lines are also due to the ⁵¹V nucleus ($I = 7/2$). The asymmetry of this spectrum suggests both the g factor (average $g = 2.02$) and the hyperfine interactions (an average hyperfine splitting of $A = 90.3$ G) are anisotropic. The larger hyperfine splitting of the bis(cyclopentadienyl) vanadium dication in this material as compared to that in the solvent ($A = 75$ G) is due to Jahn-Teller distortion to the ²E_{2g} state in the reduced mesopores.¹³² These data confirm the presence of the bis(cyclopentadienyl) vanadium dication in the sample, and are consistent with the mixed oxidation state formulation of this material where one-dimensional wires or agglomerates of bis(cyclopentadienyl) vanadium and its corresponding dication reside in the pores of a partially reduced niobium oxide framework.

4.2.4. X-ray Photoelectron Spectroscopy (XPS) Studies of Bis(cyclopentadienyl)

Vanadium Composites of Mesoporous Niobium Oxide

In order to further investigate the composition and electronic structure of this new material X-ray photoelectron spectroscopy (XPS) studies were conducted. Figure 29a shows the Nb 3d region with the 5/2 and 3/2 peaks in clear evidence. The positions of the 3/2, 5/2 peaks at 210.1, 207.3 eV, respectively is consistent with reduction of the Nb by roughly one tenth of an oxidation state as compared to previous work.⁴³ These emissions are also broader than those in the starting material, as is the O1s peak, providing further evidence for reduction of the Nb framework by bis(cyclopentadienyl)

vanadium. Figure 29b shows the V 2p 3/2,1/2 region of the spectrum and displays a series of emissions which can be simulated to fit a mixture of the neutral Cp₂V species (513.0 eV, 520.2 eV), a vanadium (IV) species at (514.9 eV, 522.4 eV), and a V(V) species (516.4 eV, 524.5 eV).¹³³ XPS simulations give a ratio between these three species of 1:14:6. The much smaller peak of neutral Cp₂V species may be due to vaporization under the high vacuum conditions of the XPS experiment.¹⁰⁸ In order to confirm the nature of the vanadium (IV) species, vanadocenium ditriflate was synthesized by treatment of vanadocene with silver triflate.

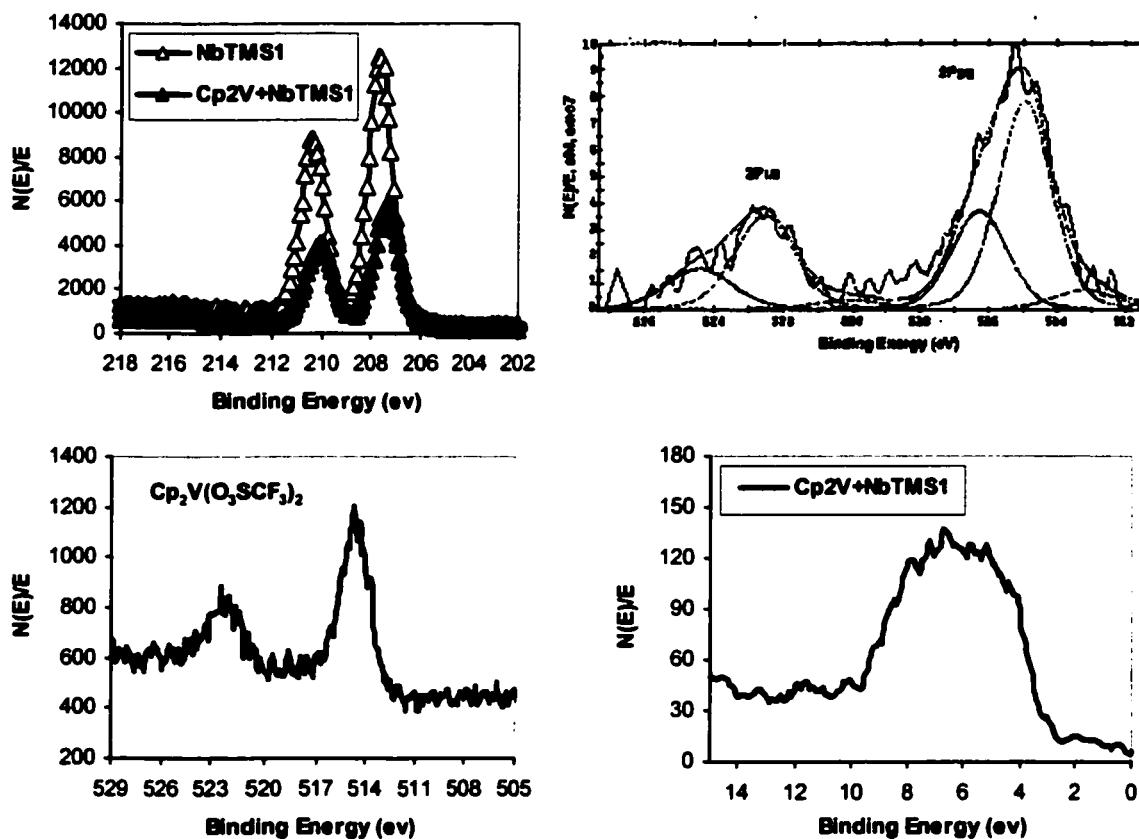


Figure 29. XPS spectra of mesoporous niobium oxide treated with excess bis(cyclopentadienyl) vanadium showing the (a, top left) Nb 3d 3/2, 5/2 region; (b, top right) V 2p 1/2, 3/2 region; (c, bottom left) V 2p 1/2, 3/2 region of vanadocenium ditriflate; and (d, bottom right) the region near Fermi level

The XPS spectrum of this previously unknown compound shows emissions in the V 2p 3/2,1/2 region at 514.8 eV, 522.3 eV (Figure 29c), completely consistent with the V(IV) emissions in the spectrum from Figure 29b. Figure 29d shows the region near the Fermi level of the XPS spectrum of the composite with a rough distance to the Fermi level of ca. 3.0 eV for the metal-oxygen sp valence emission, comparable to that observed in related materials.¹⁰⁷ The conductivity of these composites is $10^{-5} \text{ ohm}^{-1}\text{cm}^{-1}$, lower than that obtained for the bis(benzene) vanadium composites of $10^{-4} \text{ ohm}^{-1}\text{cm}^{-1}$.

4.2.5. Superconducting Quantum Interference Detector (SQUID) Measurements of Bis(cyclopentadienyl) Vanadium Composites of Mesoporous Niobium Oxide

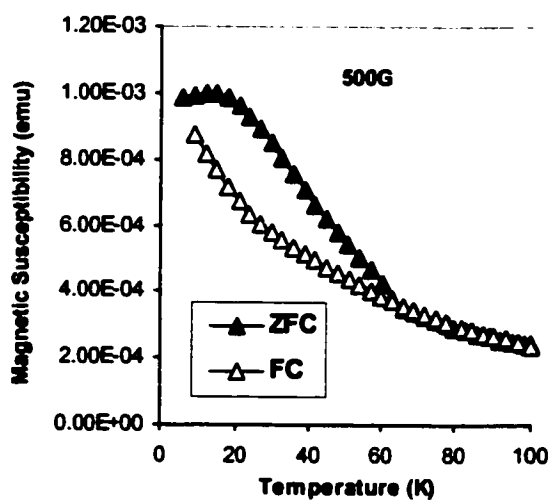


Figure 30. SQUID magnetometer plot of magnetic susceptibility per gram versus temperature (M vs. T) for a sample of mesoporous niobium oxide treated with excess bis(cyclopentadienyl) vanadium showing the field cooled (FC) and zero-field cooled (ZFC) branches of the plot.

Figure 30 shows the superconducting quantum interference device (SQUID) magnetometer plot of magnetic susceptibility versus temperature for the composite, indicating that this material is paramagnetic. This is expected from the presence of unpaired electrons in the structure. The hysteresis in this curve can be attributed to the

broad distribution of particle sizes in the mesoporous oxide, with a wide range of roughly spherical particles from 50-1000 nm as previously determined by scanning electron microscopy (SEM).⁷¹ The slight transition in the ZFC branch of the plot possibly indicates some degree of superparamagnetism or spin glass behavior at low temperature, although this contribution is clearly much weaker than observed for related nickelocene intercalates.⁷⁸ The B vs H plots at 5K and 100K of this material are linear, typical only of paramagnetic species, demonstrating that superparamagnetic or spin glass contributions do not dominate the magnetic behavior in this system.

4.2.6. Electron Paramagnetic Resonance (EPR) Spectra of Bis(cyclopentadienyl)

Chromium Composites of Mesoporous Niobium Oxide

To further probe into the effect of changing from a neutral bis(benzene) complex to its corresponding bis(cyclopentadienyl) complex, the bis(cyclopentadienyl) chromium intercalates were synthesized. Because this complex has an electronic ground state configuration of $e_{2g}^3 a_{1g}^1$, different than that of the neutral bis(benzene) Cr (0) species ($e_{2g}^4 a_{1g}^2$), different electronic properties for the corresponding mesoporous niobium oxide composites were anticipated. Thus, treatment of a sample of trimethylsilated mesoporous niobium oxide with a BET surface area of $712 \text{ m}^2\text{g}^{-1}$, an HK pore size maximum at 24 Å, and an X-ray powder diffraction (XRD) pattern with a single peak at $d = 38 \text{ Å}$ with excess bis(cyclopentadienyl) chromium (II) in benzene at ambient temperature for two days gave a new dark green to gray material which is isolated by suction filtration and washed repeatedly with benzene followed by drying in *vacuo* at 10^{-3} torr. The XRD pattern of this new material is shown in Figure 26b and displays a peak at $d = 38 \text{ Å}$, indicating that the mesostructure has been fully retained. The nitrogen adsorption-

desorption isotherms of the starting material and bis(cyclopentadienyl) chromium composite are shown in Figure 27b. The BET surface area of the composite was $589 \text{ m}^2\text{g}^{-1}$ and an HK pore size maximum at 23 Å. Figure 27c shows a plot of the HK incremental pore volume versus the average pore diameter. The pore volume of this material dropped from $0.470 \text{ cm}^3\text{g}^{-1}$ to $0.287 \text{ cm}^3\text{g}^{-1}$. All of these data confirm retention of the mesostructure with partial occlusion of the pores with one or more organometallic chromium species. Elemental analysis of this new material gave values of 9.23-9.74%C and the molar ratio of Cr:Nb in the amount of 0.10-0.13:1. The UV-visible reflectance spectrum showed a broad range of absorbances from 250 nm to 800 nm with peaks at 225 nm, 332 nm corresponding to the neutral chromium species and a peak at 280 nm which can be assigned to the cation as compared to the UV spectra of bis(cyclopentadienyl) chromium triflate and previous work conducted on the chloride salt of this cation.¹³⁴ The EPR spectra of this material are shown in Figure 31a and 31b. The powder spectrum of this material shows evidence for a three-electron system ($S = 3/2$), most likely the bis(cyclopentadienyl) chromium cation, present in these materials. The two lines in the Figure 31b are due to the anisotropy of the g factor which gives two g values, i.e. $g_{\parallel} = 1.98$, $g_{\perp} = 3.98$, according to the simulation to this spectrum. The much larger peak at g_{\perp} than that at g_{\parallel} indicates very large number of bis(cyclopentadienyl) chromium cations with axes nearly perpendicular to the magnetic field direction. Also, both of these two lines come from the transition $\langle +1/2 \rangle \leftrightarrow \langle -1/2 \rangle$. The other two transitions $\langle \pm 1/2 \rangle \leftrightarrow \langle \pm 3/2 \rangle$, which are allowed by selection rules, are not detectable because of the very large zero field interaction (D value). This case often occurs in a Cr(III) system, and can be readily fitted to an $S = 1/2$ spin Hamiltonian of the form $H = \beta_e [g_{\perp} (B_x S_x + B_y S_y) + g_{\parallel} B_z S_z]$,

but $g_{\perp} = (S+1/2) g_{\perp}'$, where g_{\perp}' is the value in the regular S spin Hamiltonian (often close to 2). Solid samples of bis(cyclopentadienyl) chromium did not show any signal at room temperature or low temperature as described previously for this complex,¹³⁵ however the spectrum of this species was obtained by observing the powder sample in THF at room temperature (Fig.31a). The two lines in this spectrum at 3517 G ($g = 1.988$) and 3488 G ($g = 2.00$) are consistent with a triplet ground state ($S = 1$) of neutral Cp_2Cr due to the transitions $\langle \pm 1 | \leftrightarrow \langle 0 |$. The half field transition $\langle +1 | \leftrightarrow \langle -1 |$ was too weak to be resolved because of unfavorable selection rules for this transition.¹³⁶

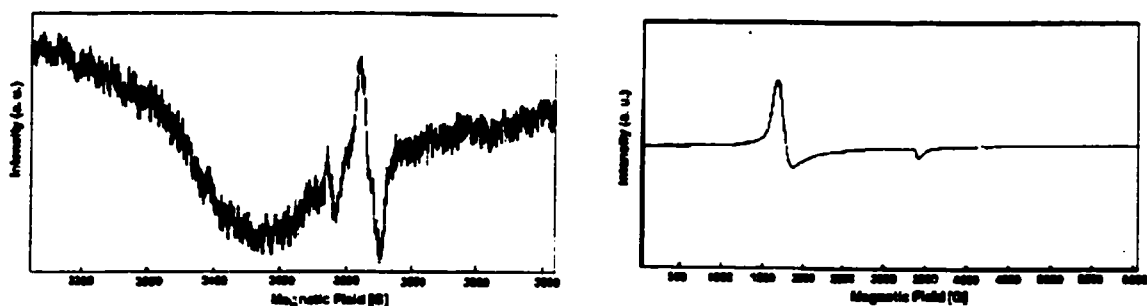


Figure 31. Powder EPR spectra of mesoporous niobium oxide treated with excess bis(cyclopentadienyl) chromium, (a, left) in THF at room temperature; and (b, right) at 77K.

4.2.7. X-ray Photoelectron Spectra of Bis(cyclopentadienyl) Chromium Composites of Mesoporous Niobium Oxide

The Cr 2p 1/2, 3/2 regions of the X-ray photoelectron (XPS) spectrum of the mesoporous composite and its simulation are shown in Figure 32a. This spectrum exhibits emissions at 584.5eV, 574.8 eV and 585.5 eV, 575.7 eV corresponding to neutral bis(cyclopentadienyl) chromium,¹³³ and a Cr (III) species, respectively. The other peaks

at 587.1 eV, 577.4 eV can be assigned to a higher oxidation state Cr (IV) species. The integrated intensity ratios of these three peaks were calculated as 1:6:6, respectively.

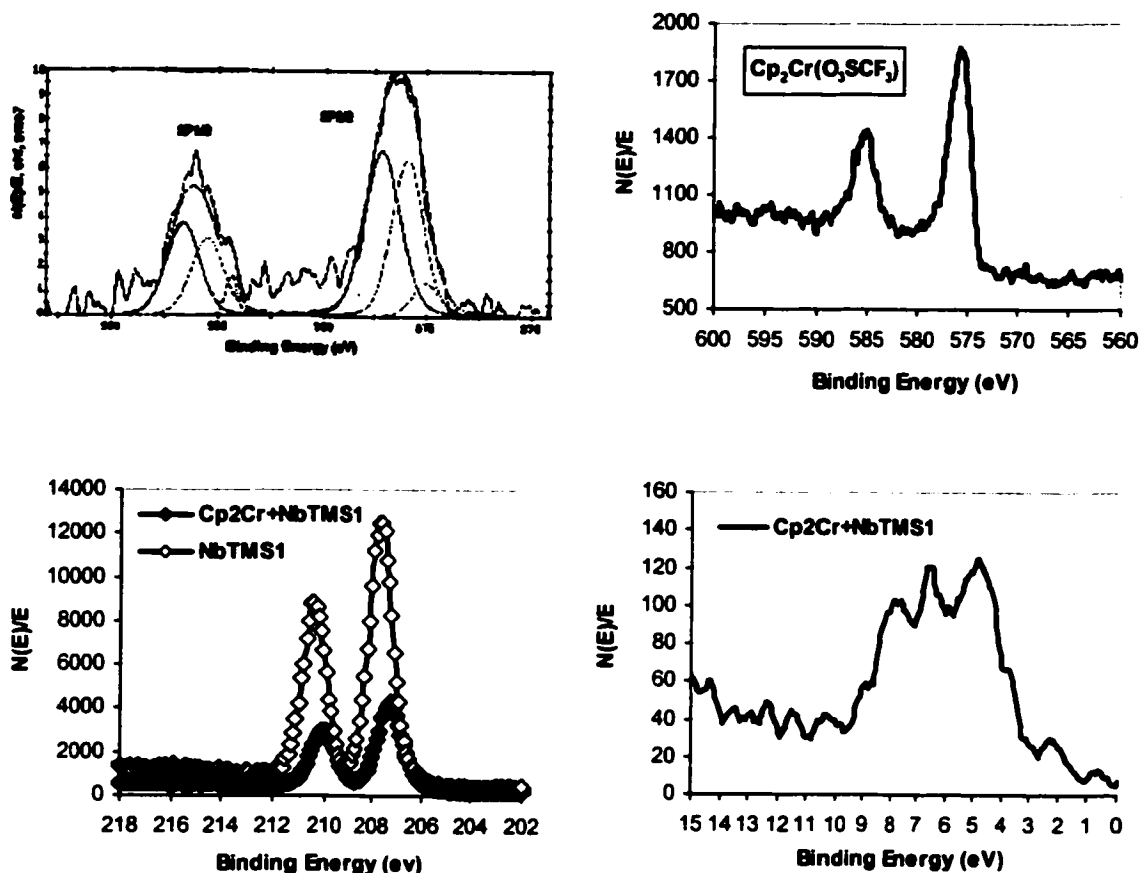


Figure 32. XPS spectra of mesoporous niobium oxide treated with excess bis(cyclopentadienyl)chromium showing the (a, top left) Cr 2p 1/2, 3/2 region; (b, top right) Cr 2p 1/2, 3/2 region of chromocenium triflate; (c, bottom left) Nb 3d 3/2, 5/2 region; and (d, bottom right) region near the Fermi level.

The lower intensities of the emissions due to neutral bis(cyclopentadienyl) chromium relative to the other species are possibly due to vaporization effects as seen for the vanadium analogue. In order to confirm that the Cr(III) emissions were due to the presence of the bis(cyclopentadienyl) chromium cation in the pores, we synthesized chromocenium triflate. The XPS spectrum of this brown compound (shown in Fig.32b)

gives the Cr 2p 1/2, 3/2 regions at 585.5 eV, 575.8 eV, virtually identical with the emissions for the Cr (III) species present in the composite at higher binding energy. The Nb 3d region of the XPS (Figure 32c) shows peaks at 207.2 eV and 210.0 eV for the 5/2 and 3/2 peaks, demonstrating that the walls of the mesostructure are only slightly reduced in this material compared to the starting material which shows emissions at 207.8 eV and 210.6 eV.³⁵ These data are consistent with a small degree of electron transfer into the walls of the mesostructure and formation of the bis-cyclopentadienyl chromium cation and other more highly oxidized species. The valence region near the Fermi level (Fig. 32d) shows a broad and complex hump for the Nb-O sp valence emission with a tail that ends at roughly 3.0 eV, consistent with other mesoporous niobium oxide composites studied.³⁵ The conductivity measurements of this material showed this material is semiconducting with a value of $10^{-6} \text{ohm}^{-1} \text{cm}^{-1}$ which compares to the mesoporous niobium oxide composites of other early-transition metal sandwich compounds such as bis(benzene) vanadium, bis(benzene) chromium, and bis(cyclopentadienyl) vanadium.

4.2.8. SQUID Measurements

SQUID magnetic measurements were conducted to further explore the magnetic behavior of this new composite. The M vs. T plot measured at 500 G is shown in Figure 8 and provides evidence for paramagnetic and possibly spin glass or superparamagnetic behavior of this material. The B vs. H plot for this material run at 100K to 5K gives a straight line with very small hysteresis, demonstrating that the paramagnetic contribution dominates the magnetic behavior of the system. The large hysteresis in Figure 33 can also be explained by a wide particle size distribution or a slight transition in the ZFC branch of the plot near 20 K indicative of superparamagnetic or spin glass behavior.

These two factors have been clearly shown by reduced two-member NbV mesoporous materials in our group.

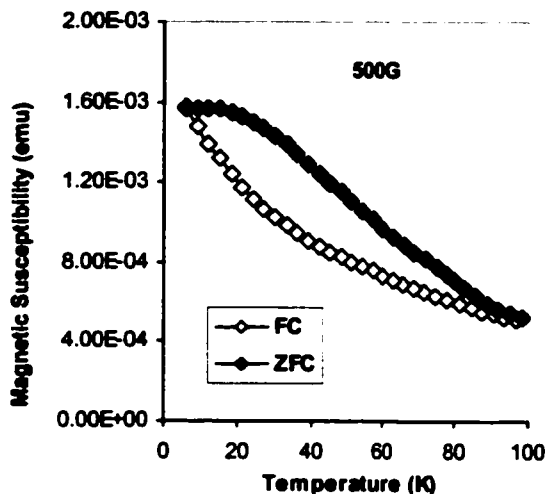


Figure 33. SQUID magnetometer plot of magnetic susceptibility per gram versus temperature (M vs. T) for a sample of mesoporous niobium oxide treated with excess bis(cyclopentadienyl) chromium showing the field cooled (FC) and zero-field cooled (ZFC) branches of the plot.

4.3. Discussion

In light of the insulating nature of mesoporous niobium oxide reduced with alkali metals the conductivity trends in these materials are best explained by a model in which the charge carrier involves the organometallic phase in the pores or on the surface of the material. Since treatment of amorphous non porous samples of niobium oxide, of similar average particle size to the mesoporous niobium oxide used in this study as judged by SEM, with bis(cyclopentadienyl) complexes of Cr and V leads to reduced materials with similar XPS spectra to the respective mesoporous composites but much lower conductivity (ca. $10^{-8} \text{ ohm}^{-1} \text{ cm}^{-1}$), it can be argued that the surface contribution to conductivity is negligible. Unpublished results in our group have demonstrated that samples of mesoporous niobium oxide prepared with 5 molar percent vanadium in the walls are insulating as are those same materials reduced with up to one equivalent

potassium naphthalene. This suggests that the role of higher oxidation state V residues in the structure in conductivity is also negligible and that any reduced vanadium in the walls is not important in the overall conductivity of these materials. Thus, conductivity in these composites is best attributed to mixed oxidation state V(II)/V(IV) or Cr(II)/Cr(III) chains in the pores which act as pseudo one-dimensional molecular wires where the hole induced by oxidation of a portion of the organometallic by the framework is likely the charge carrier. In previous work we found that the presence of the neutral species in the pores for bis(benzene) V and Cr composites of mesoporous niobium oxide was required for conductivity.⁷¹ This rules out any conductivity mechanism involving only the reduced mesostructure and the organometallic cation. While assignment of any discrete local structure to the organometallic phase within the pores is premature, further spectroscopic studies are ongoing to determine average intermolecular distances and orientations in the pores of the species in question. The distance between adjacent units is expected to be critical in such a model, as it is in the conductivity of one-dimensional Pt chains, however at room temperature there is likely enough thermal energy to allow enough motion of these individual units such that constant proximity is not a requirement and thermally induced collisions can facilitate electron mobility. This is certainly the case in most molecular metals, which possess high enough thermal vibration energy at room temperature to overcome charge density waves and Peierl's distortion which tend to cause electron localization and insulating behavior below a certain temperature threshold.⁶⁹ The role of oxidation state and electron configuration is less clear, however the dramatic difference in conductivity between cobaltocene loaded mixed oxidation state materials with 0.5 equivalents of Co (sum of Co(II) and Co(III)) and the materials under

study suggest that the electronic nature of the charge carriers is more important than absolute loading percent of the organometallic dopant.

Since conductivity in solids depends on Hubbard Potential ($U = I - A$), where I is the ionization potential and A is the electron affinity of the charge carrying species, and the bandwidth (W), quantifying these parameters in the systems under study may be helpful in understanding the trends in electronic behavior. If W is greater than U , the material will be conducting, if it is not then the material will be insulating. The Hubbard Potential can be estimated by considering the literature I values of 6.78 eV and 5.71 eV for bis(cyclopentadienyl) vanadium and chromium, respectively¹³⁷ along with the A values for the respective cationic species. Although the latter are not available in the literature, they can be estimated from A values for the neutral organometallic species and the corresponding oxides. The A values for $V(II)O$ and $V(IV)O_2$ are 1.23 eV¹³⁸ and 2.01 eV,¹³⁹ respectively, while that for bis(cyclopentadienyl) vanadium (II) is 0.68 eV.¹²⁴ Since the value for $V(II)O$ is higher than that of bis(cyclopentadienyl) vanadium (II), the cyclopentadienyl ligand environment alters the A value with respect to the O ligand environment by $(1.23 - 0.68) = 0.55$ eV. From this we can estimate the A value for the bis(cyclopentadienyl) vanadium (IV) dication as $(2.01 - 0.55) = 1.39$ eV. Likewise, considering the values of 0.88 eV, 1.22 eV, and 2.41 eV for the electron affinities of bis(cyclopentadienyl) chromium (II),¹²⁴ $Cr(II)O$,¹³⁸ and $Cr(IV)O_2$,¹³⁹ respectively (a reliable value for the A of $Cr_2(III)O_3$ is not available), and using half the difference between $Cr(II)O$ and $Cr(IV)O_2$ we can arrive at an estimation of 1.47 eV for the A of the bis(cyclopentadienyl) chromium (III) cation. Thus, U for the V system can be estimated as $(6.78 - 1.39) = 5.39$ eV while that for the Cr system can be estimated as $(5.71 - 1.47)$

= 4.24 eV. While W is difficult to calculate in an amorphous composite system, comparisons to values for the elements may still be helpful in the systems under study, since all other factors such as cyclopentadienyl ligand environment, organometallic loading level, and temperature (influencing thermal motion and charge carrier collision frequency) are roughly equal. From the estimated U calculated above and the band width W of 6.77 eV for V and 6.56 for Cr calculated assuming a body-centered cubic structure,¹⁴⁰ it would appear that conductivity in both systems should be favorable due to the 1.38 eV and 2.32 eV value for $(W - U)$ for the V and Cr systems, respectively.

Applying this model to the cobaltocene materials is valuable in understanding the origin of conductivity in this family of composites, since these materials possess a much higher loading level than the V and Cr systems by almost a factor of 50, yet are still insulating. The Hubbard potential U can be calculated from an I of 5.56 eV¹³⁷ for cobaltocene and an A estimated from the sum of the A value for cobaltocene and one-half the difference between the A value for Co(II)O ¹³⁸ and Co(IV)O ,¹³⁹ given that the literature A value for $\text{Co}_2\text{(III)O}_3$ is not available. This gives a value of 4.30 eV for U , while W for Co is 4.35 eV.¹⁴⁰ The difference between U and W of 0.05 eV is almost negligible and would thus be expected to lead to a much more insulating material than the Cr and V systems, which have much larger and more favorable values for $W - U$ of 1.38 eV and 2.32 eV, respectively. It thus appears that the governing factor in conductivity in this system is likely the balance between U and band width W of the transition metal in question, which is known to decrease monotonically across a table due to an increase in effective nuclear charge. This explanation is commonly invoked to explain the conductivity trends of simple monoxides from TiO to CoO across the periodic table.¹⁴⁰

However, owing to the amorphous nature of the material as well as the potential degree of state crossing and orbital mixing between the a and e levels of the metallocene systems, specific band assignments for these materials are as yet ambiguous.

4.4. Conclusion

In summary, treatment of mesoporous niobium oxide with bis(cyclopentadienyl) V and Cr led to materials with pseudo-one dimensional mixed oxidation-state metallocene wires in the pore structure. The specific nature of the species present was confirmed by EPR, UV, and XPS to show that the structural integrity of the organometallic was retained after electron transfer to the niobium oxide framework. The conductivity in these materials was attributed to the oxidation-induced hole in the organometallic phase in light of the fact that all samples of alkali metal reduced mesoporous niobium oxide are insulating. The trends in conductivity from V and Cr to Co fit well into the model predicted from considering estimated bandwidth and the Hubbard potential.

Chapter 5. Electronic and Magnetic Properties of Bis-benzene Chromium Composites of Mesoporous V-Nb Mixed Oxides

In Chapter 2, it was shown that the reaction of mesoporous niobium oxide with bis(benzene) chromium leads to semiconducting materials with a mixed oxidation state organometallic phase in the pores.¹⁰⁶ However, only small amounts (2 weight %) of bis-benzene chromium are oxidized by the mesoporous niobium oxide due to the limited availability of low lying acceptor states in the niobium oxide phase strong enough to oxidize the organometallic. In order to conduct a study of the variation of electronic properties with the bis(benzene) chromium loading level it is therefore necessary to increase the oxidizing ability of the mesostructure by doping it with a more highly oxidizing species. Herein, is reported the synthesis of a new family of V-doped mesoporous niobium oxide materials in which the sequential increase in V-content controls the level of bis(benzene) chromium in the structure by tuning the ability of the structure to function as an oxidizing agent. Contrary to expectation, the conductivity of these materials was found to decrease monotonically with the Cr loading level, suggesting that the ratio of species present in the pores is more important than the absolute loading level of the organometallic. ²H-NMR experiments were also conducted on the perdeutero analogues of these composites to probe into the nature of internal electron hopping in these materials.

5.1. Experimental Section

5.1.1. Materials and Equipment

All chemicals unless otherwise stated were obtained from Aldrich. All other materials and equipment unless otherwise stated were the same as those shown in Chapter 2. Bis(benzene) chromium was obtained from Strem Chemicals. Bis(hexadeuterobenzene) chromium was synthesized according to the literature,¹⁴¹ but perdeuterobenzene was in place of benzene as starting reagent. Bis(benzene) chromium iodide and bis(hexadeuterobenzene) chromium iodide were made according to literature.¹⁴² Mesoporous niobium oxide was made according to the method of Antonelli and Ying.²⁴

The solid state NMR spectra were recorded on 400 MHz MAS-NMR spectrometer without cross polarization. All elemental analysis data (conducted under an inert atmosphere) were obtained from Galbraith Laboratories, 2323 Sycamore Drive, Knoxville, TN 37921-1700.

5.1.2. Synthesis

Mesoporous V-Nb mixed oxides were prepared by the ligand-assisted templating method,²⁴ except 5, 10, or 20 mole percent of vanadium (V) tri-isopropoxy oxide with respect to Nb were added to the Nb (V) ethoxide prior to addition of the octadecylamine template and subsequent hydrolysis/condensation steps. Elemental analysis gave the following results, respectively, for the three as-synthesized samples: 1: Nb, 45.31%; V, 1.30%; C, 0.50%; H, 2.09%; N, less than 0.03%; O, 50.70%; 2: Nb, 40.41%; V, 1.80%; C, 2.01%; H, 2.29%; N, less than 0.03%; O, 53.39%; 3: Nb, 42.80%; V, 3.45%; C, 0.51%; H, 2.40%; N, less than 0.03%; O, 50.79%. The elemental formula of these materials can be calculated as $\text{Nb}_{1.0}\text{V}_{0.05}\text{O}_{6.5}\text{C}_{0.09}\text{H}_{4.7}$, $\text{Nb}_{1.0}\text{V}_{0.08}\text{O}_{7.7}\text{C}_{0.4}\text{H}_{5.3}$, and $\text{Nb}_{1.0}\text{V}_{0.15}\text{O}_{6.9}\text{C}_{0.09}\text{H}_{5.2}$, respectively for 1, 2, and 3.

Bis(benzene) chromium reduced mesoporous V-Nb oxide composites (7, 8, 9) were synthesized by addition to a suspension of the trimethylsilyl chloride treated mesoporous V-Nb oxide (4, 5, 6) in dry benzene an excess of bis(benzene) chromium calculated on the basis of sample weight and percentage of Nb. The mesoporous solid immediately turns from light yellow to gray-yellow. After several days of additional stirring to ensure complete absorption of the organometallic, the reduced material is collected by suction filtration and washed several times with benzene. The material is dried *in vacuo* at 10^{-3} torr on a Schlenk line until all condensed volatile had been removed. All reduced oxides in this study were prepared in an analogous fashion. The C, H elemental analysis is summarized in Table 3 in the Results and Discussion section.

5.2. Results and Discussion

5.2.1. Nitrogen Adsorption Study and XRD Patterns of As-synthesized Mesoporous V-Nb Oxides

The nitrogen adsorption and desorption isotherms of the mesoporous V-Nb oxides 1, 2, and 3 are shown in Figure 34a. The BET surface area, HK pore size and pore volume of these samples are summarized in Table 4 and compared to a sample of mesoporous niobium oxide prepared without addition of the V dopant. The type IV isotherm exhibited in all cases is indicative of mesoporosity, while the lack of hysteresis demonstrates that the template was removed successfully without significant loss of structure. Figure 34b shows the plots of incremental pore volume versus average pore diameter for materials 1, 2, and 3, indicating that a sharp pore size distribution was obtained upon removal of the template. The worm-hole mesostructure of these materials

was reflected in the powder X-ray diffraction (XRD) patterns, which show a broad peak centered at $d(100)$ spacing = 40 Å for these materials (Figure 35).

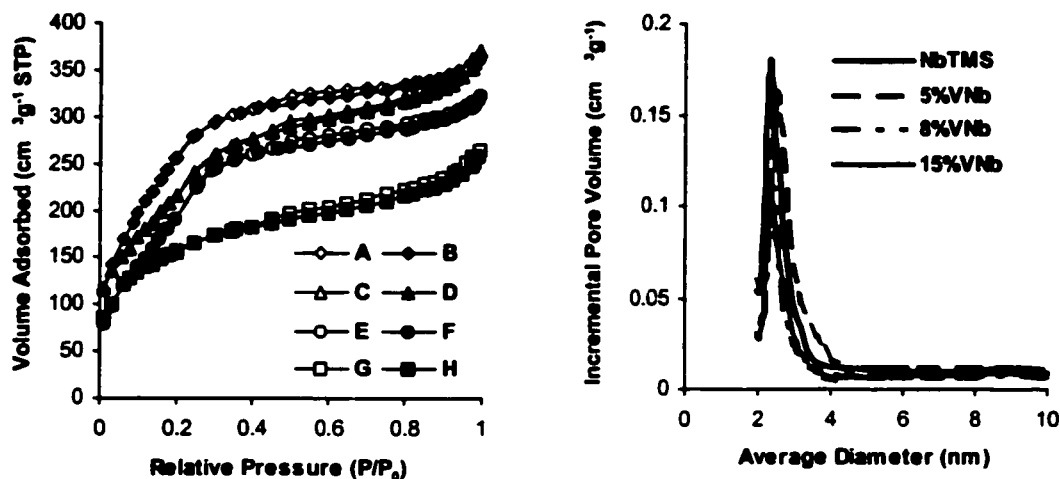


Figure 34. (a, left) Nitrogen adsorption (B, D, F, H) and desorption (A, C, E, G) isotherms of mesoporous Nb oxide (A, B), mesoporous 5%V-Nb oxide (C, D), mesoporous 8%V-Nb oxides (E, F) and mesoporous 15%V-Nb oxide (G, H), (b, right) plots of incremental HK pore volume versus average pore diameter for materials from (a).

Table 4. BET surface area, pore size and pore volume of the as-synthesized mesoporous vanadium-niobium oxides

Samples	BET surface area (m ² g ⁻¹)	HK pore size (Å)	Pore Volume (cm ³ g ⁻¹)
NbTMS	861	23.1	0.531
Meso-5%VNb (1)	832	25.7	0.511
Meso-8%VNb (2)	761	24.0	0.436
Meso-15%VNb (3)	538	23.2	0.341

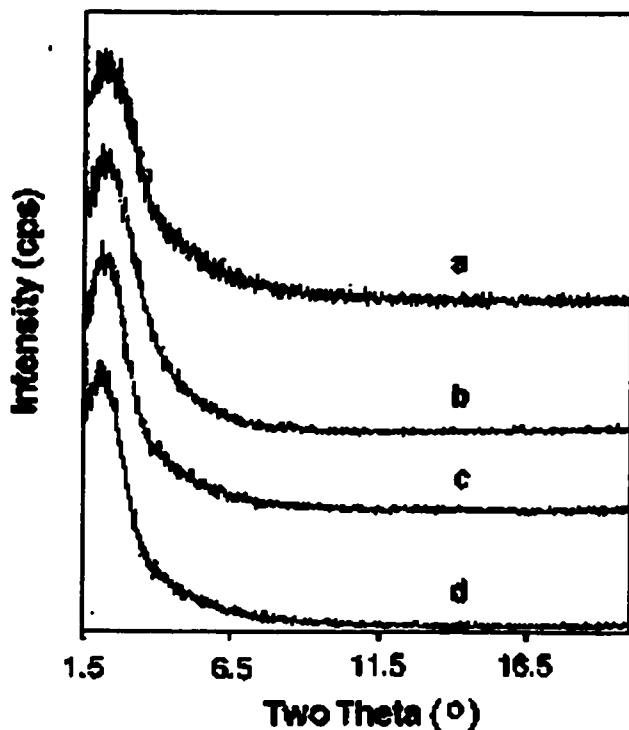


Figure 35. XRD patterns of (a) mesoporous niobium oxide, (b) 1, (c) 2, and (d) 3.

5.2.2. EPR Spectra of As-synthesized Mesoporous V-Nb Oxides

Figure 36 shows electron paramagnetic resonance (EPR) spectra of material 1. The three vanadium-doped samples show similar hyperfine splittings originating from the ^{51}V nucleus ($I = 7/2$). These splittings are the combination of double eight lines as vanadium nucleus is parallel (eight lines) and perpendicular (eight lines) to the magnetic field. The simulation of this spectrum gave the following hyperfine splitting Hamiltonian parameter A and g value: $A(x, x) = 76.50 \text{ G}$, $A(y, y) = 76.50 \text{ G}$, $A(z, z) = 191.50 \text{ G}$, $g(x) = 1.979$, $g(y) = 1.979$, $g(z) = 1.929$, indicative of vanadium (IV) in the sample.¹⁴³ The clear hyperfine splitting obtained indicates vanadium (IV) species is very well dispersed in the Nb oxide bulk structure, otherwise, the vanadium nuclei with unpaired electrons would interact with each other to result in hyperfine splitting disappearance. The presence of

V(IV) in the sample can be accounted for by reduction of the V(V) during the synthesis process, possibly by the amine template or isopropanol formed by hydrolysis of the V precursor. Since V(V) is not spin active, it is impossible to tell by this method what the ratio between V(IV) and V(V) in the material is. When the sample was heated at 100 °C for 4 hours, the EPR signal from vanadium (IV) disappeared, indicating that it had been completely oxidized into vanadium (V). The nitrogen adsorption and desorption data showed the mesostructure was completely retained after oxidation of V (IV), suggesting that this method is an effective way to produce single-valent vanadium (V)-doped mesoporous niobium oxides.

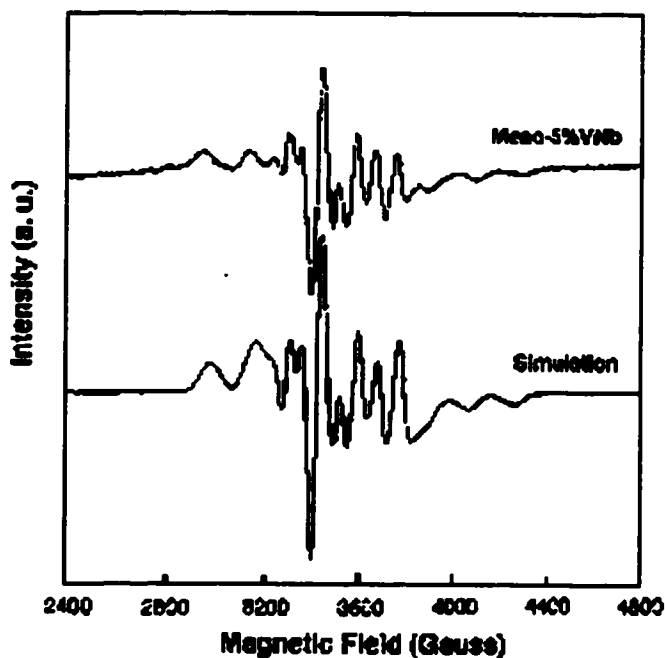


Figure 36. Powder EPR spectrum of 1 and the simulation of this spectrum.

5.2.3. XPS Spectra of As-synthesized Mesoporous V-Nb Oxides

The X-ray photoelectron spectra of 1, 2, and 3 are shown in Figure 37. Figure 37a shows the V 2p $1/2$, $3/2$ regions with a series of asymmetric emissions which can be

assigned to a mixture of V(V) (516.5 eV, 524.1 eV) and V(IV) (515.0 eV, 522.2 eV) according to the literature values for the corresponding oxides.^{116,144} As expected, the intensity of the peaks increases monotonically with the increase in V content.

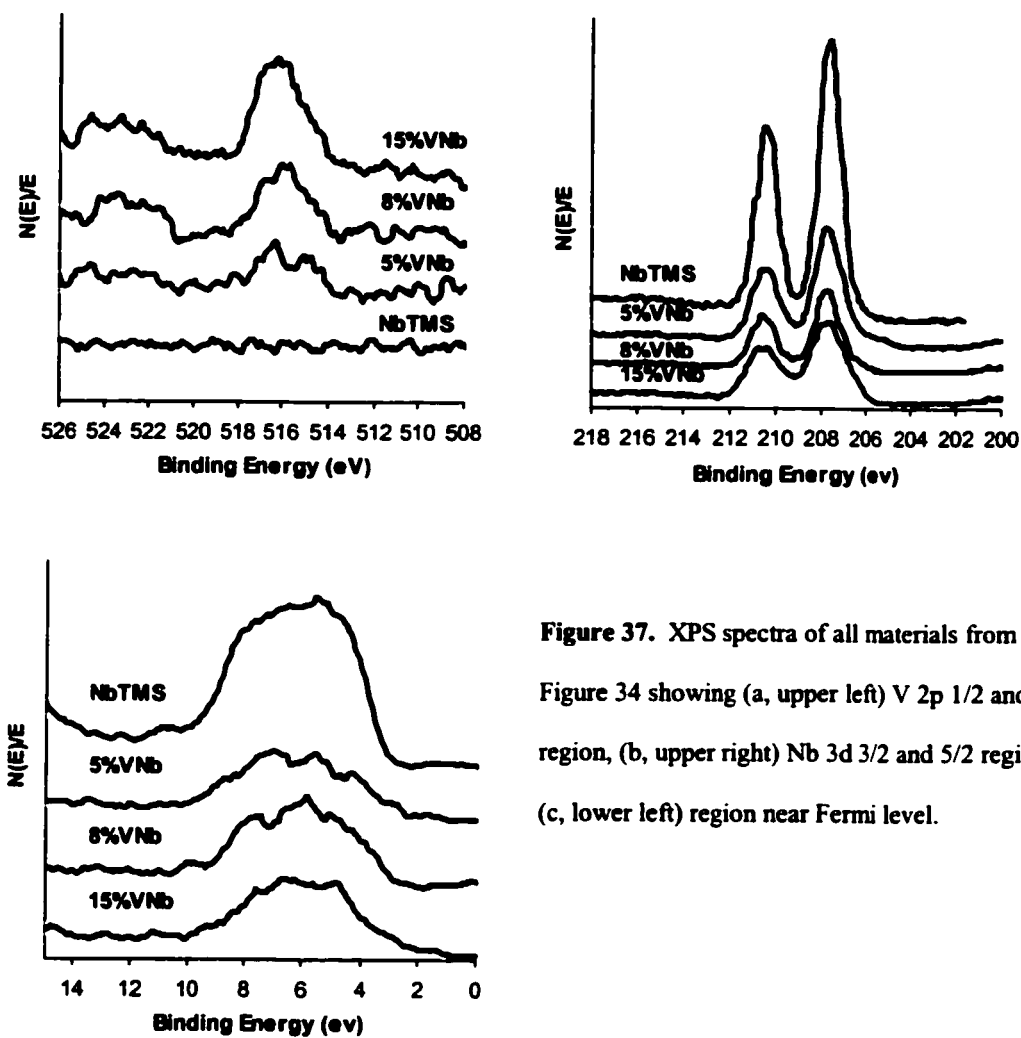


Figure 37. XPS spectra of all materials from Figure 34 showing (a, upper left) V 2p 1/2 and 3/2 region, (b, upper right) Nb 3d 3/2 and 5/2 region, (c, lower left) region near Fermi level.

Figure 37b shows the Nb 3d region with the 5/2 and 3/2 emission peaks located at 207.6 eV, 210.4 eV, consistent with Nb (V).¹⁰⁶ The valence region near Fermi level are shown in Figure 37c, yielding an approximate distance to the Fermi level of 3.0 eV for oxygen 2p valence emission.

5.2.4. Nitrogen Adsorption Study, XRD Patterns and Elemental Analysis of Bis(benzene) Chromium Composites of Mesoporous V-Nb Mixed Oxide

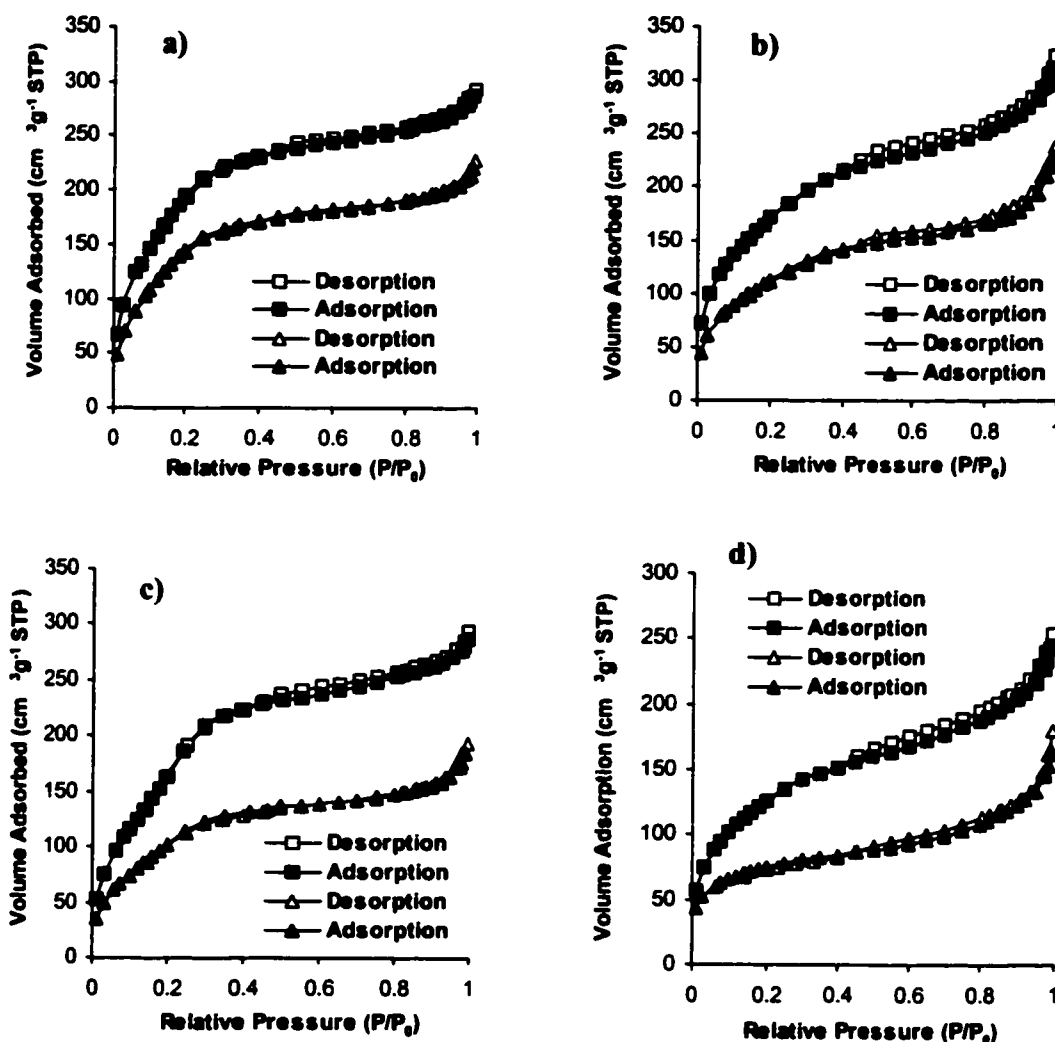


Figure 38. Nitrogen adsorption and desorption isotherms of (a) trimethylsilated mesoporous niobium oxide before (upper) and after (lower) treatment with excess bis(benzene) chromium, (b) trimethylsilated mesoporous 5%V-Nb oxide (4) before (upper) and after (7) (lower) treatment with excess bis(benzene) chromium, (c) trimethylsilated mesoporous 8%V-Nb oxide (5) before (upper) and after (8) (lower) treatment with excess bis(benzene) chromium, and (d) trimethylsilated mesoporous 15%V-Nb oxide (6) before (upper) and after (9) (lower) treatment with excess bis(benzene) chromium.

Previous studies in our group demonstrated that the degree to which mesoporous Nb oxide can absorb and retain an organometallic dopant depends largely on the ability of that dopant to reduce the transition metal oxide walls.^{107,108,145} This observation is of great importance because the amount of dopant in the pore structure can greatly influence its physical properties. For example, increasing the cobaltocene-to-niobium ratio in a series of mesoporous niobium oxide cobaltocene composites from 0.1:1 to 0.5:1 leads to a transition from paramagnetic to superparamagnetic behavior.⁷² Since mesoporous Nb oxide only absorbs ca. 0.07 equivalents of bis(benzene) chromium,¹⁰⁶ in order to explore the effect on electron transport and magnetic properties of increasing the bis(benzene) chromium content, the walls of the mesostructure have to be modified to make it a more effective electron acceptor. Because V (V) is a stronger oxidant than Nb (V), adding varying amounts of V to the walls should increase the capacity for the mesostructure to absorb higher levels of a dopant and thus allow us to study mesoporous composites with much higher levels of bis(benzene) chromium in the pore structure in an effort to establish trends relating composition and electronic or magnetic properties.

In a preliminary step, samples of 1, 2, and 3 were treated with excess trimethylsilyl chloride to give materials 4, 5, and 6. This procedure is necessary to preserving the integrity of the mesostructure after reduction, because it removes surface water and caps surface hydroxyl groups which may form nucleophilic oxygen species, which effect the mesostructure, after reduction. Materials 4, 5, and 6 were then treated with excess bis(benzene) chromium over several days to ensure complete reaction to give reduced composites 7, 8, and 9. The BET surface area, HK pore size and pore volume for all reduced samples are shown in Table 5.

Table 5. BET surface area, pore size and pore volume of trimethylsilylated vanadium-doped mesoporous niobium oxides and the corresponding bis(benzene) chromium composites. The data for pure trimethylsilylated mesoporous niobium oxide synthesized with a dodecylamine template before and after treatment with bis (benzene) chromium is also shown.

Samples	BET surface area (m ² g ⁻¹)	HK pore size (Å)	Pore Volume (cm ³ g ⁻¹)
NbTMS	771	23.1	0.434
Meso-5%VNb (4)	721	25.7	0.412
Meso-8%VNb (5)	691	24.0	0.388
Meso-15%VNb (6)	457	23.2	0.331
NbCr	642	22.0	0.364
5%VNbCr (7)	557	23.2	0.332
8%VNbCr (8)	487	23.0	0.286
15%VNbCr (9)	296	22.2	0.202

The nitrogen adsorption and desorption isotherms of these materials before and after reduction with bis(benzene) chromium are shown in Figure 38. The loss of surface area on absorption of the organometallic has been commented on previously.¹⁰⁶ The XRD patterns of all new materials exhibited the same d-spacing as the starting material (Figure 39), indicating retention of the mesostructure on reduction by the organometallic. The elemental analysis of these new materials shows an increase of carbon and hydrogen percentage on intercalation, further confirming that the organometallic was absorbed into the pore structure. The results are summarized in the Table 6. The percentage of Cr can be estimated from the increase in carbon as 0.97%, 1.27%, and 2.18% for 7, 8, and 9, respectively. In previous studies on bis(arene) and bis(cyclopentadienyl) metal

composites of mesoporous Nb oxide, the metal percentage from inductively coupled plasma analysis of the organometallic was virtually identical to that value estimated from the increase in carbon.

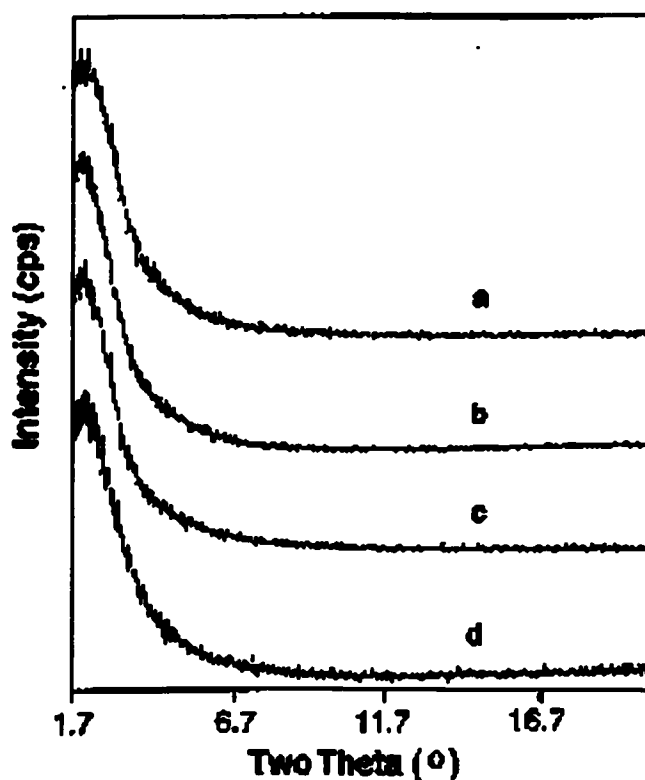


Figure 39. XRD patterns of trimethylsilated mesoporous transition metal oxides from Figure 1 after treatment with excess bis(benzene) chromium (a) mesoporous niobium oxide, (b) 5%VNb, (c) 8%VNb, and (d) 15%VNb.

Table 6. Carbon and hydrogen elemental analysis results of the mesoporous transition metal oxides before and after reduction with bis(benzene) chromium.

Samples before reduction	Carbon (wt. %)	Hydrogen (wt. %)	Samples after reduction	Carbon (wt. %)	Hydrogen (wt. %)
NbTMS1	5.73	1.43	NbCr	7.24	1.75
Meso-5%VNb (4)	5.30	1.49	5%VNbCr (7)	7.98	2.05
Meso-8%VNb (5)	4.65	1.77	8%VNbCr (8)	8.18	2.39
Meso-15%VNb (6)	6.72	1.37	15%VNbCr (9)	12.76	2.77

Inspection of Table 6 reveals that the carbon content after treatment with bis(benzene) chromium increases monotonically with increased percentage of V in the samples. This is consistent with the increased oxidizing ability of the materials with a higher V content and demonstrates that the oxidizing ability of the walls can be adjusted by the addition of this dopant to the structure.

5.2.5. EPR Spectra of Bis(benzene) Chromium Composites of Mesoporous V-Nb Mixed Oxide

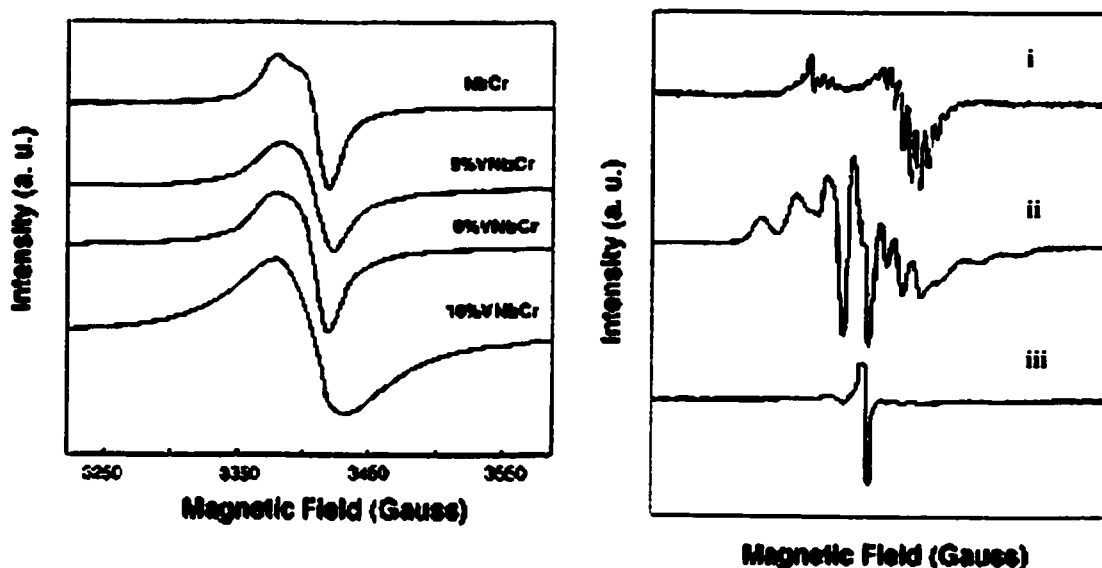


Figure 40. (a, left) EPR spectra of all materials from Figure 6; (b, right) samples of (i) mesoporous niobium oxide treated with 0.001 equivalent of bis(benzene) chromium, (ii) sample 5 treated with 0.001 equivalent of bis(benzene) chromium, and (iii) sample 5 treated with 0.003 equivalent of bis(benzene) chromium.

Figure 40a shows the electronic paramagnetic resonance (EPR) spectra of Nb-TMS1 and the mesoporous V-Nb oxide composites reduced by bis(benzene) chromium. All samples show a large resonance at $g = 1.98$ originating from the bis(benzene) chromium

cation. The broadened nature of the resonances suggests that there may be other spin active species present. Figure 40b shows EPR spectra of the sample which was made from mesoporous niobium oxide and 0.001 equivalent of bis(benzene) chromium (i), and sample 5 after treatment with 0.001 or 0.003 equivalent of bis(benzene) chromium (ii and iii). The V (IV) hyperfine splittings in the unreduced starting materials are obscured by the bis(benzene) chromium cation resonance at $g = 1.98$, which increases in intensity with higher loading levels. The clear proton hyperfine splittings ($\alpha_H = 3.43\text{G}$, $g = 1.98$), characteristic of the bis(benzene) chromium cation,¹¹⁰ were obtained in the sample of mesoporous niobium oxide reduced with 0.001 equivalent of bis(benzene) chromium. The disappearance of the V (IV) hyperfine splitting in the reduced vanadium-doped mesoporous niobium oxide samples is due to the strong electron – electron interaction in this system because the V (V) in the starting materials had been reduced into V (IV) by bis(benzene) chromium. The peak at $g = 2.00$ from free electrons in the mesostructure, observed in many reduced mesoporous niobium oxides studied in our group, was not resolved in this case, most likely because it is obscured by the strong signal for the bis(benzene) chromium cation. These data indicate that the mesoporous structure was reduced by bis(benzene) chromium to give a new material with V(IV) in the walls and the bis(benzene) chromium cation in the pore channels.

5.2.6. XPS Spectra of Bis(benzene) Chromium Composites of Mesoporous V-Nb Mixed Oxide

The XPS studies of the mesoporous V-Nb oxides after reaction with bis(benzene) chromium (7, 8, and 9) further confirm the reduction of the mesostructure. Figure 41a shows the V 2p (1/2, 3/2) region, exhibiting asymmetric emissions centered at 515.0 eV

and 522.0 eV. These emissions are broader and centered at much lower binding energy than those for the unreduced material shown in Figure 37a, indicating a more complete reduction to V(IV) in the former materials. The broadness of the emissions suggests that

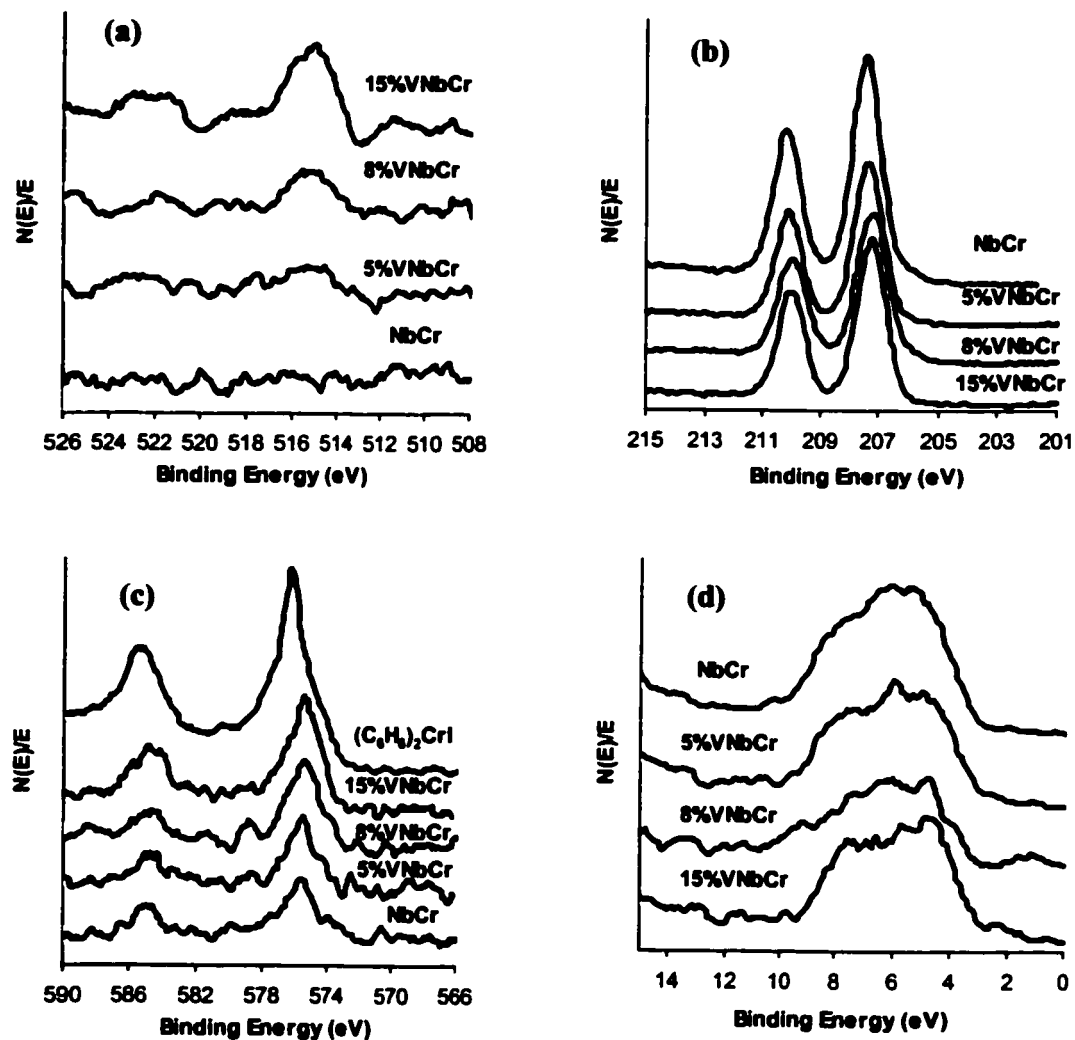


Figure 41. XPS spectra of all materials from Figure 6 after treatment with excess bis(benzene) chromium showing (a) V 2p 1/2 and 3/2 regions, (b) Nb 3d 3/2 and 5/2 regions, (c) Cr 2p 1/2 and 3/2 regions, and (d) region near Fermi level.

there is still V(V) remaining in the reduced materials, and that there are V sites in the walls that are perhaps too isolated for reduction by a reagent introduced on the surface of the pore channels. As expected, the intensity of the emissions increases with increased percentage of V. Figure 41b shows the Nb 3d (5/2, 3/2) region. The emissions appear at lower binding energy (207.1 eV and 209.9 eV) as compared to the starting materials at 207.6 eV and 210.4 eV. These data indicate that some surface Nb sites have also been reduced by the organometallic. Figure 41c shows the chromium 2p (3/2, 1/2) region of the reduced materials, with emissions at 575.5 eV and 585.1eV, consistent with neutral bis(benzene)chromium.¹¹² The bis(benzene)chromium(I) cation was not clearly resolved as compared with the XPS data from bis(benzene)chromium iodide (Figure 41c top curve), indicating the Cr⁰/ Cr^I ratio is in favor of the neutral species. As predicted from the elemental analysis, these emissions increase in intensity as the vanadium component increases in the materials. Figure 41d shows the region near Fermi level with an approximate distance to Fermi level of 3.0eV for the metal-Oxygen sp valence emission.

5.2.7. Conductivity Measurement of Bis(benzene) Chromium Composites of

Mesoporous V-Nb Mixed Oxide

Table 7 shows the effects of vanadium content in the materials on the room temperature four-point DC conductivity of bis(benzene) chromium reduced mesoporous V-Nb oxide composites. Materials 1-6 were insulating before reduction by the organometallic. Previous work in our group showed that increasing the loading level of bis(benzene) chromium in mesoporous niobium oxide from Cr:Nb ratios of 0.01:1 to 0.07:1 led to an increase of conductivity and that the electron transport mechanism appeared to involve a mixed oxidation state bis(benzene) chromium-bis(benzene)

chromocinium phase in the pore channels.¹⁰⁶ Estimations of the bandwidths and Hubbard potentials of these materials do not preclude such a mechanism where the electron moves by a hopping process between the Cr(0) and Cr(I) centers. The insulating nature of mesoporous niobium oxide reduced with varying amounts of alkali metal or cobaltocene suggest that the walls do not participate in the electron transport mechanism. Close inspection of Table 7 shows that materials 7, 8 and 9 afford a decrease in conductivity with increasing V, and therefore bis(benzene) chromium content. This is contrary to what was observed for the V-free bis(benzene) chromium reduced mesoporous Nb oxides discussed above. Moreover, virtually all reduced mesoporous oxides with alkali fulleride⁸³ or organometallic^{107,108,145} in the pores show an increase in conductivity with increased dopant level. The reason for the decreased conductivity on increase of bis(benzene) chromium in the present study is not understood, but could be related to a different conductivity mechanism in these materials as compared to the V-free starting materials, in which the V in the walls acts as an electron trap, or effects related to different ratios of Cr (I) to Cr (0) bis(benzene) complexes in the pores. Variable temperature conductivity studies on these materials showed that the conductivity dropped sharply with the decrease of the temperature, indicating that these materials are semiconductors.

Table 7. The effects of vanadium contents on the conductivity of bis(benzene) chromium reduced mesoporous V-Nb oxide composites.

Samples	0.6 wt. equ. ^a	0.1 wt. equ. ^a	0.05 wt. equ. ^a	0.01 wt. equ. ^a
	(ohm ⁻¹ cm ⁻¹)	(ohm ⁻¹ cm ⁻¹)	(ohm ⁻¹ cm ⁻¹)	(ohm ⁻¹ cm ⁻¹)
NbTMS1+(C ₆ H ₆) ₂ Cr	1.36×10 ⁻⁵	6.88×10 ⁻⁶	2.26×10 ⁻⁶	4.24×10 ⁻⁷

5%VNb (4)+(C ₆ H ₆) ₂ Cr	4.52×10 ⁻⁶	1.70×10 ⁻⁶	2.20×10 ⁻⁷	Insulating ^b
8%VNbCr (5)+(C ₆ H ₆) ₂ Cr	1.13×10 ⁻⁶	5.24×10 ⁻⁷	insulating ^b	insulating ^b
15%VNbCr (6)+(C ₆ H ₆) ₂ Cr	insulating ^b	insulating ^b	insulating ^b	insulating ^b

- a The numbers are the weight ratio of added (C₆H₆)₂Cr to the mesoporous transition metals oxides.
- b Insulating refers to conductivity is lower than 10⁻⁸ ohm⁻¹cm⁻¹.

5.2.8. SQUID Measurements of Bis(benzene) Chromium Composites of Mesoporous V-Nb Mixed Oxides

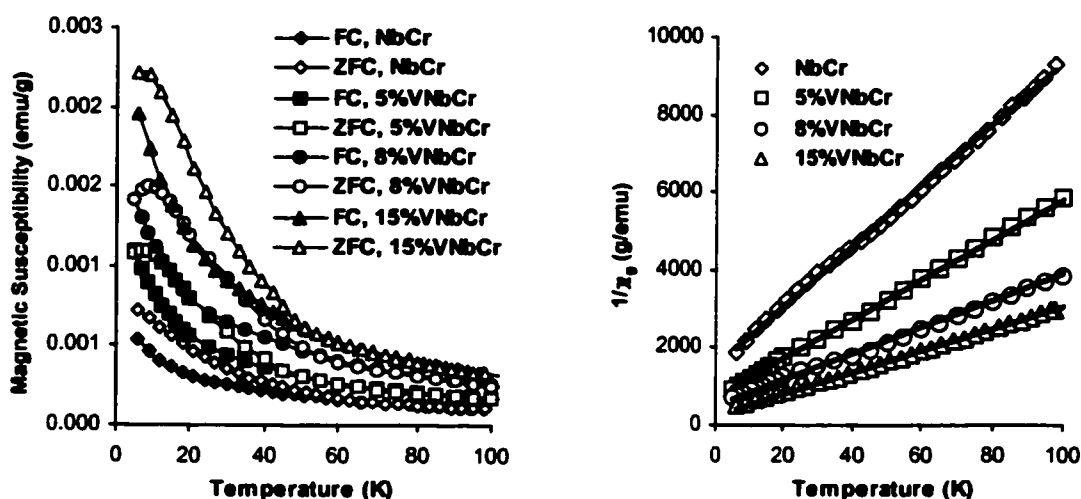


Figure 42. SQUID magnetometer plots of (a, left) magnetic susceptibility versus temperature, and (b, right) variation of inverse magnetic susceptibility with temperature for all materials from Figure 39.

Figure 42a shows the superconducting quantum interference detector (SQUID) magnetometer plots of the magnetic susceptibility versus temperature for the composites 7, 8, and 9. The slight transition at 10 K in the ZFC branch of the plots indicates some degree of spin glass behavior. Figure 42b shows the variation of inverse magnetic susceptibility with temperature over the temperature range from 6 to 100 K, indicating

that these materials obey the Curie-Weiss law where $\chi_m = C/(T-\theta)$, where C is Curie constant and θ is Weiss constant. The effective magnetic moment μ_{eff} can be calculated from the equation $C = N \mu_B^2 \mu_{\text{eff}}^2 / 3\kappa$, where, N is Avogadro number, μ_B is Bohr magneton, κ is Boltzmann constant.¹⁴⁶ The results are summarized in Table 8. The sample with the highest V and Cr loading (9) has the largest number of unpaired electrons of these samples, while the sample made from V-free Nb-TMS1 and bis(benzene) chromium has the smallest number of unpaired electrons, and the lowest Cr loading level. This result is also fully consistent with the data from XPS studies. The negative Weiss constant is consistent with spin glass behavior, also observed in other bis(benzene) and bis(cyclopentadienyl) transition metal doped materials studied in our group.^{107,108}

Table 8. Curie constants, Weiss constants and effective magnetic moments of the samples made from mesoporous transition metal oxide and excess bis(benzene) chromium

Samples	C (emu g ⁻¹ K)	θ (K)	μ_{eff}
NbCr	0.0127	-18.869	0.1008
5%VNbCr (7)	0.0197	-14.089	0.1255
8%VNbCr (8)	0.0291	-13.71	0.1525
15%VNbCr (9)	0.0354	-8.6086	0.1682

5.2.9. Solid State ²H-NMR Studies

In order to gain more insight into the nature of the charge carrying species in the pores, ²H-NMR studies were conducted on the d₆-benzene analogues of 7, 8, and 9. The deuterium chemical shift of the neutral bis(hexadeuterobenzene) chromium and its cation iodide are -2.3 ppm and 224 ppm as compared with hexadeuterobenzene(C₆D₆). The

sample made from mesoporous niobium oxide and bis(hexadeuterobenzene) chromium yielded two broad peaks at 280 ppm and 5 ppm which can be assigned to bis(hexadeuterobenzene) chromium(I) cation and its neutral species according to simulations. The peak from bis(hexadeuterobenzene) chromium neutral species is much bigger than that from the cation species, consistent with the results from the XPS spectra. The high chemical shift to down field as compared to its pure compound can be ascribed to the paramagnetic nature of the material.

5.3. Conclusion

In summary, we have synthesized a new series of mesoporous mixed V-Nb oxides and reduced these materials with bis(benzene) chromium. The increased amount of organometallic absorbed with increased V(V) shows that it is possible to tune the oxidizing strength of the walls of mesoporous niobium oxide by varying the amount of V in a new family of mesoporous V-Nb oxides. This property allowed us to study the effect of a composition on the conductivity and magnetic properties of these composites. Surprisingly, the conductivity drops with increased bis(benzene) chromium, contrary to other reduced mesoporous oxides we have studied.

Chapter 6. Magnetic Properties of Decamethylsamarocene Composites of Mesoporous Niobium Oxide

The exploration of materials with two or more disparate phases interwoven into a periodic array on the nanometer scale is of much current interest due to the potential of such materials to offer properties not observed in the corresponding pure phases. Previous work in our group demonstrated that Cp_2Ni and Cp_2Co reduced mesoporous niobium oxide composites are insulating superparamagnetic or spin glasses depending on the loading level. Superparamagnetism is a property associated with fine grains of ferromagnetic materials in which the domain size is too small to overcome randomization introduced by temperature.¹⁴⁶ Bulk samples of cobaltocene are not ferromagnetic, so the source of the magnetic interaction leading to superparamagnetism in mesoporous niobium oxide cobaltocene composites is not known. Since lanthanide elements have interesting optical and magnetic properties due to the high density of isolated f-states in the materials,⁶⁹ we wanted to synthesize reduced mesoporous composites with mixed oxidation state organolanthanide species in the pores to investigate what effect these had on the physical properties of the composites. In particular, we were interested in magnetic properties, since lanthanide dopants are known to have a dramatic effect on magnetic alloys, often increasing the remanent magnetism of ferromagnetic materials. For example, SmCo_5 is one of the best magnetic materials known. Also, the physical properties of such composites may shed light on the source of superparamagnetism in the cobaltocene composites.

6.1. Experimental Section

6.1.1. Materials and Equipment

All chemicals unless otherwise stated were obtained from Aldrich. All other materials and equipment unless otherwise stated were the same as those shown in preceding chapters. Samarium(II) iodide was obtained from Strem Chemicals. Decamethylsamarocene, $(C_5Me_5)_2Sm(THF)_2$, was synthesized by the literature method,¹⁴⁷ and was characterized by 1H -NMR. Anal. Calcd for $C_{28}H_{46}O_2Sm$: C, 59.52; H, 8.21; O, 5.66; Sm, 26.61. Found: C, 59.31; H, 8.01; O, 5.76; Sm, 26.77.

All elemental analysis data (conducted under an inert atmosphere) were obtained from Galbraith Laboratories, 2323 Sycamore Drive, Knoxville, TN 37921-1700.

6.1.2. Synthesis

Decamethylsamarocene-mesoporous Nb oxide composites were synthesized by addition of trimethylsilyl chloride-treated mesoporous niobium oxide (Nb-TMS1) to a THF solution of excess decamethylsamarocene calculated on the basis of molar ratio of Sm to Nb according to the ICP elemental analysis of the parent mesoporous oxide. The mesoporous solid immediately went from faun to black in color. After several days of additional stirring to ensure complete absorption of the organometallic, the reduced material was collected by suction filtration and washed several times with THF. The material was collected from the filter and dried *in vacuo* at 10^{-3} torr on a Schlenk line until all condensed volatile had been removed. The elemental analysis gave: Sm, 9.65%; Nb, 41.52%; O, 32.53%; C, 11.78%; H, 1.90%; Si, 2.60%; I, less than 19 ppm; N, less than 0.05%. On the basis of these data, the formula of this material can be written as $Nb_{1.0}O_{4.5}Sm_{0.14}Si_{0.21}C_{2.2}H_{4.2}$.

6.2. Results and Discussion

6.2.1. XRD Patterns and Nitrogen Adsorption Studies

Reduction of mesoporous niobium oxide by organometallic transition metal sandwich complexes has been studied extensively by our group. These topotactic host guest inclusion reactions generally lead to materials with a reduced Nb oxide mesostructure and one or more organometallic species in the pores. Most commonly, mixtures of the neutral organometallic and its corresponding cation are observed, imparting a net positive charge to the encapsulated phase which balances out the negative charge of the framework. Of special interest are mesoporous Nb oxide cobaltocene composites, because these materials exhibit superparamagnetism. This is surprising, given that this phenomenon is normally observed in fine grains of materials which are ferromagnetic in the bulk state, and pure cobaltocenium is paramagnetic. This suggests that different magnetic coupling processes are operative in the mesoporous composites, possibly involving interactions between the spins in the walls and those in the pores. Because lanthanides are often added to ferromagnetic metals in order to improve magnetic properties, the reduction of mesoporous niobium oxide with an organolanthanide complex could lead to mesoporous composites with novel magnetic properties and possibly help clarify the origin of superparamagnetism in the cobaltocene analogues. Decamethylsamarocene is a highly reactive, one-electron reducing reagent,¹⁴⁷ and for this reason it is an ideal candidate for electron transfer-driven intercalation into mesoporous niobium oxide. The steric shielding afforded by the methyl groups should provide greater thermal stability with respect to decomposition of the corresponding cation in the pores. In some cases, most notably in the reaction of bis(toluene) niobium

with mesoporous niobium oxide, the organometallic decomposes to leave a low valent metallic coat on the inner pore surface.¹⁴⁵

When a sample of trimethylsilated Nb-TMS1 with an X-ray powder diffraction (XRD) peak centered at $d(100) = 40 \text{ \AA}$, an HK pore size of 23 \AA , a BET surface area of $520 \text{ m}^2\text{g}^{-1}$, and a pore volume of $0.287 \text{ cm}^3\text{g}^{-1}$ was treated with excess decamethylsamarocene in dry THF over several days under nitrogen, a new black material was formed. Figure 43 shows the XRD peaks of the materials before and after treatment with decamethylsamarocene. The broad reflection centered at $d(100) = 35 \text{ \AA}$ in the product material demonstrates that this material fully retained its wormhole mesostructure on reaction with the organometallic.

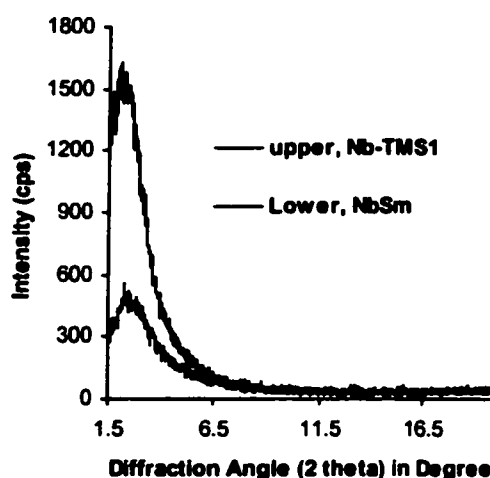


Figure 43. XRD patterns of trimethylsilated mesoporous niobium oxide before (upper) and after (lower) treatment with excess $(\text{C}_5\text{Me}_5)_2\text{Sm}(\text{THF})_2$.

The nitrogen adsorption and desorption isotherms of the material before and after treatment with decamethylsamarocene are shown in Figure 44a. The BET surface area of the treated sample dropped to $283 \text{ m}^2\text{g}^{-1}$, while the HK pore size and pore volume decreased to 20.8 \AA and $0.151 \text{ cm}^3\text{g}^{-1}$, respectively. The plots of incremental pore

volume versus average pore diameter as calculated from the adsorption strings of the isotherms are shown in Figure 44b, demonstrating that the pore size in the decamethylsamarocene composite is smaller than in the parent material. These data are consistent with partial filling of the mesopores by the encapsulated organometallic.

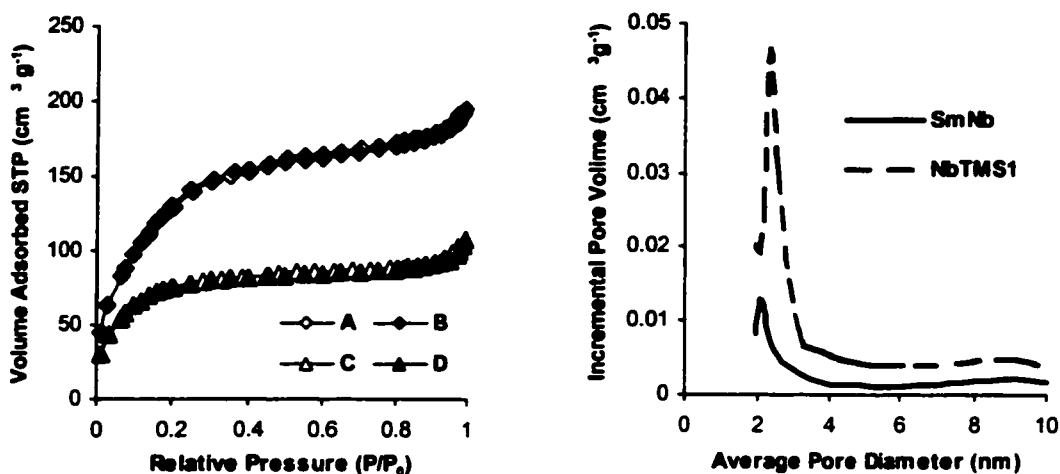


Figure 44. (a, left) Nitrogen adsorption (B, D) and desorption (A, C) isotherms of trimethylsilated mesoporous niobium oxide before (A, B) and after (C, D) treatment with excess $(C_5Me_5)_2Sm(THF)_2$. (b, right) Plots of incremental HK pore volume vs. average pore diameter before (upper) and after (lower) treatment with excess $(C_5Me_5)_2Sm(THF)_2$.

The elemental analysis of this new material showed an increase from 5.73% C and 1.43% H in the starting material to 11.78% C and 1.90% H in the product with 9.65% Sm as determined by inductively coupled plasma. The loading level of Sm in the pores (Sm:Nb = 0.14:1) is greater than in the analogous bis(benzene)chromium composites (0.07:1), but less than that in the cobaltocene composites (0.5:1). The percentage of C is consistent with the intercalation of organometallic into the pores with some loss of ligand, since the expected value on the basis of the Sm content is over 20%. Loss of ligand in

organolanthanide complexes is often more facile than in the analogous organotransition metal species because the larger coordination sphere around the metal center and lack of pi bonding to the ligand enables low-energy dissociation processes to occur.

6.2.2. EPR Spectrum

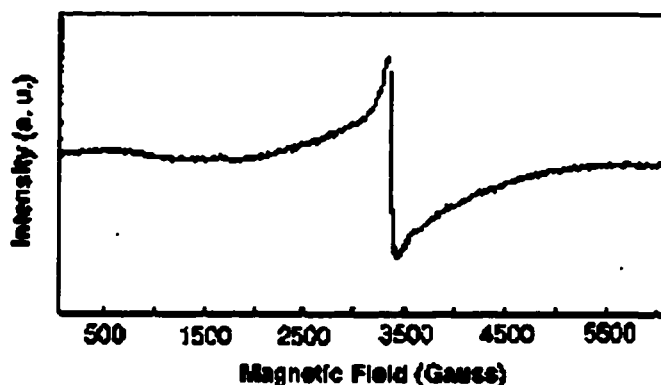


Figure 45. Powder EPR spectrum of trimethylsilated mesoporous niobium oxide after treatment with excess $(C_5Me_5)_2Sm(THF)_2$.

The powder electron paramagnetic resonance (EPR) spectrum is shown in Figure 45. This spectrum shows one peak at 3340G ($g = 2.00$) which originates from the electrons in the reduced mesoporous niobium oxide walls and is observed in many reduced mesoporous Nb oxide composites. The lack of Nb hyperfine splitting indicates that the reduction electrons are not closely associated with the Nb centers or that the material has a broad array of surface sites because of the amorphous wall structure, however the g value of 2.00, almost identical to that of a free electron, favors the former explanation. The unpaired 4f electrons from the samarium species were not detected from room temperature down to liquid nitrogen temperature because of the strong shielding of samarium 5s and 5p electrons.¹⁴⁸

6.2.3. XPS Spectra

Figure 46a shows the Nb 3d region of the reduced material and mesoporous niobium oxide (Nb-TMS1). The 5/2 and 3/2 peaks move from 207.8 eV and 210.6 eV in the starting material to 207.3 eV and 209.8 eV in the reduced material with new shoulder peaks appearing at 205.8 eV and 208.7 eV. This is consistent with reduction of the niobium oxide framework to a state between Nb(V) and Nb(IV) with a small amount of more highly-reduced phase.¹⁰⁷ Figure 46b shows the Sm 3d 5/2 and 3/2 emission region

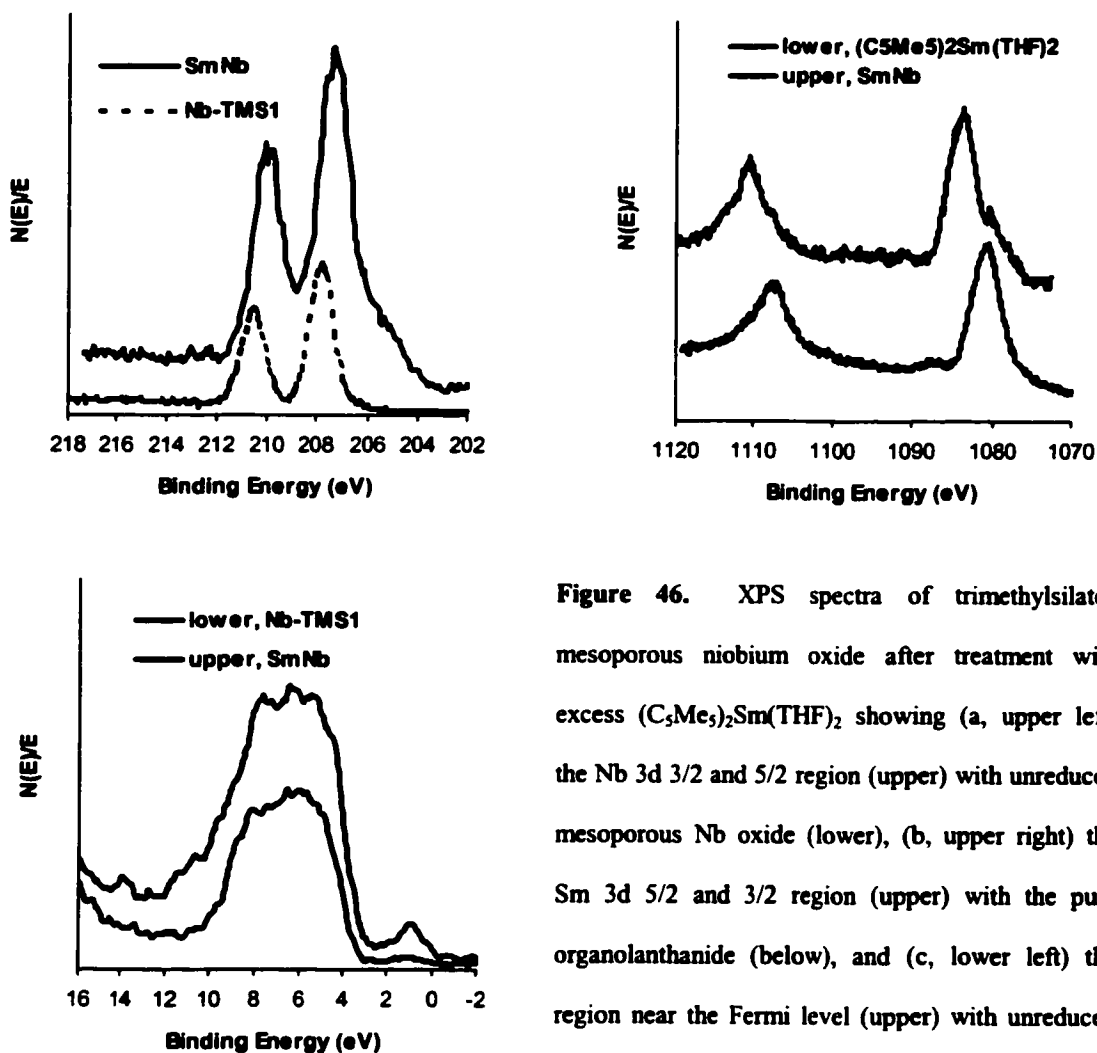


Figure 46. XPS spectra of trimethylsilated mesoporous niobium oxide after treatment with excess $(C_5Me_5)_2Sm(THF)_2$ showing (a, upper left) the Nb 3d 3/2 and 5/2 region (upper) with unreduced mesoporous Nb oxide (lower), (b, upper right) the Sm 3d 5/2 and 3/2 region (upper) with the pure organolanthanide (below), and (c, lower left) the region near the Fermi level (upper) with unreduced mesoporous Nb oxide (lower).

of $(C_5Me_5)_2Sm(THF)_2$ and its reduced mesoporous niobium oxide composite, exhibiting several emissions which can be assigned as divalent Sm (II) at 1080.2 eV and 1107.1 eV, and trivalent Sm(III) at 1083.5 eV and 1110.4 eV,¹⁴⁹ respectively. A simulation revealed a 4:1 ratio of Sm(III) to Sm(II). The emissions assigned to divalent Sm match the 3d 5/2, 3/2 emissions from pure decamethylsamarocene, which fall at 1080.3 eV and 1107.0 eV (Figure 46b lower). There is currently no spectroscopic or synthetic data available on the decamethylsamarocinium cation to verify the nature of the Sm(III) species, however the low intensity of the Sm(II) emission in the composite relative to Sm(III) emission suggests that much of the ligand was retained on oxidation, because there is not enough Sm(II) present to account for the high percentage of C in the elemental analysis. On the basis of the molecular weight of Sm(II) complex, the % Sm in the sample, and the XPS simulation, only 3.08% C in the composite could be due to the neutral Sm(II) complex. The region near Fermi level has been shown in Figure 46c, demonstrating a distance to Fermi level of 3.1 eV from the oxygen 2p valence emission, and small peak centered at 1 eV due to the samarium 4f electron emission.¹⁵⁰

6.2.4. Conductivity Measurements

Room temperature DC conductivity measurements on the samples of the decamethylsamarocene reduced mesoporous niobium composites conducted by the four-point method under argon showed that these materials are semiconducting with conductivity as high as $3 \times 10^{-6} \text{ ohm}^{-1} \text{ cm}^{-1}$. In previous work we attributed conductivity in metallocene-doped mesoporous Nb oxide composites to an electron hopping mechanism through the mixed oxidation state dopant phase in the pores with minimal involvement by the walls of the mesostructure.¹⁰⁸ Variable temperature conductivity measurements on

related bis(benzene) chromium composites show increasing resistivity with decreasing temperature. The low conductivities are expected on the basis of those values obtained for other reduced mesoporous oxides and the fact that the 4f electrons from the Sm dopant are core-like and tightly bound to the nuclei. Because of strong electron localization, few lanthanide-base materials exhibit high conductivity.

6.2.5. SQUID Measurements

Complex magnetic behavior is expected in these materials because of the many different magnetic species present, including the reduced Nb oxide walls, Sm^{2+} with four unpaired electrons, and Sm^{3+} with five unpaired electrons. Figure 47a shows the superconducting quantum interference device (SQUID) magnetometer plots of magnetic susceptibility versus temperature for the composite at 500 Gauss. The shape of this plot suggests contributions to the magnetization from a temperature dependent Langevin free spin term and a temperature independent term, most likely due to Van Vleck paramagnetism, a phenomenon observed in many other reduced mesoporous transition metal oxides studied by our group.¹⁰⁸ Pauli paramagnetism is ruled out because these materials are not metallic. The plots of magnetic susceptibility versus temperature recorded at 100 G and 10000 G showed similar curves, ruling out any field dependent magnetic transitions. Figure 47b shows the variation of the molar magnetic susceptibility (corrected by subtraction of the temperature independent term obtained by extrapolating the M vs. T plot to $T = 300\text{K}$, $\chi_g = 9.15 \times 10^{-4} \text{ emu/g}$) with inverse temperature over the temperature range from 6-200K. The linearity over this region indicates that the temperature dependent term in this material obeys Curie law (magnetic susceptibility, $\chi_m = C/T$, where $C = N\mu_B^2\mu_{\text{eff}}^2/3k$) above 20K, with a tailing off of the magnetic

susceptibility below this lower temperature. This is consistent with spin glass behavior in which electron spins become frozen and begin to cancel out the spin contributions to the

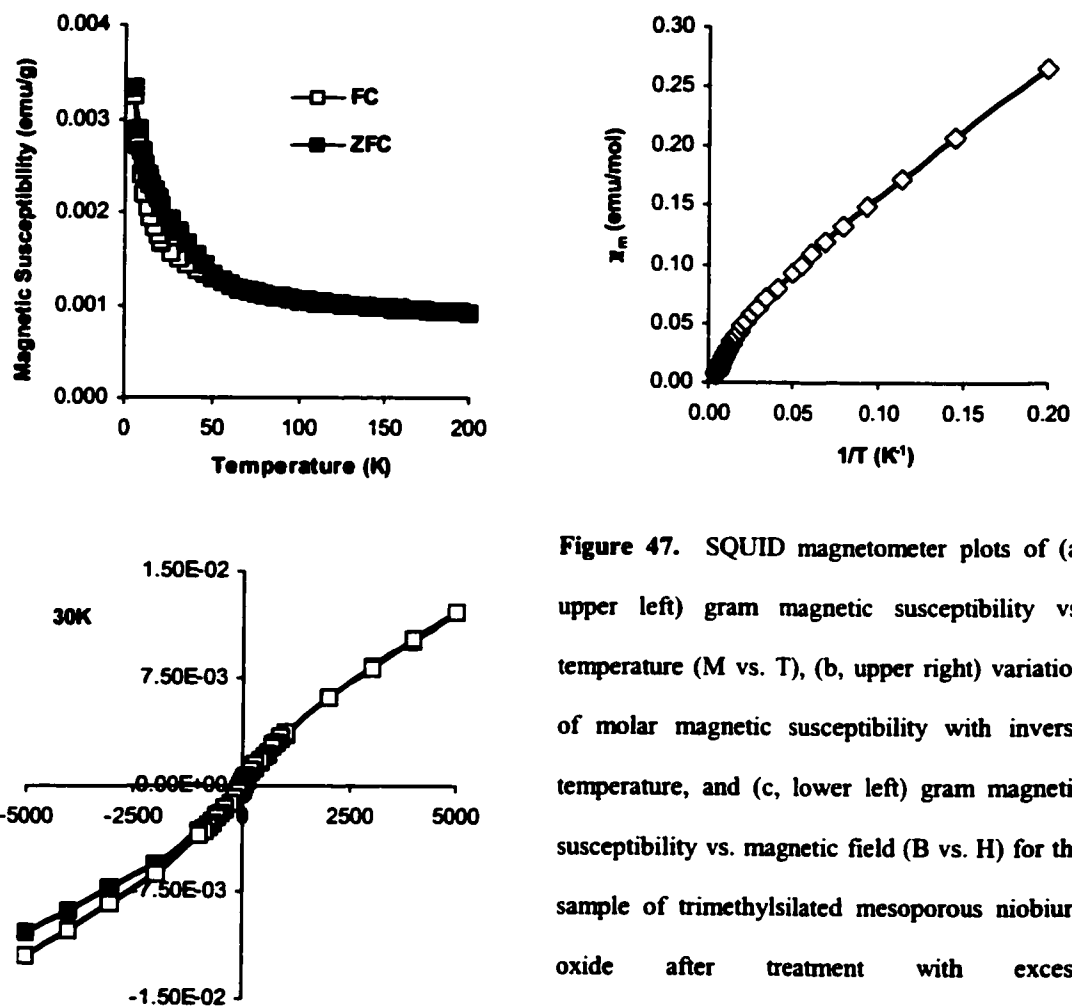


Figure 47. SQUID magnetometer plots of (a, upper left) gram magnetic susceptibility vs. temperature (M vs. T), (b, upper right) variation of molar magnetic susceptibility with inverse temperature, and (c, lower left) gram magnetic susceptibility vs. magnetic field (B vs. H) for the sample of trimethylsilated mesoporous niobium oxide after treatment with excess $(C_5Me_5)_2Sm(THF)_2$.

magnetization from other isolated spins. Spin glass behavior is common in amorphous alloys with a dilute magnetic component and has been observed in several other reduced mesoporous oxides, most notably in a mesoporous Nb oxide-nickelocene composite which undergoes a Ni-dependent superparamagnet-to-spin glass transition.⁷⁸ From the region between 100K and 200 K, a Curie constant C of 3.18 emu mol K⁻¹ can be

calculated. The effective magnetic moment μ_{eff} can also be calculated as 1.59, close to the theoretical result of 1.41 based on elemental analysis, assuming every divalent Sm (II) atom donates one electron to niobium and becomes trivalent Sm(III). Because each trivalent Sm(III) possesses five unpaired electrons, the average electrons per metal atom is 0.73 for a material with the formula $\text{Nb}_{1.0}\text{O}_{4.5}\text{Sm}_{0.14}\text{Si}_{0.21}\text{C}_{2.2}\text{H}_{4.2}$.

Figure 47c shows the plots of magnetic susceptibility versus field (B vs. H). The slight S-shape in the plot provides evidence for superparamagnetism, as a straight line is expected for a classical paramagnet. There is also a small hysteresis, indicative of some degree of domain-dependent behavior of this material. The absence of a blocking temperature (T_b) in the plot from Figure 47a suggests that this may fall below 4K, or that the superparamagnetic phase is not large enough to dominate over the paramagnetic domains. Analogous cobaltocene⁷¹ and nickelocene⁷⁸ composites show T_b values of 21K and 8K respectively. The small value of μ_{eff} is consistent with either very small superparamagnetic particles or superparamagnetism in only a small percentage of the material, because superparamagnetic particles have very large μ_{eff} and this value represents an average across the entire sample. The observation of superparamagnetism in this system is surprising because lanthanides rarely show cooperative magnetism in the pure form, although they are often added to transition metals as a dopant to improve the remanent magnetism. Because of the broad bandwidths of early transition metal compounds, which tend to favor metallic or paramagnetic states with no domain-dependent magnetic ordering, and the lack of superparamagnetism in alkali metal reduced mesoporous Nb oxides, superparamagnetism in these mesoporous Nb oxide Sm composite is not expected to arise solely from the reduced niobium oxide walls. This

suggests a cooperative mechanism in which the Sm phase in the walls is somehow influenced by the confinement in the reduced mesostructure to give magnetic coupling interactions leading to the spin alignment necessary in nanoscale domains for superparamagnetism to occur.

6.3. Conclusion

Mesoporous Nb oxide was reduced by decamethylsamarocene THF complex to give a new semiconducting composite with a mixture of decamethylsamarocene and a second Sm(III) species in the pores. Partial loss of the organic ligand was observed, suggesting that some of the Sm(II) complex did not survive oxidative intercalation. This is the first example of a reduced mesoporous transition metal complex with an organolanthanide in the pores. This is important because lanthanide elements possess many unusual magnetic and optical absorption properties due to the large number of unpaired electrons in the core of the f shell. The material was characterized by XPS, XRD, EPR, EA, and nitrogen adsorption. SQUID magnetometry studies revealed that this composite was largely paramagnetic with some evidence for spin glass behavior and superparamagnetic behavior at temperature below 40K. This is surprising given that very few Nb- or Sm-based materials display ferromagnetism and superparamagnetism which normally occurs in fine grains of ferromagnetic materials.

Chapter 7. Conclusion

The exploration of materials with two or more disparate phases interwoven into a periodic array on the nanometer scale is of much current interest due to the potential of such materials to offer properties not observed in the corresponding pure phases. Mesoporous transition metal oxides are an ideal candidate as a host in the fabrication of low-dimensional nanostructured composites because this family of materials possess not only periodical and controllable nanoscale voids which can be filled with a wide variety of molecular and continuous phase substances, but also variable oxidation states which can not be provided by mesoporous silicate counterparts. In this thesis, I have synthesized and elegantly characterized a new family of mesoporous niobium composites with mixed oxidation state of bis(benzene) chromium, bis(benzene) vanadium, bis(cyclopentadienyl) chromium, bis(cyclopentadienyl) vanadium and decamethylsamarocene, and systematically investigated their electronic and magnetic properties as well as the effects of vanadium(V) contents in the mesoporous V-Nb mixed oxides on the electronic and magnetic properties of the corresponding bis(benzene) chromium composites. The intercalation of bis-arene and Cp species into mesoporous Nb oxide by reduction reaction dramatically changed the electronic and magnetic properties of the parent mesoporous transition metal materials since the pure mesoporous Nb oxide is diamagnetic and insulating as well as bis-arene and Cp species used in this thesis are also insulating. Now the following points can be concluded.

Mesoporous niobium oxide can act as electron acceptor when it was reduced by a series of organometallics and organolanthanide, yielding semiconducting composites

with conductivity as high as $10^{-4} \text{ ohm}^{-1}\text{cm}^{-1}$. This is the first example of conducting mesoporous niobium oxide composites with mixed oxidation state organometallic species in the pores.

The oxidation of organometallics by mesoporous niobium oxide led to the formation of positive charge holes, which act as charge carriers in the electronic conduction process of the materials, in the valence band.

Since mesoporous Nb or V-Nb oxide reduced with alkali metals led to insulating materials, the mixed oxidation state of organometallic species in the pores plays a main role in the conducting nature of the mesostructure composites even though partial loss of organic ligand was observed, which made this system more complicated.

The Hubbard model involving bandwidth and Hubbard potential was the first time to be invoked to account for the mesoporous composites, which showed this model was successful in explaining the conductivity of the new family of materials.

It is possible to tune the oxidizing ability of the walls of mesoporous niobium oxide by varying the amount of vanadium (V) contents in the new mesoporous V-Nb mixed oxides. The ligand-assisted templating method was proved to be successful in this application.

The reduced mesoporous niobium oxide composites made from organometallics of transition metals in the early part of period, e.g. V, Cr, Nb, tend to afford conducting materials, and from those in the late part of period, e.g. Ni, Co tend to give insulating materials.

The reduction of mesoporous niobium oxide with decamethylsamarocene THF complex led to semiconducting, paramagnetic mesoporous composites with some degree

of superparamagnetic behavior at temperature below 40 K. This is surprising given that very few Nb and Sm based material display ferromagnetism superparamagnetism which normally occurs in fine grains of ferromagnetic materials.

Appendix:

Figure 48. Single crystal structure (ORTEP) of vanadocenium ditriflate [$\text{Cp}_2\text{V}(\text{O}_3\text{SCF}_3)_2$]

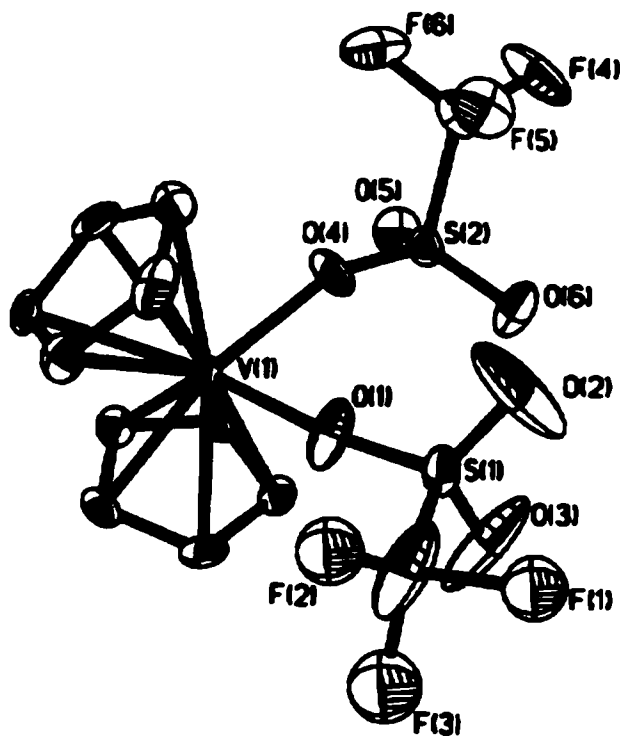


Table 9. Lattice constants and parameters of the structure determination of vanadocenium ditriflate [$\text{Cp}_2\text{V}(\text{O}_3\text{SCF}_3)_2$]

	$\text{Cp}_2\text{V}(\text{O}_3\text{SCF}_3)_2$
Formula	$\text{C}_{12}\text{H}_{10}\text{F}_6\text{O}_6\text{S}_2\text{V}$
Molecular weight	479.26
Size of the crystal (mm)	$0.50 \times 0.40 \times 0.35$
Crystal system	Monoclinic
Space group	$\text{P}2(1)/n$

Unit cell dimensions(Å or degree)	
a	8.3342(14)
b	12.681(2)
c	16.011(3)
α	90
β	91.460(3)
γ	90
Cell volume (Å ³)	1691.6(5)
Temperature of data collection (K)	293(2)
Formula units	4
Density (Mg/cm ³)	1.882
Radiation (λ , Å)	Mo K α (0.71073)
F(000)	956
Absorption coefficient (mm ⁻¹)	0.925
Theta range for data collection (degrees)	2.05 - 23.28
Limiting indices	-9 \leq h \leq 9, -14 \leq k \leq 12, -16 \leq l \leq 17
Reflections collected / unique	7138 / 2432 [R(int) = 0.0228]
Completeness to theta = 23.28	99.6 %
Data / restraints / parameters	2432 / 0 / 239
Goodness-of-fit on F ²	1.081
Final R indices [I>2sigma(I)]	R1 = 0.0705, wR2 = 0.1955
R indices (all data)	R1 = 0.0797, wR2 = 0.2031
Largest diffraction peak and hole	1.040 and -0.818 e.Å ⁻³

Table 10. Atomic coordinates ($\times 10^4$) and equivalent isotropic displacement parameters ($\text{Å}^2 \times 10^3$) for $\text{Cp}_2\text{V}(\text{O}_3\text{SCF}_3)_2$

Atom	x	y	z	U(eq)
V(1)	284(1)	5740(1)	7693(1)	31(1)
S(1)	-3090(2)	5743(2)	6473(1)	59(1)
S(2)	-2720(2)	5430(2)	9081(1)	51(1)
O(1)	-1581(7)	5870(5)	6845(4)	92(2)
O(2)	-3133(16)	4539(10)	6335(8)	78(3)
O(2')	-3977(17)	4884(11)	6597(8)	83(3)
O(3)	-4598(18)	6068(12)	6625(9)	95(4)
O(3')	-3880(20)	6756(14)	6750(9)	110(5)
O(4)	-1449(7)	5834(4)	8564(4)	78(2)
O(5)	-2151(7)	4855(5)	9785(4)	76(2)
O(6)	-4013(8)	5016(6)	8600(4)	97(2)
F(1)	-4332(16)	6215(10)	5019(8)	97(3)
F(1')	-3641(18)	5877(10)	4835(8)	97(4)
F(2)	-1943(18)	6716(13)	5179(9)	116(4)
F(2')	-2582(16)	7284(11)	5537(8)	106(4)
F(3)	-2220(20)	5026(18)	5084(12)	155(6)
F(3')	-1111(19)	5989(12)	5229(9)	119(4)
F(4)	-4595(9)	6480(6)	10027(5)	152(3)
F(5)	-3939(8)	7304(5)	8923(4)	107(2)
F(6)	-2302(9)	7149(5)	9935(4)	114(2)
C(1)	1840(10)	6958(6)	7038(5)	64(2)
C(2)	430(11)	7476(6)	7243(8)	80(3)
C(3)	1654(11)	6985(6)	8437(5)	68(2)
C(4)	320(11)	7487(5)	8079(8)	77(3)
C(5)	2620(8)	6689(6)	7780(6)	62(2)
C(6)	2156(8)	4516(5)	8141(5)	54(2)

C(7)	2179(9)	4564(5)	7264(5)	57(2)
C(8)	-249(9)	3985(5)	7626(5)	54(2)
C(9)	706(11)	4237(5)	6952(5)	62(2)
C(10)	668(9)	4148(5)	8372(5)	55(2)
C(11)	-2766(15)	6021(13)	5392(9)	131(6)
C(12)	-3436(10)	6640(7)	9507(5)	70(2)

U_{eq} is defined as one third of the trace of the orthogonalized U_{ij} tensor.

Table 11. Selected bond distance (Å) and bond angles (°) for $Cp_2V(O_3SCF_3)_2$

V(1)-O(4)	2.037(5)
V(1)-O(1)	2.044(5)
S(1)-O(1)	1.387(5)
S(2)-O(4)	1.454(5)
S(2)-O(6)	1.409(6)
S(1)-O(2)	1.335(13)
O(4)-V(1)-O(1)	84.8(3)
S(2)-O(4)-V(1)	155.3(4)
S(1)-O(1)-V(1)	160.3(4)
O(1)-S(1)-C(11)	103.5(5)
O(4)-S(2)-C(12)	99.8(4)
O(6)-S(2)-O(4)	112.2(4)
O(2)-S(1)-O(1)	122.1(6)
C(4)-V(1)-C(2)	33.8(4)
C(1)-V(1)-C(7)	84.2(3)
O(4)-V(1)-C(10)	79.7(3)

References

- (1) Schmidt, O. G.; Schmarje, N.; Deneke, C.; Müller, C.; Jin-Phillipp, N.-Y. *Adv. Mater.* **2001**, *13*, 756.
- (2) Whitcombe, M. J.; Vulfson, E. N. *Adv. Mater.* **2001**, *13*, 467.
- (3) Lee, K. Y.; Peters, M. C.; Mooney, D. J. *Adv. Mater.* **2001**, *13*, 837.
- (4) Nguyen, T.Q.; Wu, J.; Tolbert, S. H.; Schwartz, B. J. *Adv. Mater.* **2001**, *13*, 609.
- (5) (a) Kresge, C. T.; Leonowicz, M. E.; Roth W. J.; Vartulli, J. C.; Beck, J. S. *Nature* **1992**, *359*, 710; (b) Beck, J. S.; Vartuli, J. C.; Roth, W. J.; Leonowicz, M. E.; Kresge, C. T.; Schmitt, K. D.; Chu, C. T-W.; Olson, D. H.; Shepard, E. W.; McCullen S. B.; Higgins, J. B.; Schlenker, J. L. *J. Am. Chem. Soc.* **1992**, *114*, 10834.
- (6) (a) Huo, Q.; Margolese, D. I.; Ciesla, U.; Demuth, D. G.; Feng, P.; Gier, T. E.; Sieger, P.; Firouzi, A.; Chmelka, B. F.; Schuth, F.; Stucky, G. D. *Chem. Mater.* **1994**, *6*, 1176; (b) Firouzi, A.; Kumar, D.; Bull, L. M.; Besier, T.; Sieger, P.; Huo, Q.; Walker, S. A.; Zasadzinski, J. A.; Glinka, C.; Nicol, J.; Margolese, D.; Stucky, G. D.; Chmelka, B. F. *Science* **1995**, *267*, 1138; (c) Ciesla, U.; Demuth, D.; Leon, R.; Petroff, P.; Stucky, G.; Unger, K.; Schuth, F. *J. Chem. Soc., Chem. Commun.* **1994**, 1387.
- (7) Tanev, P. T.; Chibwe, M.; Pinnavaia, T. J. *Nature* **1994**, *368*, 321.
- (8) Chen, C.-Y.; Burkette, S. L.; Li, H.-X.; Davis, M. E. *Micropor. Mater.* **1993**, *2*, 27.
- (9) Antonelli, D. M.; Ying, J. Y., *Curr. Opin. Coll. Interface Sci.* **1996**, *1*, 523.
- (10) Behrens, P. *Angew. Chem. Int. Ed. Engl.* **1996**, *35*, 515.

- (11) Yang, H.; Coombs, N.; Ozin, G. A. *Nature* **1997**, *386*, 692.
- (12) Walsh, D.; Mann, S. *Nature* **1995**, *377*, 320.
- (13) Chomsky, E.; Ozin, G. *Adv. Mater.* **2000**, *12*, 1071.
- (14) Davis, M. E. *Nature* **1993**, *364*, 391.
- (15) Ying, J. Y.; Mehnert, C. P.; Wong, M. S. *Angew. Chem. Int. Ed. Engl.* **1999**, *38*, 56.
- (16) Antonietti, M.; Berton, B.; Goeltner, C.; Hentze, H. *Adv. Mater.* **1998**, *10*, 154.
- (17) Zhao, D.; Feng, J.; Huo, Q.; Melosh, N.; Frederickson, G. H.; Chmelka, B. F.; Stucky, G. D. *Science* **1998**, *279*, 548.
- (18) Tanev, P. T.; Pinnavaia, T. J. *Science* **1996**, *271*, 1267.
- (19) Imhof, A.; D. Pine, J. *Nature* **1997**, *389*, 948.
- (20) Holland, B. T.; Blanford, C. F.; Stein, A. *Science* **1998**, *281*, 538.
- (21) Wijnhoven, J. E. G. J.; Vos, W. L. *Science* **1998**, *281*, 802.
- (22) Norris, D. J.; Vlasov, Y. A. *Adv. Mater.* **2001**, *13*, 371.
- (23) Huo, Q.; D. Margolese, I.; Ciesla, U.; Feng, P.; Gier, T. E.; Sieger, P.; Leon, R.; Petroff, P. M.; Schüth, F.; Stucky, G. *Nature* **1994**, *368*, 317.
- (24) Antonelli, D. M.; Ying, J. Y. *Angew. Chem. Int. Ed. Engl.* **1996**, *35*, 426.
- (25) Antonelli, D. M.; Nakahira, Y. A.; Ying, J. *Inorg. Chem.* **1996**, *35*, 3126.
- (26) Sun, T.; Ying, J. Y. *Nature* **1997**, *389*, 704.
- (27) Antonelli, D. M. *Microporous and Mesoporous Materials* **1999**, *33*, 209.
- (28) Antonelli, D. M.; Ying, J. Y. *Chem. Mater.* **1996**, *8*, 874.
- (29) Ciesla, U.; Schacht, S.; Stucky, G. D.; Unger, K.; Schuth, F. *Angew. Chem., Int. Ed. Engl.* **1996**, *35*, 541.
- (30) Reddy, J. S.; Sayari, A. *Catal. Lett.* **1996**, *38*, 219.

- (31) Wong, M. S.; Antonelli, D. M.; Ying, J. Y. *Nanostruct. Mater.* **1997**, *9*, 165.
- (32) Antonelli, D. M.; Ying, J. Y. *Angew. Chem. Intl. Ed. Engl.* **1995**, *34*, 2014.
- (33) Liu, P.; Liu, J.; Sayari, A. *Chem. Commun.* **1997**, 577.
- (34) Antonelli, D. M. *Adv. Mater.* **1999**, *11*, 488.
- (35) Antonelli, D. M., *Microporous and Mesoporous Materials* **1999**, *30*, 315.
- (36) Wang, Y.; Tang, X.; Lin, L.; Huang, W.; Hacoheh, Y. R.; Gedanken, A. *Adv. Mater.* **2000**, *12*, 1183.
- (37) Takahara, Y.; Kondo, J. N.; Takata, T.; Lu, D.; Domen, K. *Chem. Mater.* **2001**, *13*, 1200.
- (38) Tian, Z. R.; Wang, J. Y.; Duan, N. G.; Krishnan, V. V.; Suib, S. L. *Science* **1997**, *276*, 926.
- (39) Mamak, M.; Coombs, N.; Ozin, G. *Adv. Mater.* **2000**, *12*, 198.
- (40) Wachhold M.; Rangan, K. K.; Billinge, S. J. L.; Petkov, V.; Heising, J.; Kanatzidis, M. G. *Adv. Mater.* **2000**, *12*, 85.
- (41) MacLachlan, M. J.; Coombs, N.; Ozin, G., *Nature* **1999**, *397*, 681.
- (42) Vettraiho, M.; Trudeau, M.; Antonelli, D. M. *Adv. Mater.* **2000**, *12*, 337.
- (43) Vettraiho, M.; Trudeau, M.; Antonelli, D. M. *Inorg. Chem.* **2001**, *40*, 2088.
- (44) Minh, N. Q.; *J. Am. Ceram. Soc.* **1993**, *76*,563; Steele, B. C. H. *Nature* **1999**, *400*,619.
- (45) Verweij, H. *Adv. Mater.* **1998**, *10*, 1483. Ziehfrend, A.; Simon, U.; Maier, W. F. *Adv. Mater.* **1996**, *8*, 424. Berkel, van F. P. F.; Heuveln, van F. H.; Huijsmans, J. P. P. *Solid State Ionics* **1994**, *72*, 240. Steele, B. C. H. *Solid State Ionics* **1997**, *94*, 239. Shiga, H.; Okubo, T.; Sadakata, M. *Ind. Eng. Chem. Res.* **1996**, *35*, 4479.

- (46) Mamak, M.; Coombs, N.; Ozin, G., *J. Am. Chem. Soc.* **2000**, 122, 8932.
- (47) Mamak, M.; Coombs, N.; Ozin, G. *Adv. Funct. Mater.* **2001**, 11, 59.
- (48) Neeraj; Rao, C. N. R. *J. Mater. Chem.* **1998**, 8, 1631.
- (49) Zheng, H.; Colby, M. W.; Mackenzie, J. D. *Mater. Res. Soc. Symp. Proc.* **1988**, 121, 537. Holland, B. T.; Blanford, C. F.; Do, T.; Stein, A. *Chem. Mater.* **1999**, 11, 795.
- (50) Zhao, D.; Goldfarb, D. *Chem. Mater.* **1996**, 8, 2571.
- (51) Abe, T.; Taguchi, A.; Iwamoto, M. *Chem. Mater.* **1995**, 7, 1429.
- (52) Antonelli, D. M.; Trudeau, M. *Angew. Chem., Int. Ed. Engl.* **1999**, 38, 1471.
- (53) Ozin, G. A. *Acc. Chem. Res.* **1997**, 30, 17.
- (54) Oliver, S.; Kuperman, A.; Coombs, N.; Lough, A.; Ozin, G. A. *Nature* **1995**, 378, 47.
- (55) Terrones, M.; Terrones, H.; Banhart, F.; Charlier, J.-C.; Ajayan, P. M. *Science* **2000**, 288, 1226.
- (56) Davis, R. J.; Gainer, J.; O'Neal, G.; Wu, I-W. *Water Environ. Res.* **1994**, 66, 50.
- (57) Al-sayyed, G.; D'Oliveira, J. C.; Pichat, P. *J. Photochem. Photobiol. A* **1991**, 58, 99.
- (58) Saladin, F.; Forss, L.; Kamber, I. *J. Chem. Soc. Chem Commun.* **1995**, 533.
- (59) Anpo, M.; Yamashita, H.; Ichihashi, Y.; Ehara, S. *J. Electroanal. Chem.* **1995**, 396, 21. Yamashita, H.; Kamada, N.; He, H.; Tanaka, K.; Ehara, S.; Anpo, M. *Chem. Lett.* **1994**, 855.
- (60) Yamagata, S.; Nishijo, M.; Murao, N.; Ohta, S.; Mizoguchi, I. *Zeolites* **1995**, 15, 490.

- (61) Bard, A. J.; Fox, M. A. *Acc. Chem. Res.* **1995**, *28*, 141.
- (62) Sayama, K.; Tanaka, A.; Domen, K.; Maruya, K.; Onishi, T. *J. Catal.* **1990**, *124*, 541.
- (63) Tanaka, K.; Harada, K.; Murata, S. *Sol. Energy* **1986**, *36*, 159.
- (64) Stone, V. F.; Davis, Jr. R. J. *Chem. Mater.* **1998**, *10*, 1468.
- (65) Takahara, Y.; Kondo, J. N.; Takata, T.; Lu, D.; Domen, K. *Chem. Mater.* **2001**, *13*, 1194.
- (66) Kudo, A.; Kato, H.; Nakagawa, S. *J. Phys. Chem. B* **2000**, *104*, 571.
- (67) Ishihara, T.; Nishiguchi, H.; Fukumachi, K.; Takita, Y. *J. Phys. Chem. B* **1999**, *103*, 1.
- (68) Sayama, K.; Arakawa, H.; *J. Photochem. Photobiol. A* **1994**, *77*, 243.
- (69) Cox, P. A. *The Electronic Structure and Chemistry of Solids*, Oxford University Press, New York, **1987**.
- (70) Brock, S. L.; Duan, N.; Tian, Z. R.; Giraldo, O.; Zhou, H.; Suib, S. L. *Chem. Mater.* **1998**, *10*, 2619.
- (71) Murray, S.; Trudeau, M.; Antonelli, D. M. *Adv. Mater.* **2000**, *12*, 1339.
- (72) Murray, S.; Trudeau, M.; Antonelli, D. M. *Inorg. Chem.* **2000**, *39*, 5901.
- (73) O'Hare, D. *Chem. Soc. Rev.* **1992**, 121.
- (74) Blythe, H. J.; Fedosyuk, V. M.; *J. Phys., Condens. Matter.* **1995**, *7*, 3461.
- (75) Wirnsberger, G.; Gatterer, K.; Fritzer, H. P.; Grogger, W.; Pillep, B.; Behrens, P.; Hansen, M. F.; Koch, C. B. *Chem. Mater.* **2001**, *13*, 1453.
- (76) Wirnsberger, G.; Gatterer, K.; Fritzer, H. P.; Grogger, W.; Pillep, B.; Behrens, P.; Hansen, M. F.; Koch, C. B. *Chem. Mater.* **2001**, *13*, 1467.

- (77) Padovani, S.; Chado, I.; Scheurer, F.; Bucher, J. P. *Phys. Rev. B* **1999**, *59*, 11887.
- (78) Vettraiño, M.; He, X.; Trudeau, M.; Antonelli, D. M. *J. Mater. Chem.* **2001**, *11*, 1755.
- (79) Shen, T. D.; Schwarz, R. B.; Thompson, J. D. *J. Appl. Phys.* **1999**, *85*, 4110.
- (80) Ye, B.; Trudeau, M.; Antonelli, D. M. *Adv. Mater.* **2001**, *13*, 29.
- (81) Ye, B.; Trudeau, M.; Antonelli, D. M. *Adv. Mater.* **2001**, *13*, 561.
- (82) (a) Lof, R. W.; Veenendaal, van M. A.; Koopmans, B.; Jonkman, H. T.; Sawatzky, G. A. *Phys. Rev. Lett.* **1992**, *68*, 3924. (b) Rosseinsky, M. J. *Chem. Mater.* **1998**, *10*, 2665.
- (83) Ye, B.; Trudeau, M.; Antonelli, D. M. *Chem. Mater.* **2001**, *13*, 2730.
- (84) Cheng, W.; Baudrin, E.; Dunn, B.; Zink, J. I. *J. Mater. Chem.* **2001**, *11*, 92.
- (85) Yang, P.; Zhao, D.; Margolese, D. I.; Chmelka, B. F.; Stucky, G. D. *Chem. Mater.* **1999**, *11*, 2813.
- (86) Yang, P.; Zhao, D.; Margolese, D. I.; Chmelka, B. F.; Stucky, G. D. *Nature* **1998**, *396*, 152.
- (87) MacLachlan, M. J.; Coombs, N.; Bedard, R. L.; White, S.; Thompson, L. K.; Ozin, G. A. *J. Am. Chem. Soc.* **1999**, *121*, 12005.
- (88) Osenar, P.; Braun, P. V.; Stupp, S. I. *Adv. Mater.* **1996**, *8*, 1022.
- (89) Braun, P. V.; Osenar, P.; Stupp, S. I. *Nature* **1996**, *380*, 325.
- (90) Stupp, S. I.; Braun, P. V. *Science* **1997**, *277*, 1242.
- (91) Li, J.; Kessler, H.; Souldard, M.; Khouchaf, L.; Tuiler, M. H. *Adv. Mater.* **1998**, *10*, 946.

- (92) Jiang, T.; Ozin, G. A. *J. Mater. Chem.* **1998**, *8*, 1099. Jiang, T.; Ozin, G. A.; Bedard, R. L. *J. Mater. Chem.* **1998**, *8*, 1641.
- (93) Fröba, M.; Oberender, N. *Chem. Commun.* **1997**, 1729.
- (94) Neeraj, C. N. R. Rao, *J. Mater. Chem.* **1998**, *8*, 279.
- (95) Wachhold, M.; Rangan, K. K.; Lei, M.; Thorpe, M. F.; Billinge, S. J. L.; Petkov, V.; Heising, J.; Kanatzidis, M. G. *J. Solid State Chem.* **2000**, *152*, 21.
- (96) Prouzet, E.; Pinnavaia, T. J. *Angew. Chem. Int. ed. Engl.* **1997**, *36*, 516. Bagshaw, S. A.; Pinnavaia, T. J. *Angew. Chem. Int. ed. Engl.* **1996**, *35*, 1102.
- (97) Rangan, K. K.; Billinge, S. J. L.; Petkov, V.; Heising, J.; Kanatzidis, M. G. *Chem. Mater.* **1999**, *11*, 2629.
- (98) Rangan, K. K.; Trikalitis, P. N.; Kanatzidis, M. G. *J. Am. Chem. Soc.* **2000**, *122*, 10230.
- (99) Trikalitis, P. N.; Bakas, T.; Papefthymiou, V.; Kanatzidis, M. G. *Angew. Chem. Int. Ed. Engl.* **2000**, *39*, 4558.
- (100) Beinert, H.; Holm, R. H.; Münck, E. *Science* **1997**, *277*, 653.
- (101) Trikalitis, P. N.; Rangan, K. K.; Bakas, T.; Kanatzidis, M. G. *Nature* **2001**, *410*, 671.
- (102) Attard, G. S.; Göltner, C. G.; Corker, J. M.; Henke, S.; Templer, R. H. *Angew. Chem. Int. Ed. Engl.* **1997**, *36*, 1315.
- (103) Attard, G. S.; Bartlett, P. N.; Coleman, N. R. B.; Elliott, J. M.; Owen, J. R.; Wang, J. H. *Science* **1997**, *278*, 838.
- (104) Attard, G. S.; Leclerc, S. A. A.; Maniguet, S.; Russell, A. E.; Nandhakumar, I.; Bartlett, P. N. *Chem. Mater.* **2001**, *13*, 1444.

- (105) Bell, T.; Antonelli, D. *Adv. Mater.* **1998**, *10*, 846.
- (106) He, X.; Trudeau, M.; Antonelli, D. M. *Adv. Mater.* **2000**, *12*, 1036.
- (107) He, X.; Trudeau, M.; Antonelli, D. M. *Inorg. Chem.* **2001**, *40*, 6463.
- (108) He, X.; Trudeau, M.; Antonelli, D. M. *Chem. Mater.* **2001**, *13*, 4808.
- (109) MacFarlane, D. R.; Huang, J.; Forsyth, M. *Nature* **1999**, *402*, 792.
- (110) Prins, R.; Reinders, F. J. *Chem. Phys. Lett.* **1969**, *3*, 45.
- (111) Wu, C.-G.; Bein, T. *Chem. Mater.* **1994**, *6*, 1109.
- (112) Binder, H.; Elschenbroich, Ch. *Angew. Chem. Inter. Ed. Engl.* **1973**, *12*, 659.
- (113) Beck, J.J., *Magnetic Properties of Metals and Alloys*, American Society for Metals, Cleveland, Ohio, **1959**.
- (114) Fischer, E. O.; Reckziegel, A. *Chem. Ber.* **1961**, *94*, 2204.
- (115) Andrews, M. P.; Mattar, S. M.; Ozin, G. A. *J. Phys. Chem.* **1986**, *90*, 1037.
- (116) Biener, J.; Bäumer, M.; Wang, J.; Madix, R. *Surf. Sci.* **2000**, *450*, 12.
- (117) Calderazzo, F.; Benedetto, G. E. D.; Pampaloni, G.; Mössmer, C. M.; Strähle, J.; Wurst, K. *J. Organomet. Chem.* **1993**, *451*, 78.
- (118) He, X.; Antonelli, D. M. unpublished results.
- (119) Anderson, S. E.; Drago, R. S. *Inorg. Chem.* **1972**, *11*, 1546.
- (120) Clemente, D. A.; Marzotto, A. *J. Mater. Chem.* **1996**, *6*, 941.
- (121) Evans, S.; Green, J. C.; Jackson, S. E.; Hingginson, B. *J. Chem. Soc. Dalton Trans.* **1974**, *2*, 304.
- (122) Evans, S.; Green, J. C.; Jackson, S. E.; *J. Chem. Soc. Faraday Trans. II* **1974**, *70*, 236.
- (123) Pandey, R.; Rao, B. K.; Jena, P.; Blanco, M. A. *J. Am. Chem. Soc.* **2001**, *123*, 3799.

- (124) Giordan, J. C.; Moor, J. H.; Tossell, J. A.; Weber, J. *J. Am. Chem. Soc.* **1983**, *105*, 3431.
- (125) Burrow, P. D.; Modelli, A.; Guerra, M.; Jordan, K. D. *Chem. Phys. Lett.* **1985**, *118*, 328.
- (126) Cloke, F. G. N. *Chem. Soc. Rev.* **1993**, *17*.
- (127) Anderson, S. E. Jr.; Drago, R. S. *J. Am. Chem. Soc.* **1970**, *92*, 4244.
- (128) Almeida, M.; Gaudiello, J. G.; Kellogg, G. E.; Tetrick, S. M.; Marcy, H. O.; McCarthy, W. J.; Butler, J. C.; Kannewurf, C. R.; Marks, T. J. *J. Am. Chem. Soc.* **1989**, *111*, 5271.
- (129) Gordon, K. R.; Warren, K. D. *Inorg. Chem.* **1978**, *17*, 987.
- (130) Green, J. C.; Payne, M. P.; Teuben, J. H. *Organometallics* **1983**, *2*, 203.
- (131) McConnell, H. M.; Porterfield, W. W.; Robertson, R. E. *J. Chem. Phys.* **1959**, *30*, 442; Prins, R.; Biloen, P.; Voorst, J. D. W. van *J. Chem. Phys.* **1967**, *46*, 1216.
- (132) Armstrong, D. R.; Fortune, R.; Perkins, P. G. *J. Organomet. Chem.* **1976**, *111*, 197.
- (133) Perkin-Elmer Corporation, Physical Electronics Division. *Handbook of X-Ray Photoelectron Spectroscopy*.
- (134)(a) Ghosh, P.; Kotchevar, A. T. *Inorg. Chem.* **1999**, *38*, 3730. (b) Ozin, G. A.; Godber, J. *J. Phys. Chem.* **1989**, *93*, 878.
- (135) Barrera, J. A.; Wilcox, D. E. *Inorg. Chem.* **1992**, *31*, 1745.
- (136) Desai, V. P.; Konig, E. *J. Chem. Phys.* **1983**, *78*, 6299.
- (137) Evans, S.; Green, M. L. H.; Jewitt, B.; King, G. H.; Orchard, A. F. *J. Chem. Soc. Faraday Trans. II* **1974**, *70*, 356.
- (138) Gutsev, G. L.; Rao, B. K.; Jena, P. *J. Phys. Chem. A* **2000**, *104*, 5374.

- (139)Gutsev, G. L.; Rao, B. K.; Jena, P. *J. Phys. Chem. A* **2000**, 104, 11961.
- (140)Harrison, W. A. *Electronic Structure and the Properties of Solid*, Dover Publications, New York, **1989**.
- (141)Fischer, E. O. *Inorganic Syntheses*, **1960**, 6, 132.
- (142)Fischer, E. O. *Inorganic Syntheses*, **1960**, 6, 136.
- (143)Bogomolova, L. D.; Stefanovsky, S. V.; Troole, A. Y.; Vance, E. R. *J. Mater. Sci.* **2001**, 36, 1213.
- (144)Mendialdua, J.; Casanova, R.; Barbaux, Y. *J. Electron Spectrosc. Relat. Phenom.* **1995**, 71, 249.
- (145)Vettraiño, M.; He, X.; Drake, J. E.; Trudeau, M.; Antonelli, D. M. *Adv. Funct. Mater.* **2002**, 12, 174.
- (146)Chen, C-W, *Magnetism and Metallurgy of Soft Magnetic Materials*, Dover Publications, New York, **1986**.
- (147)Evans, W. J.; Grate, J. W.; Choi, H. W.; Bloom, I.; Hunter, W. E.; Atwood, J. L. *J. Am. Chem. Soc.* **1985**, 107, 941.
- (148)Wertz, J. E.; Bolton, J. R. *Electron Spin Resonance Elementary Theory and Practical Application*, McGraw-Hill Inc., United States, **1972**.
- (149)Suzuki, K; Enoki, T.; Bandow, S. *Phy. Rev. B* **1993**, 48, 11077.
- (150)Franciosi, A.; Perfetti, P.; Katnani, A. D.; Weaver, J. H.; Margaritonda, G. *Phy. Rev. B* **1984**, 29, 5611.

Vita Auctoris

Name: Xun He

Place of Birth: Sichuan, China

Education: Southwest China Normal University, China
1989-1993 Honor B. Sc.
Institute of Chemistry, Chinese Academy of Sciences, China
1993-1996 M. Sc.
University of Windsor, Canada
1999-2002 M. Sc.

Publications and Presentations

(1999 - 2002)

Publications:

- (1) **Xun He**, Michel Trudeau, David Antonelli, Electronic Properties of Novel Mixed Oxidation-State Bis-Arene Chromium Nanowires Supported by a Mesoporous Niobium Oxide Host, *Advanced Materials*, **2000**, 12, 1036.
- (2) **Xun He**, Michel Trudeau, David Antonelli, Synthesis and Electronic Properties of Low-Dimensional Bis(benzene)vanadium Reduced Mesoporous Niobium Oxide Composites, *Inorganic Chemistry*, **2001**, 40, 6463.

- (3) **Xun He, Michel Trudeau, David Antonelli, Bis(cyclopentadienyl)chromium and Bis(cyclopentadienyl)vanadium Composites of Mesoporous Niobium Oxide with Pseudo- One-Dimensional Organometallic Wires in the Pores, *Chemistry of Materials*, 2001, 13, 4808.**
- (4) **Melissa Vettrano, Xun He, Michel Trudeau, David Antonelli, Superparamagnetic and Spin Glass Behaviors in Mesoporous Niobium Oxide Bis(cyclopentadienyl) Nickel Composites, *Journal of Materials Chemistry*, 2001, 11, 1755.**
- (5) **Melissa Vettrano, Bing Ye, Xun He, David Antonelli, Self-Assembled Molecular Nanowires in Mesoporous Transition Metal Oxide Hosts: Conducting Peas in an Insulating Pod, *Australian Journal of Chemistry*, 2001, 54, 85.**
- (6) **Xun He, David Antonelli, Recent Advances in Synthesis and Applications of Transition Metal Containing mesoporous Molecular Sieves, *Angewandte Chemie International Edition*, 2002, 41, 214.**
- (7) **Melissa Vettrano, Xun He, Michel Trudeau, David Antonelli, Synthesis of the First Stable Metallic Molecular Sieve by Single Atom Transfer Modification of a Mesoporous Niobium Oxide Host Structure, *Advanced Functional Materials*, 2002, 12, 174.**
- (8) **Xun He, Michel Trudeau, David Antonelli, Electronic and Magnetic Properties of Bis-benzene Chromium Composites of Mesoporous V-Nb Mixed Oxides, submitted.**
- (9) **Xun He, Michel Trudeau, David Antonelli, Magnetic Properties of Decamethylsamarocene Composites of Mesoporous Niobium Oxide, submitted.**

Presentations:

- (1) **Xun He, David Antonelli and Michel Trudeau, Reduced Organometallic Composites of Mesoporous Niobium Oxide with one-Dimensional Organometallic Phase in the Pores. *84th CSC Conference and Exhibition*, May 26th-30th, 2001. Montreal, Canada.**
- (2) **Xun He, David Antonelli and Michel Trudeau, Synthesis and Electronic Properties of Novel Mixed Oxidation-state Bis-Arene Chromium Nanowires Supported by a Mesoporous Niobium Oxide Host, *2th International Symposium on Mesoporous Molecular Sieves*. Aug. 27th-Sept. 2nd, 2000, Quebec City, Canada.**